

Polymer-Ligated Nanocrystals with Tunable Dimensions, Compositions, and Architectures

A Dissertation

Presented to

The Academic Faculty

by

Mingyue Zhang

In Partial Fulfilment

Of the Requirements for the Degree

DOCTOR OF PHILOSOPHY in the

SCHOOL OF MATERIALS SCIENCE AND ENGINEERING

Georgia Institute of Technology

December 2022

COPYRIGHT©2022 BY MINGYUE ZHANG

Polymer-Ligated Nanocrystals with Tunable Dimensions, Compositions, and Architectures

Approved by:

Dr. Zhiqun Lin, Advisor

School of Materials Science and Engineering
Georgia Institute of Technology

Dr. Vladimir Tsukruk, Co-advisor

School of Materials Science and Engineering
Georgia Institute of Technology

Dr. Seung Soon Jang

School of Materials Science and Engineering
Georgia Institute of Technology

Dr. Zhitao Kang

Georgia Tech Research Institute
School of Materials Science and Engineering
Georgia Institute of Technology

Dr. Xing Xie

School of Civil and Environmental
Engineering
Georgia Institute of Technology

Date Approved: [September 23, 2022]

ACKNOWLEDGEMENTS

First of all, I want to give my greatest appreciation to my advisor Professor Zhiqun Lin, for his support, guidance, inspiration, encouragement, and patience in the past four years. The nanoreactor projects are really challenging, without Dr. Lin's constant help, I cannot pass through the difficult times. Dr. Lin is not only an advisor to me, but also a role model. His passion about research and science, his hard-working attitude toward the career, and his healthy lifestyle despite of the heavy work, inspire and motivate me to continuously improve myself in many aspects. Moreover, I would like to sincerely thank Dr. Lin for his trust and invitation to work as postdoctoral research fellow in his new lab at National University of Singapore. Thanks to this exciting opportunity, I can graduate from Ph.D. in 4 years, continue my research projects, and move one step closer to my career goal. I would also like to thank all my committee members, Dr. Seung Soon Jang, Dr. Zhitao Kang, Dr. Vladimir Tsukruk, and Dr. Xing Xie for their constructive advice and guidance throughout my Ph.D. study. Specifically, I am very grateful to Professor Vladimir Tsukruk, for serving as my co-advisor in my last semester at GaTech. I also want to thank Dr. Yulin Deng, who provided many valuable suggestions to me when I started my Ph.D.

I would not be able to accomplish anything without the help and support from the former and current group members of our NanoFM group. First, I am deeply grateful to Dr. Zewei Wang, Dr. Yihuang Chen and Dr. Shuang Liang for their hand-by-hand mentoring and training and their nonstop insightful and helpful suggestions during my Ph.D. study. Second, I would like to appreciate the support and help in my research that I received from our current and former members, especially our Nanoreactor subgroup, Dr. Xinchang Pang, Dr. Zili Li, Dr. Yanjie He,

Dr. Yijiang Liu, Dr. Yeu Wei Harn, Dr. Young Jun Yoon, Dr. Shuang Pan, Dr. Dingfeng Sheng, Dr. Qianqian Fan, Dr. Jiwoo Yu, Dr. Han Miao, Dr. Baoying Dai, Chao Yang, Woosung Choi, Jinyoung Choi, Shiqi Wei, and Minju Kim, we all “suffered”, enjoyed, improved, and achieved from this challenging yet highly impactful research project. Furthermore, I would like to thank many group members who collaborated with me in the research out of my expertise: Chris Sewell, Dr. Gill Biesold, Dr. Yan Yan, Dr. Jiabin Qi, Dr. Hongwei Mi, Dr. Shumeng Hao, Dr. Xun Cui, Dr. Likun Gao, Dr. Yuelan Zhang. Also, I would like to thank Dr. Meng Zhang, Dr. Shiqiang Zhao, Dr. Chuntao Lan, Dr. Fan-wei Liu, Dr. Jiawei Zhang, Dr. Cheng-Hsin Lu, Matt Rager, Dr. Wenran Wang, Dr. Aurelia Wang, Dr. Bing Wang, Dr. Hanyin Zhang, Dr. Songru Jia, Dr. Meidan Ye, Dr. Wendan Xue, Rachel Lawless, Ariany Bonadio, we come from different places all over the world and form a big family at Tech, I cherish all the memories we have made together.

Outside our lab, I also want to thank many people who helped me and supported me. I want to thank Dr. Wensi Chen, for the collaboration in my antibacterial nanocomposite project. I must mention my close friendship with Zhijian Sun, Anqi Jian, Dr. Weilin Zhang, Dr. Fujia Wang, Yifan Liu, Zhaonan Liu, Yifan Ma, Junhe Chen, Dr. Zhiheng Lyu, Dr. Hong Hong, Dr. Jing Zhang, Jiaxiong Li, Dr. Qianqian Chu, Dr. Dong An, Dr. Qing Liu, Dr. Zhijun Liu, Dr. Xirui Peng, Dr. Mingkai Liu, Shiyao Wang, their accompany makes my Ph.D. journey much easier. I also want to thank Dr. Ningxin Jiang, Yanxin Ye, Yiou Zhu, and Dr. Qicheng Tang, we were classmates in high school ten years ago and are still keeping close contact with and encouraging each other while we are pursuing our dreams in USA.

Finally, and the most importantly, I thank my parents, Xinxi Zhang and Chaohong Duan. They have offer me everything they have; I am sure I cannot achieve anything without their unconditional love and support. I am lucky to be their son. I hope I could make them proud of me.

I also want to thank my girlfriend Minju Kim, for offering me love, happiness, courage, and motivation. Her appearance makes all the suffering in the Ph.D. life worth.

TABLE OF CONTENTS

ACKNOWLEDGEMENTS	i
List of Tables	vi
List of Figures	vii
Summary	xii
Chapter 1. Introduction	1
1.1. Colloidal Nanocrystals	1
1.2. Synthesis of Non-linear Star-like and Bottlebrush-like Polymers	3
1.2.1 Synthesis of Star-like Polymer	5
1.2.2. Synthesis of Bottlebrush-like polymers	7
1.3. Nonlinear Block Copolymer as Nanoreactor for Nanocrystal Synthesis	11
1.4. Antibacterial Nanomaterials for Food Packaging Applications	19
Chapter 2. Motivations, Goals and Objectives	21
2.1. Motivations and Goals	21
2.2. Objectives	22
Chapter 3. Ternary Biocidal-Photocatalytic-Upconverting Nanocomposites for Enhanced Antibacterial Activity Preliminary Results	25
3.1. Introduction	25
3.2. Experimental Section	27
3.2.1. Materials	27
3.2.2. Method	28
3.2.3. Characterizations	30
3.3. Results and Discussion	31
3.4. Conclusion	45
Chapter 4. Nanoparticles via Star-like Block Copolymer as Nanoreactor and Their Applications in Electrocatalysis	47
4.1. Introduction	47
4.2. Experimental Section	49
4.2.1. Materials	49
4.2.2. Methods	50
4.2.3. Characterization	52
4.2.4. Synthesis of 0D Nanoparticles	52
4.3. Results and Discussion	54

4.4. Conclusion	72
Chapter 5. Synthesis of Bottlebrush-like Block Copolymer as Nanoreactor for 1D Nanorods	73
5.1. Introduction	73
5.2. Experimental Section	74
5.2.1. Materials	74
5.2.2. Methods	74
5.2.3. Characterization	77
5.3. Results and Discussion	78
5.4. Conclusion	88
Chapter 6. Reversible Photo Crosslinkable 2D Organic-Inorganic Metal Halide Perovskite Nanoplates for Advanced Optoelectronic Devices	89
6.1. Introduction	89
6.2. Experimental Section	90
6.2.1. Materials	90
6.2.2. Methods	91
6.2.3. Characterization	92
6.3. Results and Discussion	92
6.4. Conclusion	99
Chapter 7. General Conclusions and Broader Impacts	101
7.1. General Conclusions	101
7.2. Broader Impacts	103
Dissemination of Work	107
References	110

List of Tables

Table 3.1	Comparison of <i>E. coli</i> reduction percentage with and without UV filter	38
Table 4.1	Molecular Weight of PtBA- <i>b</i> -PS star-like block copolymers	59
Table 4.2	Molecular Weight of PAA- <i>b</i> -PS star-like block copolymers	60
Table 5.1	Molecular Weight of PtBA- <i>b</i> -PS bottlebrush-like block copolymers	82
Table 5.2	Reaction Parameter Tuning of ATRP of Bottlebrush PtBA	86

List of Figures

Figure 1.1	(a) Scheme and TEM image of a CdSe/ZnS core-shell nanoparticle; (b) change in energy levels with increasing core size; (c) scheme, photograph, and photoluminescent spectrum showing progressive color change of the nanoparticles with increasing core size.	2
Figure 1.2	(a) Schematic illustration of the star-like polymers. (b) Core-first and arm-first strategies for the synthesis of star-like polymers.	4
Figure 1.3	Examples of sophisticated architectures of bottlebrush polymers.	8
Figure 1.4	Illustration of the three approaches for the synthesis of BBPs.	8
Figure 1.5	(a) Synthesis strategies for perovskite nanocrystals using amphiphilic block copolymer micelles as nanoreactors; (b) molecular structure of a fourth-generation phenylazomethine dendrimer and STEM image of an $\text{In}_{12}\text{Sn}_{16}\text{Ox}$ nanoparticle made from the dendrimer.	13
Figure 1.6	Schematic representation of synthetic strategies for nanoparticles with different architectures ((a) solid, (b) core-shell and (c) hollow) using star-like block copolymers as nanoreactors with the corresponding TEM images of solid Au nanoparticle, Au-TiO ₂ core-shell nanoparticle, and Au hollow nanoparticle respectively.	14
Figure 1.7	TEM images of different types of nanoparticles synthesized using star-like block copolymer as nanoreactors.	16
Figure 1.8	Schematic representation of synthetic strategies for (a) plain, (b) core-shell, and (c) hollow nanorods using bottlebrush-like block copolymers as nanoreactors with the corresponding TEM images of solid Au nanorod, Au-Fe ₃ O ₄ core-shell nanorod, and Au nanotube (hollowed nanorod) respectively.	18
Figure 1.9	(a) Modes of action of Ag NPs on bacteria. (b) Electronic structure of semiconductor and generation of ROS from photocatalytic reactions (top); Diagram of ROS' action on bacteria (bottom)	20
Figure 3.1	(a-c) TEM images of (a) Au NPs, (b) TiO ₂ NPs, and (c) UCNPs dispersed in water. (d) UV-vis absorption spectrum of Ag NPs. (e) XRD profiles of Ag, TiO ₂ , and UCNPs.	32
Figure 3.2	TEM images of synthesized (a) TiO ₂ NPs, and (b) UCNPs dispersed in hexane. Digital image of (c) TiO ₂ NPs and (d) UCNPs solutions before and after ligand exchange.	33
Figure 3.3	(a) UV-vis absorption spectra of TiO ₂ NPs before and after ligand exchange. (b) Upconversion spectra of UCNPs before and after ligand exchange. (c)	35

Tauc plot obtained from UV-vis absorption spectra of TiO₂ NPs and Ag/TiO₂ nanocomposites in water.

Figure 3.4	(a) Digital image of test sample under solar simulator; IR image showing temperature of samples under irradiation for (b) 0 min, (c) 15 min, and (d) 30 min.	37
Figure 3.5	Comparison of antibacterial performance of Ag NPs, Ag/TiO ₂ NPs nanocomposites, and Ag/TiO ₂ /UCNP NPs nanocomposite against <i>E. coli</i> in dark, under ambient light, and under solar simulator equipped with a UV filter (i.e., removal of UV photons).	39
Figure 3.6	Comparison of antibacterial performance of ternary nanocomposite systems with different compositions against <i>E. coli</i> .	41
Figure 3.7	(a) Energy level diagram of NaYF ₄ @Yb:Tm NPs. (b)Antibacterial mechanism of the ternary Ag/TiO ₂ /β-NaYF ₄ @Yb:Tm UCNP nanocomposite system.	41
Figure 3.8	(a) Absorption spectra depicting photodegradation of RhB by the ternary nanocomposites aqueous solution in the absence of trapping scavenger under solar simulator with a UV filter. (b) Photodegradation of RhB as a function of time with no trapping scavenger, EDTA, BQ, and IPA, respectively.	43
Figure 3.9	Change in UV-Vis absorption spectra of RhB in the ternary nanocomposites solution in the presence of BQ, EDTA, and IPA.	43
Figure 3.10	(a) Stress-strain curves of TEMPO-oxidized CNF-based nanocomposite films with 0 wt%, 1wt%, 5wt%, and 10wt% of the ternary Ag/TiO ₂ /UCNP nanocomposites. (b-d) Digital images of disc diffusion antibacterial tests of the CNF/Ag/TiO ₂ /UCNP nanocomposite films (b) in dark, (c) under ambient light, and (d) solar simulator with UV filter.	45
Figure 4.1	Schematic illustration of the synthesis of star-like nonlinear block copolymer (i.e., star-like PAA- <i>b</i> -PS) nanoreactor.	50
Figure 4.2	¹ H NMR spectrum of the Br-β-CD macroinitiator.	55
Figure 4.3	GPC traces of (a) PtBA star-like polymers; and (b) PtBA- <i>b</i> -PS star-like block copolymers.	56
Figure 4.4	Typical ¹ H NMR spectrum of the PtBA star-like polymer.	57
Figure 4.5	Typical ¹ H NMR spectrum of the PtBA- <i>b</i> -PS star-like block copolymer.	58
Figure 4.6	FT-IR spectra of PtBA- <i>b</i> -PS and PAA- <i>b</i> -PS star-like polymers.	60

Figure 4.7	TEM images of CFO nanoparticles synthesized with PAA- <i>b</i> -PS star-like nanoreactor. (a) and (b) are 6.5 nm CFO nanoparticles using PAA- <i>b</i> -PS-1; (c) and (d) are 10 nm CFO nanoparticles using PAA- <i>b</i> -PS-4.	61
Figure 4.8	Digital images of CFO nanoparticles made from PAA- <i>b</i> -PS-4 dispersed in toluene. The nanoparticles can be attracted by magnet placed near the vial and redispersed in toluene easily by hand shaking.	62
Figure 4.9	TEM images of metal oxide nanoparticle synthesized using PAA- <i>b</i> -PS nanoreactors. (a) 12.5 nm NFO nanoparticles synthesized with PAA- <i>b</i> -PS-4. (b) 7.3 nm Fe ₃ O ₄ nanoparticles using PAA- <i>b</i> -PS-1; (c) and (d) 13.6 nm BTO nanoparticles using PAA- <i>b</i> -PS-4.	63
Figure 4.10	TEM images of (a) 13.6 nm Au nanoparticle synthesized using PAA- <i>b</i> -PS-4; and (b) 12.6 nm CsPbBr ₃ perovskite nanoparticles synthesized with PAA- <i>b</i> -PS-4.	64
Figure 4.11	CsPbBr ₃ nanoparticle dispersed in toluene and store in lab for (a) 2 months and (b) 10 months. The nanoparticles prepared using star-like nanoreactors show excellent stability.	65
Figure 4.12	TEM images of as synthesized CFO NPs reacted for (a) 2 hours, (b) 5 hours, (c) 8 hours, and (d) 12 hours at 250 °C, without template.	67
Figure 4.13	TEM images of as synthesized CFO NPs reacted for (a) 2 hours, (b) 5 hours, (c) 8 hours, and (d) 12 hours at 250 °C, using PAA- <i>b</i> -PS-1 as nanoreactor.	68
Figure 4.14	TEM images of CFO NPs synthesized (a) without template and (b) using PAA- <i>b</i> -PS-1 as nanoreactor after storing in THF for overnight and centrifugation at 6000 rpm for 10 minutes. Insets are digital images of NP dispersion in THF after overnight storage, showing the supreme dispersity of PS-ligated CFO NPs in THF.	68
Figure 4.15	TEM images of CFO NPs synthesized (a) without template and (b) using PAA- <i>b</i> -PS-1 as nanoreactor after storing in THF for overnight and centrifugation at 6000 rpm for 10 minutes. Insets are digital images of NP dispersion in THF after overnight storage, showing the supreme dispersity of PS-ligated CFO NPs in THF.	69
Figure 4.16	Illustration of the two-step surface reconstruction process.	70
Figure 4.17	TEM images of PS ligated CFO NPs before (left column) and after (right column) S-doping at different reaction conditions. NP size changed from 9.6±1.1 nm to 6.5±1.4 nm when S-doping was conducted at 100 °C for 5 minutes (a); NP size remain almost unchanged when reaction temperature is lowered to 70°C and kept for 1 (b) or 2 minutes (c).	70

Figure 4.18	The linear sweep voltammetry (LSV) curve of CFO NPs after surface reconstruction.	71
Figure 4.19	(a) Nyquist plots for pure nickel foam, surface reconstructed CFO NPs on NF, and surface reconstructed CFO NPs after magnetization obtained from electrochemical impedance spectroscopy. (b) LSV curves of surface reconstructed CFO NPs before and after magnetization.	72
Figure 5.1	Schematic illustration of the synthesis of bottlebrush-like block copolymer (i.e., bottlebrush-like PAA- <i>b</i> -PS) nanoreactor.	75
Figure 5.2	¹ H NMR spectrum of the cellulose-Br macroinitiator.	79
Figure 5.3	(a) GPC traces of cellulose-Br macroinitiators; (b) GPC traces of bottlebrush-like PtBA and PtBA- <i>b</i> -PS.	80
Figure 5.4	Typical ¹ H NMR spectrum of the PtBA bottlebrush-like polymer.	81
Figure 5.5	Typical ¹ H NMR spectrum of the PtBA- <i>b</i> -PS bottlebrush-like block copolymer.	82
Figure 5.6	FT-IR spectra of PtBA- <i>b</i> -PS and PAA- <i>b</i> -PS bottlebrush-like polymers.	83
Figure 5.7	Examples of bottlebrush-like PtBA polymers with tailing in their GPC curves.	85
Figure 5.8	AFM images show the 1D worm-like morphology hydrolyzed Cell9K-PtBA113k-PS300k nanoreactor.	88
Figure 6.1	¹ H NMR spectra of (a) 7-amino-4-methylcoumarin and (b) 7-ammonium-4-methylcoumarin halides (chloride in the upper panel, bromide in the center panel, and iodide in the lower panel).	93
Figure 6.2	(a) UV-vis absorption and (b) PL spectra of as synthesized C ₂ PbX ₄ nanoplatelets. (c) UV-vis absorption and (b) PL spectra of three as synthesized C ₂ PbBr ₄ nanoplatelets batches, showing poor reproducibility.	94
Figure 6.3	XRD patterns of pure BA ₂ PbBr ₄ 2D perovskite and 2D perovskite made from mixed A cations consisted of coumarin containing A cation and BABr at different ratios.	95
Figure 6.4	TEM images of (a) BA ₂ PbBr ₄ nanoplatelets and (b) nanostructures resulted from synthesis using BA:coumarin 1:1 mixed A cations.	96
Figure 6.5	¹ H NMR spectrum of (a) 7-hydroxyl-4-methylcoumarin, (b) 4-methylcoumarin-7-O-propyl-Boc, and (c) 4-methylcoumarin-7-O-propyl-ammonium bromide.	97

- Figure 6.6 UV-vis absorption and PL emission spectra of coumarin containing A cations 98
with (a) ethyl (b) propyl (c) butyl group as spacers and 2D perovskites
synthesized from coumarin containing A cation with (d) ethyl (e) propyl (f)
butyl group as spacers.
- Figure 6.7 TEM images of coumarin containing 2D perovskite nanoplatelets using 99
coumarin containing A cations with (a) ethyl (b) propyl and (c) butyl groups
as spacers.

Summary

The ability to produce monodisperse nanocrystals with stable and tunable surface chemistry is of key importance to render investigation into their size- and shape-dependent physical properties and thus an array of applications including electronics, photonics, catalysis, sensors, energy storage, information technology, bionanotechnology, etc. In this context, nonlinear block copolymer nanoreactor has emerged as a general and robust route to synthesis of a gallery of nanocrystals with precisely controlled sizes, shapes, compositions, and surface chemistry. In this thesis, I capitalized on a set of rationally designed star-like and bottlebrush-like block copolymer to template the growth of a host of functional 0D and 1D nanocrystals with controlled dimensions, compositions, and architectures, and scrutinize the dependence of physical properties and energy-related applications on their size, shape, and surface chemistry.

First, a series of star-like copolymers were synthesized via sequential atom transfer radical polymerization (ATRP) of tert-butyl acrylate (tBA) and styrene from star-like macroinitiators, brominated β -cyclodextrin (β -CD). Due to the living nature of ATRP, the molecular weight of each polymer block can be precisely controlled by simply tuning polymerization time and a low polydispersity index (PDI) can be achieved. The inner hydrophobic poly(tert-butyl acrylate) (PtBA) blocks were then converted into hydrophilic poly(acrylic acid) (PAA), which strongly coordinates with the metal moieties of precursors of targeted nanocrystals, leading to the nucleation and growth of nanocrystals confined within the space occupied by the PAA blocks. As a result, the size and shape of nanocrystals can be readily controlled by the molecular weight of PAA blocks (i.e., diameter of nanoparticles). Moreover, the outer PS blocks, originally covalently linked to the inner

PAA blocks, form a layer of permanently anchored ligands on the nanocrystal surface to enable stable surface chemistry. This synthetic strategy were successfully applied for preparing a diversity of functional nanoparticles for the investigation into their physical properties and applications. Specifically, this judiciously designed nanoreactor was utilized to craft monodispersed magnetic spinel CoFe_2O_4 nanoparticles, which was studied for their magnetic and surface chemistry related electrocatalytic activity. It was the first systematic scrutiny of the influence of spin-pinning effect in spinel nanoparticles realized via surface reconstruction on the oxygen evolution reaction (OER).

Second, using the same chemistry, 1D bottlebrush-like PAA-b-PS templates can be realized by employing brominated cellulose (Cell-Br) as macroinitiators. Due to the larger number of side chains on one Cell-Br macroinitiator (ranging from about 40 chains to more than 150 chains), high quality bottlebrush-like block copolymers are more challenging to synthesize than star-like block copolymers, which only have 21 arms. Systematic scrutiny was made to investigate the reaction conditions (e.g., catalyst ratio, ligand ratio, reaction concentration, degassing method, etc.) that affect the uniform growth of the highly dense block copolymer side chains, which has a determining effect on the quality of the bottlebrush-like templates and their application as nanoreactors for the synthesis of 1D nanocrystals.

In addition to focusing on the precise synthesis of 0D and 1D nanocrystals via nanoreactor strategy, this thesis also covers the practical application of multi-functional nanocomposites. In this work, a ternary nanocomposite consisting of antibacterial silver (Ag) NPs, photocatalytic titania oxide (TiO_2) NPs, and upconverting NPs are prepared, manifesting a greatly enhanced biocidal performance under ambient environment. It was found that the visible light (blue) and ultraviolet (UV) light which were converted from near infrared (NIR) radiation by the $\text{NaYF}_4@\text{Yb:Tm}$ upconverting NPs can be effectively absorbed by Ag and TiO_2 NPs to generate

electrons and electron-hole pairs, respectively. Reactive oxygen species (ROS) could then be produced from the reactions between environment and the electrons and holes to terminate bacteria. The outstanding antibacterial performance of this nanocomposite system renders it the potential to be used in food packaging industry.

Moreover, reversible photo responsive Ruddlesden-Popper 2D perovskite nanoplatelets were explored in this thesis. Colloidal two-dimensional RP perovskite nanoplatelets with a general formula $L_2(ABX_3)_{n-1}BX_4$ are a rapidly emerging type of semiconductor materials with excellent optical and electronic properties. Research on the functional organic spacers (L) has become a popular direction in the past several years. Inspired by our previous research about reversible photo-crosslinkable nanoparticles realized by capitalizing on star-like nanoreactors with photo responsive coumarin containing repeat units in the outer block, the preparation of RP lead halide perovskite nanoplatelets with coumarin containing ammonium as organic spacers was attempted. Molecular modification and mixed organic spacer strategies were adopted to overcome the solubility limitation of coumarin containing molecules in non-polar solvents. Such coumarin containing 2D perovskite nanoplatelets will undergo controllable and reversible layer-by-layer crosslinking and de-crosslinking under radiation of certain wavelength, leading to many intriguing and tunable optical and electronic properties.

Chapter 1. Introduction

1.1. Colloidal Nanocrystals

Nanomaterials represent an amazing and broad class of materials with at least one dimension in the range of 1 to 100 nm.¹ The history of utilization of nanomaterials can be dated by to several thousand years ago, when human started to use them for a variety of purpose unknowingly.^{1,2} A famous example is the Lycurgus Cup, a dichroic cup produced by in 4th century A.D. the Romans.³ It shows different color depending on the incident light because of the presence of gold and silver nanoparticles. The modern nanotechnology began since the introduction of the concept by Nobel Prize laureate Richard Feynman in 1959 in his famous speech “There’s plenty of room at the bottom”.⁴ Since 1980s, nanotechnology has undergone rapid development thanks to the invention of advanced techniques that enable the preparation and characterization of nanomaterials.

Colloidal nanocrystals are a specific class of nanomaterials, which are fragments of crystalline lattice of bulk inorganic solids typically in the size range of 2-20 nm.^{5, 6} They have attracted tremendous research attention and been viewed as the hottest research topics of the past decades because of the diverse and tunable properties which are heavily dependent on the size, shape, architecture, composition, and surface chemistry. In this size regime, the electronic structure, magnetic, and optical properties of nanocrystals can be changed by varying the size of nanocrystals because of the quantum confinement effect.^{7, 8} For example, band gap of semiconductor nanocrystals and surface plasmonic resonance of metal nanoparticles (e.g., Au and Ag) can be tuned by simply adjusting their size without changing their composition (**Figure 1.1**).⁹⁻¹¹

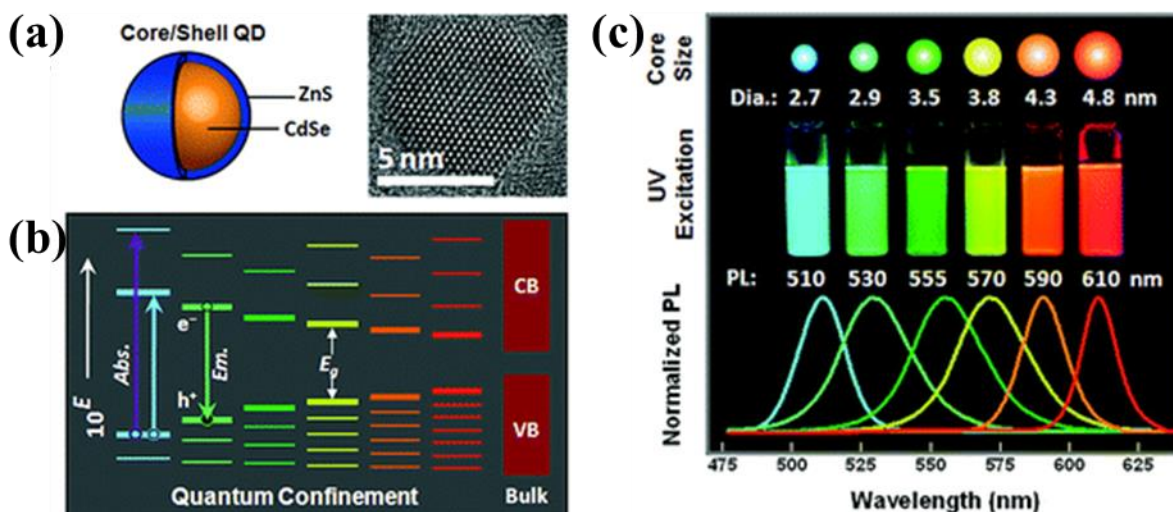


Figure 1.1. (a) Scheme and TEM image of a CdSe/ZnS core-shell nanoparticle; (b) change in energy levels with increasing core size; (c) scheme, photograph, and photoluminescent spectrum showing progressive color change of the nanoparticles with increasing core size.¹²

Typically, a layer of organic or inorganic surfactant (i.e., ligand) is coordinated on the surface of nanocrystals to render good dispersibility and facilitate the control over size and shape of the nanocrystals during the synthesis.^{5, 13} Due to the nature of colloids, these nanocrystals are dispersed in solvents, rendering a solution-processable class of materials that could be scaled up for synthesis and be fabricated into an array of devices for a wide range of applications.¹⁴⁻¹⁶ Ligands play an important role in the synthesis, property, and application of nanocrystals. First, the binding between ligand and surface nanocrystals is crucial in determining the growth kinetics of nanocrystals, and thus their size and shape. For instance, alkyltrimethylammonium bromides (C_n TAB) were used for the synthesis of Au nanorods and the ligand with longer alkyl chain resulted in longer nanorods due to a more stable bilayer of ligand formed on nanorod facilitating the further growth of Au nanorod along the longitudinal direction.¹⁷ Moreover, ligands can also

affect the property of nanocrystals. For example, carrier mobilities of both electrons and holes in PbSe nanocrystal solids decrease exponentially with increasing the length of alkanedithiol ligand.¹⁸ In addition, contour shape of the ligand layer on the nanocrystal surface can be varying types of ligands, which has been shown to influence the assembly of nanocrystals and bring new opportunities in designing nanocrystal-based devices.^{19, 20}

Apparently, the ability to produce monodisperse nanocrystals with stable and tunable surface chemistry is of key importance to render investigation into their size- and shape-dependent physical properties and thus an array of applications including electronics, photonics, catalysis, sensors, energy storage, information technology, bionanotechnology, etc. However, due to the dynamic nature of the interaction between ligands the nanocrystal surfaces, ligands could detach from nanocrystal surfaces during the synthesis, purification, and post-synthesis treatment, lead to decreased colloidal stability, physical properties, and even structure integrity of the nanocrystals.^{21,}
²² On the other hand, sophisticated post synthesis treatments are commonly needed to tune the surface chemistry of nanocrystals to meet requirements for specific applications, limiting the large scale use of the nanocrystals.

1.2. Synthesis of Non-linear Star-like and Bottlebrush-like Polymers

Non-linear polymers represent a unique class of soft materials where polymer side chains are covalently connected to a 0D and 1D center (star-like and bottlebrush-like, respectively). Non-linear block copolymers refer to non-linear polymers whose arms are consisted of more than one blocks. Due to the hyperbranched molecular structure, non-linear polymers take less volume and have lower viscosity compared to their linear counterparts with similar molecular weight.²³ Due

to their radial and cylindrical architecture, star-like and bottlebrush-like polymers are unimolecular micelles.²⁴ Distinct from conventional micelles, which are formed via weak dynamic interaction between linear polymers, the cores and arms in star-like and bottlebrush-like polymers are covalently connected, affording a more robust architecture against environment perturbations (e.g., pH, temperature, solvents, salt, etc).²⁵ Due to the tremendous progress made in polymer chemistry over the past several decades, especially the development in controlled living polymerization, including atom transfer radical polymerization (ATRP)^{26, 27}, reversible addition-fragmentation chain transfer (RAFT) polymerization,^{28, 29} and nitroxide-mediated radical polymerization (NMP)³⁰, non-linear star-like and bottlebrush-like copolymer with well-controlled molecular weight and narrow PDI have been achieved.

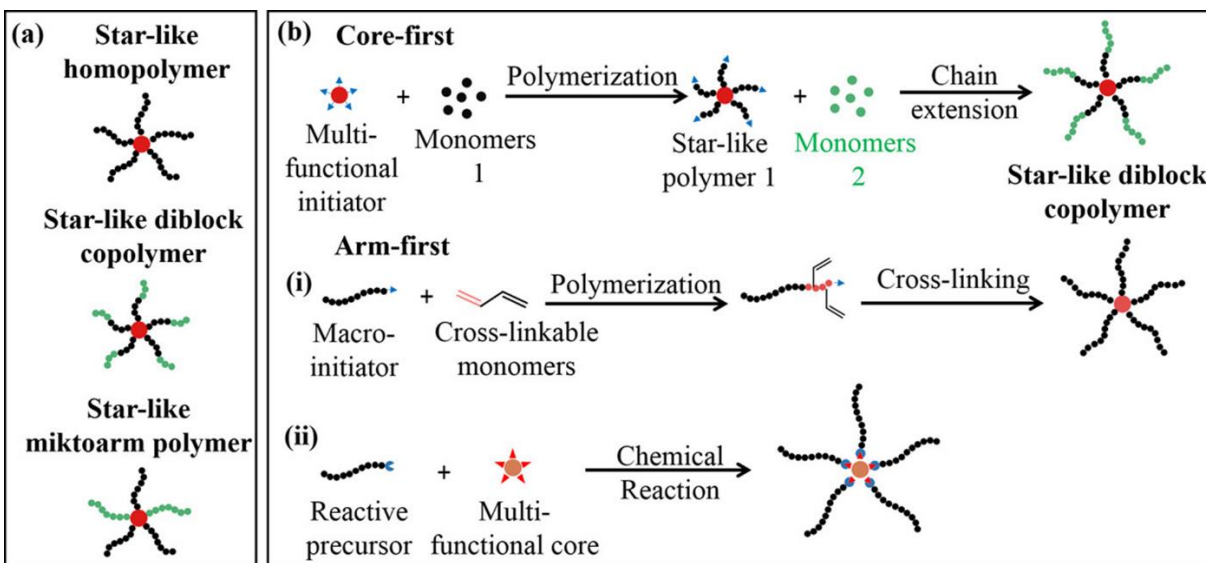


Figure 1.2. (a) Schematic illustration of the star-like polymers. (b) Core-first and arm-first strategies for the synthesis of star-like polymers.²⁵

1.2.1 Synthesis of Star-like Polymer

In general, two routes can be followed to synthesize star-like polymers: (1) core-first and (2) arm-first (Figure 1.2.).^{24, 25} In arm-first method, preformed arm polymers with end-functional groups are connected together via polymerization or coupling reaction or onto a multi-functional core (sometimes also called graft onto method).³¹ A high degree of control over the arm structure can be achieved with arm-first method due to the ability to characterize the linear arms prior to the formation of the star. However, compared to core first method, star-like polymers synthesized via arm-first approach often have broader arm number distributions and low arm-to-star conversion.³² The quality of star-like polymers prepared through this method is largely influenced by many parameters, including degree of polymerization of the arms, composition of the arms, composition of cross-linker and multifunctional cores, and the ratio between arms and cross-linkers and cores.³³ Such drawbacks greatly limit the further development this method.

In contrast to the arm-first method, core-first strategy involves pre-synthesized a multifunctional initiator from which polymer arms are grafted sequentially via controlled/living polymerization to yield a star-like architecture. As a key component in the core-first approach, the core initiators are normally multifunctional molecules, such as cyclodextrin (CD),³⁴⁻³⁶ polyhedral oligomeric silsesquioxane (POSS),^{37, 38} calixarene,^{39, 40} hyperbranched and dendritic polymers.⁴¹⁻

43

Taking β -CD as an example, 21 -OH groups on the β -CD core are brominated and converted into -Br to render a 21 Br- β -CD macroinitiator. Subsequent ATRP of a variety of monomers can then be conducted to form star-like block copolymers. Using this method, a library of star-like polymers has been successfully developed, such as amphiphilic star-like β -CD-*graft*-[poly(acrylic acid)-*block*-polystyrene] diblock copolymer (denoted β -CD-*g*-[PAA-*b*-PS]),⁴⁴

thermoresponsive star-like β -CD-*graft*-[poly(acrylic acid)-*block*-poly(*N*-isopropylacrylamide)] diblock copolymer (denoted β -CD-*g*-[PAA-*b*-PNIPAM]),⁴⁵ photoresponsive star-like β -CD-*graft*-[poly(acrylic acid)-*block*-poly(7-methylacryloyloxy-4-methylcoumarin)] diblock copolymer (denoted β -CD-*g*-[PAA-*b*-PMAMC]),⁴⁶ star-like β -CD-*graft*-[polystyrene-*block*-poly (acrylic acid)-*block*-polystyrene] triblock copolymer (denoted β -CD-*g*-[PS-*b*-PAA-*b*-PS]),⁴⁷ and star-like β -CD-*graft*-[poly(4-vinylpyridine)-*block*-poly (acrylic acid)-*block*-polystyrene] triblock copolymer (denoted β -CD-*g*-[P4VP-*b*-PAA-*b*-PS]).⁴⁸ Moreover, for star-like block copolymers that contain blocks cannot be synthesized via controlled/living polymerization, a combination of ATRP and click reaction could be implemented. Through this way, we have demonstrated star-like β -CD-*graft*-[poly(acrylic acid)-*block*-poly(ethylene oxide)] diblock copolymer (denoted β -CD-*g*-[PAA-*b*-PEO]),⁴⁹ star-like β -CD-*graft*-[poly(acrylic acid)-*block*-poly(3-hexylthiophene)] diblock copolymer (denoted β -CD-*g*-[PAA-*b*-P3HT]),⁵⁰ star-like β -CD-*graft*-[poly(acrylic acid)-*block*-poly(vinylidene fluoride)] diblock copolymer (denoted β -CD-*g*-[PAA-*b*-PVDF]),⁵¹ and star-like β -CD-*graft*-[poly(acrylic acid)-*block*-poly(3,4-ethylenedioxythiophene)] diblock copolymer (denoted β -CD-*g*-[PAA-*b*-PEDOT]).⁵² All these star-like block copolymers composed of hydrophilic inner blocks could be used as nanoreactors for crafting plain, hollow, and core-shell nanoparticles.

Core-first method is capable of synthesizing star-like polymers with precisely controlled arm numbers by designing the number of functionalities in the initiator. Moreover, the composition of the resulting star-like polymers can also be readily tuned by changing monomer species. However, this method is not suitable for the synthesis of miktoarm star-like polymers, which have dissimilar polymer arms, unless initiating cores with orthogonal initiating functionality is used. In addition, the arm polymers of the star-like polymer cannot be characterized directly; more tedious

methods such as cleavage and end-group analysis have to be used.³³ Nevertheless, this strategy has been widely practiced to synthesize star-like block copolymers, which will be demonstrated in Chapter 4 in this thesis.

1.2.2. Synthesis of Bottlebrush-like polymers

Bottlebrush-like polymers (BBPs) represent a class of densely grafted polymers with high molecular weights, in which one or more polymeric side chains are tethered to each repeating unit of a linear polymer backbone.⁵³ Because the densely-packed side chains of the bottlebrush polymers experience significant steric repulsion, BBPs form extended cylindrical shapes.⁵⁴ Such steric repulsion renders an intriguing characteristic to the BBPs: the lack of entanglement (very low backbone entanglement density that can be ignored), which further influences the viscoelastic properties and molecular alignment of BBPs. Moreover, this unique characteristic also endows BBPs with distinctive mechanical and rheological performances (e.g., low entanglement plateau modulus), crystalline abilities (e.g., fast crystal nucleation and slow growth), and stimuli-responsive behaviors (e.g., morphological transformation).⁵³ Owing to the fast development in polymer chemistry, especially the advance in controlled/living polymerization, such as controlled/living radical polymerization,⁵⁵ controlled/living anionic/cationic polymerization,⁵⁶ ring-opening metathesis polymerization,⁵⁷ and click reactions,⁵⁸ BBPs with sophisticated molecular architectures have been achieved as demonstrated in Figure 1.3..

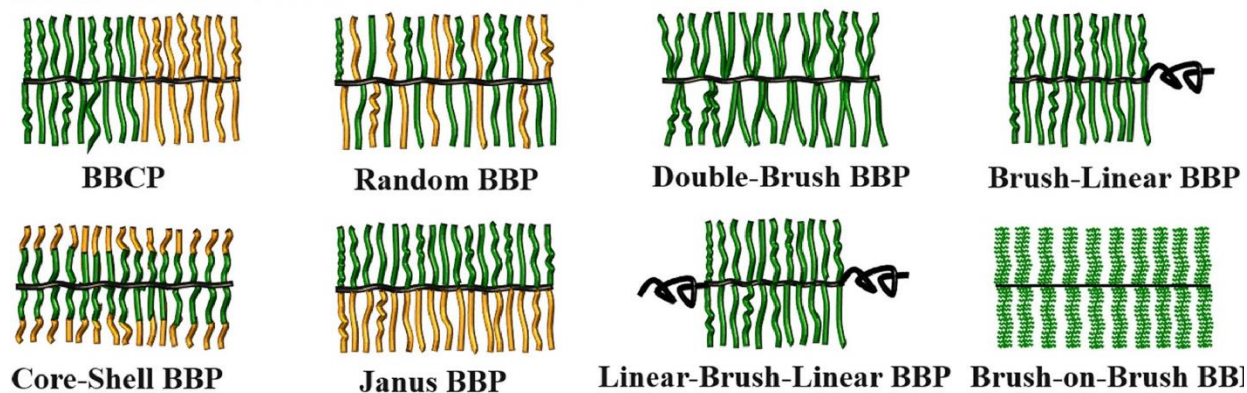


Figure 1.3. Examples of sophisticated architectures of bottlebrush polymers.⁵³

Bottlebrush-like polymers are mostly obtained through three synthetic routes, as shown in **Figure 1.4.**: (1) Grafting-from (i.e., polymerization of side chain monomers from backbone macroinitiator), (2) grafting-through (i.e., polymerization of pre-synthesized side chain macromonomers with functionality at chain ends), and (3) grafting-onto (i.e., attachment of pre-synthesized macromonomers onto backbones).

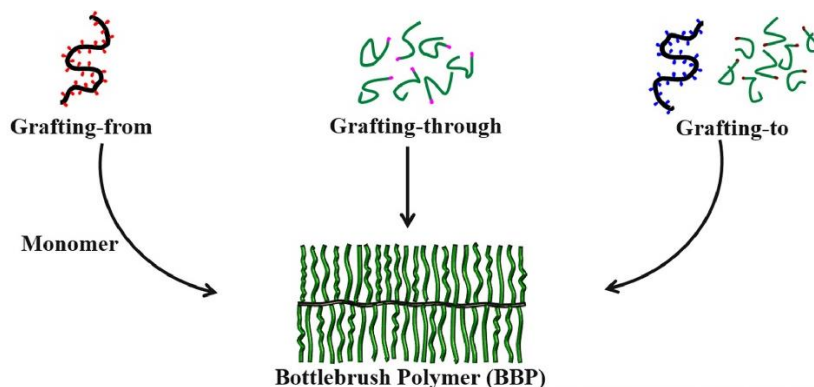


Figure 1.4. Illustration of the three approaches for the synthesis of BBPs.⁵³

In grafting-from approach, the growth of the polymer brushes starts from initiating sites on the polymer backbone. The polyinitiators are prepared by the polymerization of inimers or through post-modification on backbone polymers to introduce the initiating moieties.⁵⁹ A key feature of this method is the high grafting density due to the significantly decreased steric hindrance among the side chains during the growth. High molecular weight side chains could be obtained via grafting-from strategy because the monomers can easily diffuse to the initiator sites as the side chains gradually grow.⁶⁰ However, inter- and intramolecular termination and macroscopic gelation may occur due to the coupling of the densely packed initiating sites during radical polymerization. Such problem could be suppressed by controlled/living radical polymerization which rely on the reversible deactivation radical polymerization (RDRP) to control radical concentration as a low level. Long-backbone BBPs with high grafting density and low PDI can be readily obtained via the grafting-from approach.

A class of unique bottlebrush-like block copolymers has been developed using cellulose as macroinitiators in our lab for the application of nanoreactor to craft 1D nanocrystals.⁶¹ First, cellulose microcrystals were fully dissolved in lab made ionic liquid, which is able to destroy the inter-and intra-molecular hydrogen bonding in cellulose bundles formed due to the tremendously large amount of -OH groups on cellulose backbones.⁶² Esterification reactions will then be conducted to convert all the -OH groups into Br containing ATRP initiating sites. Normally, two esterification processes are need to yield 100% conversion, which is of vital importance in the initiating and polymerization of densely packed side chains to more a rigid 1D structure.⁶³ A series of linear brominated cellulose macroinitiator with narrow distribution in their length could be achieved by performing fractional precipitation. Side chain polymer blocks are then

subsequentially grafted from the cellulose backbone via ATRP to achieved bottlebrush-like core-shell block copolymers including cellulose-*g*-[PtBA-*b*-PS], cellulose-*g*-[P4VP-*b*-PtBA-*b*-PS], and cellulose-*g*-[P4VP-*b*-PtBA-*b*-PS]. When polymer blocks that cannot be prepared by ATRP are involved, such as PEO, click reaction could be utilized to attach the outer block to form the core-shelled bottlebrush such as cellulose-*g*-[PtBA-*b*-PEO] and cellulose-*g*-[P4VP-*b*-PtBA-*b*-PEO]. The hydrophilic inner block P4VP and PAA (obtained from hydrolyzation of PtBA block) can coordinate with metal moieties to form plain, core-shell, and hollow 1D nanocrystals.⁶¹ Compared to conventional colloidal synthesis, where 1D anisotropic structures are normally not favored unless specific ligands are used, this nanoreactor strategy is robust and universal to craft 1D nanocrystals of many different compositions.

Grafting-through method is another rapidly developing approach to synthesize high quality bottlebrush-like polymers. Opposite to grafting from approach, polymer side chains with end functionalities are synthesized first and then polymerized as a macromonomers through appropriate techniques. Unlike grafting from, linear side chains with low PDI are first synthesized normally via controlled/living polymerization and can be characterized clearly. This method also guarantees a 100% grafting density due to its intrinsic features.⁶⁴ Therefore, graft-through method has been widely implemented to synthesize bottlebrush-like polymers with precisely controlled dimensions and architectures for the investigation of their structure-property relationships. However, despite the ability to yield 100% grafting density, achieving high molecular weight bottlebrush-like polymers via this strategy could be challenging. It is largely resulted from the nature of macromonomers which have higher viscosity and limited solubility. Also, less polymerizable end groups and high steric hinderance of the brushes at the propagating sites are attributed to the low degree of polymerization in the backbone. In addition, as a consequence of

the low conversion, the products obtained from grafting-through approach are usually a mixture of bottlebrush-like and linear polymers. Therefore, tedious fractional precipitation or dialysis are often necessary to remove the unreacted macromonomers.⁵³ Many progress in synthesis of bottlebrush-like polymers via grafting-through has been made in recent years. Particularly, using norbornenyl groups as polymerizable moiety of the macromonomers in graft-through approach has attracted increasing attention due to the quantitative monomer conversion catalyzed by Grubbs' catalyst, high reactivity, and large spacing of the norbornenyl groups which reduces space hinderance and allows higher macromonomer conversion.^{64, 65}

The grafting-to strategy involves both pre-synthesized side chain polymers and backbone polymers with reactive functional moieties and a subsequent attachment of side chains onto reactive sites on the backbone polymers via highly effective coupling reactions. Since the polymers are synthesized independently by appropriate techniques, precisely controlled molecular weight and low PDI could be achieved and characterized before the coupling reaction. However, this method typically suffers from low graft density because of the unfavorable thermodynamic and kinetic barriers. As more side chains are grafted on backbone polymers, increased steric repulsion could limit the movement of unattached side chains towards the active moieties and lead to low graft density.⁶⁶ Such steric hinderance effect is more significant when high molecular weight side chains are attached. In order to achieve high graft density, an excess amount of side chain polymers are usually used in coupling reaction, which causes the need of additional tedious and time-consuming separation processes.⁵³

1.3. Nonlinear Block Copolymer as Nanoreactor for Nanocrystal Synthesis

In order to improve the stability of nanocrystals while maintain their properties for various applications, linear amphiphilic block copolymers and unimolecular dendrimers have been used

as an alternative to conventional small molecule ligands. (**Figure 1.5.**) Linear amphiphilic block copolymers in solutions can aggregated and form organized structures called micelle as a result of interactions between themselves and environment.⁶⁷ These micelles typically contain one block with coordinating groups, such as acrylic acid groups in poly(acrylic acid) (PAA) and vinylpyridine groups in poly(2-vinylpyridine) (P2VP) and poly(4-vinylpyridine) (P4VP), that can interact with precursors of nanocrystals and regulate their crystallization in a confined space.⁶⁸⁻⁷¹ The other blocks of the polymers then serve as organic ligands on the surface of nanocrystals. Since polymer blocks are covalently and permanently connected, those ligands will not dissociate from nanocrystals. Dendrimers are a class of complex monodisperse macromolecules with highly branched three-dimensional architecture and well-define chemical structure.^{72, 73} Similar to forming nanocrystals in micelles, precursors are coordinated with binding groups inside the dendrimers (usually imide and amide groups) and then crystalized under certain conditions.⁷⁴⁻⁷⁶ However, these methods still have their own drawbacks. Dynamically stabilized micelles formed by linear block copolymers may deform and disassemble as a result of environmental stimuli including pH, temperature, solvent, etc.⁷⁷ Dendrimers, on the other hand, can only produce very small nanoparticles (<5nm in most cases) due to the difficulty in preparing high generation dendrimers.

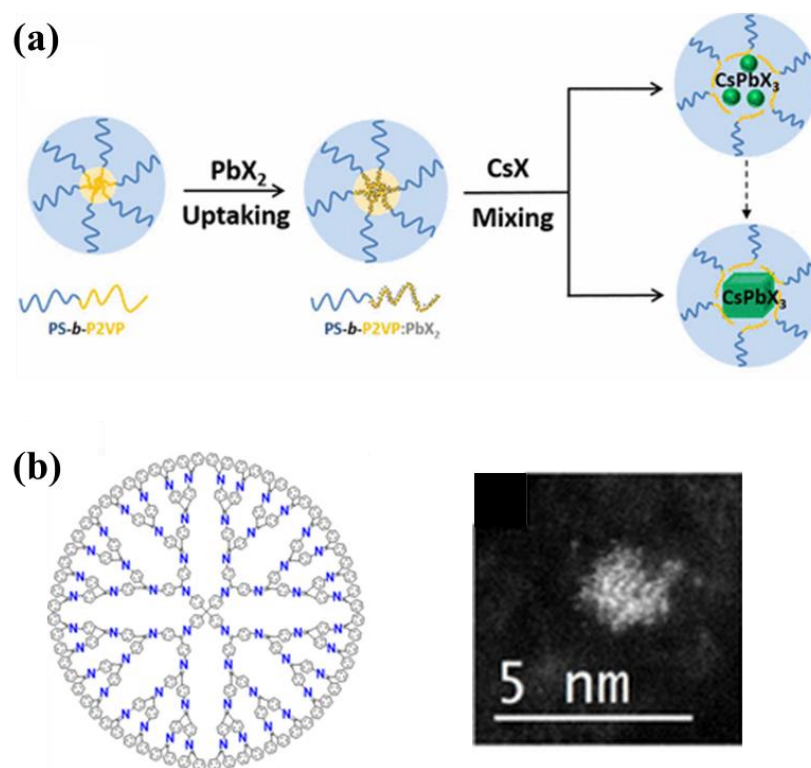


Figure 1.5. (a) Synthesis strategies for perovskite nanocrystals using amphiphilic block copolymer micelles as nanoreactors;⁷⁸ (b) molecular structure of a fourth-generation phenylazomethine dendrimer and STEM image of an $\text{In}_{12}\text{Sn}_{16}\text{O}_x$ nanoparticle made from the dendrimer.⁷⁹

In this regard, Lin group has developed a general and robust strategy to capitalize on unimolecular nonlinear block copolymer micelles as nanoreactors for the synthesis of uniform colloidal 0D and 1D nanocrystals with well-controlled size, shape, composition, and architecture.^{61,}

⁸⁰ Unlike conventional micelles formed by linear block copolymers, nonlinear block copolymers are composed of amphiphilic block copolymer arms covalently connected to the core or backbone and form a thermodynamically stable micelle. Due to the stable and well-defined molecular structure of the nonlinear block copolymers, they are used as nanoreactors for inorganic

nanocrystals. The size and shape of the nanocrystals can be readily controlled by the space taken coordinating blocks which is determined by the molecular weight of the polymer blocks and the morphology of the nanoreactor. Additionally, outer block polymers are covalently bonded to the inner block, forming a permanent polymer layer on the surface of nanocrystals formed inside nanoreactors. The permanently ligated polymer chains provide superior stability of the nanocrystals. Meanwhile, length and chemical composition of the outer block polymers also play a role in determining the property and functionality of the nanocrystals.

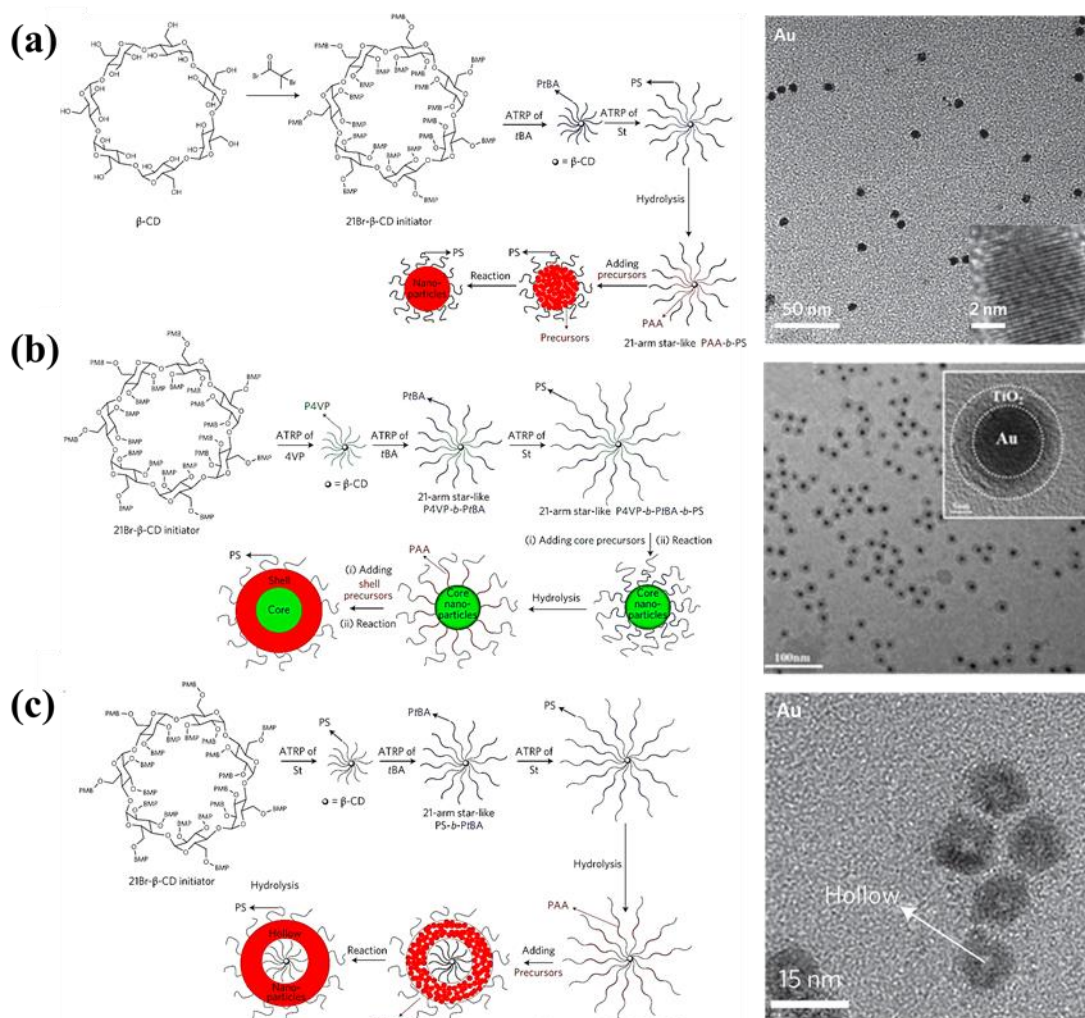


Figure 1.6. Schematic representation of synthetic strategies for nanoparticles with different architectures ((a) solid, (b) core-shell and (c) hollow) using star-like block copolymers as nanoreactors with the corresponding TEM images of solid Au nanoparticle, Au-TiO₂ core-shell nanoparticle, and Au hollow nanoparticle respectively.^{48, 80}

As shown in **Figure 1.6.**, a star-like block copolymer can be synthesized from β -cyclodextrin (β -CD). The 21 hydroxyl groups on β -CD are firstly converted into bromine as initiation sites for sequential atom transfer radical polymerization (ATRP). *Tert*-butyl acrylate (*t*BA), 4-vinylpyridine (4VP), and styrene are monomers used to form the star-like deblock and triblock copolymers. The number and chemical composition of blocks are dependent on the morphologies of particles one would like to obtain in the end. Star-like PAA-*b*-PS, obtained from hydrolysis of *Pt*BA blocks in star-like *Pt*BA-*b*-PS, was used for form plain nanoparticles with the outer block PS capped on the surface. Core-shell and hollowed nanoparticles can also be realized by using star-like PAA-*b*-P4VP-*b*-PS and PS-*b*-PAA-*b*-PS triblock copolymer, respectively. The diameter and shell thickness of the nanoparticles can be readily controlled by the molecular weight of first and second blocks which can be tuned by reaction time. A gallery of uniform nanoparticles has been successfully crafted by using the star-like nanoreactor strategy as displayed in **Figure 1.7.**, proving that this method is very general and robust.

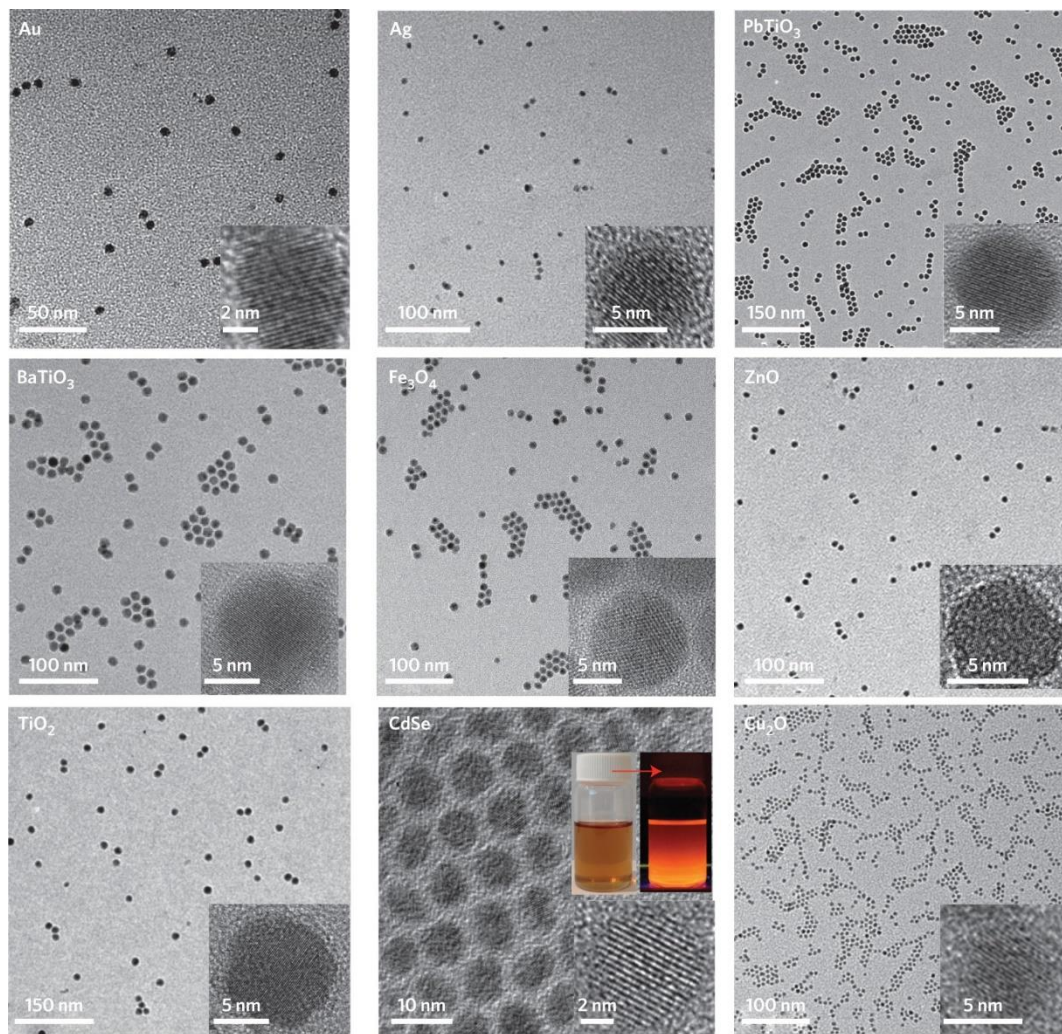


Figure 1.7. TEM images of different types of nanoparticles synthesized using star-like block copolymer as nanoreactors.⁸⁰

Moreover, this method can be extended to craft anisotropic 1D nanorods when star-like nanoreactors are switched to bottlebrush-like nanoreactors. As illustrated in **Figure 1.8.**, cellulose molecule, instead of β -CD, is used as initiator for the bottlebrush-like nanoreactor. Following similar synthetic route to prepare star-like nanoreactor, hydroxyl groups on cellulose backbones are brominated to initiate sequential ATRP of P*t*BA, P4VP, and PS blocks depending on the

targeted nanorod morphology. The length of nanorods is determined by the molecular weight of brominated cellulose initiator while the diameter and shell thickness of the nanorods are again controlled by the molecular weight of first and second blocks.

This nanoreactor-assisted synthetic approach can be utilized for synthesizing a rich diversity of inorganic nanomaterials, especially with complicated composition and structure, which could be hardly made with conventional methods. Moreover, the ability to control the size, shape, dimension, composition, and surface chemistry of nanocrystals of the nanoreactor strategy open up opportunities to investigate size-, shape-, composition- dependent physical properties of nanocrystals.

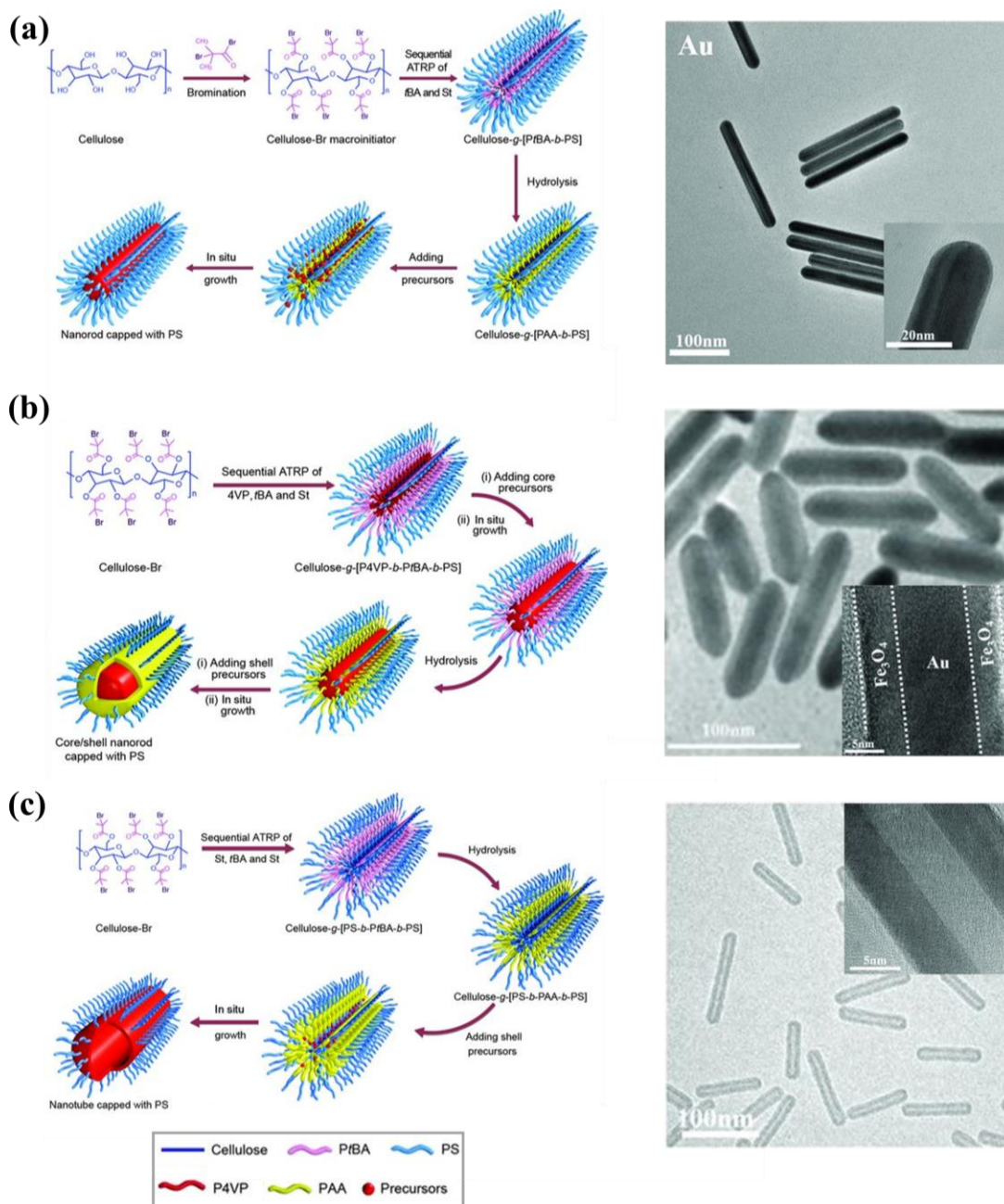


Figure 1.8. Schematic representation of synthetic strategies for (a) plain, (b) core-shell, and (c) hollow nanorods using bottlebrush-like block copolymers as nanoreactors with the corresponding TEM images of solid Au nanorod, Au-Fe₃O₄ core-shell nanorod, and Au nanotube (hollowed nanorod) respectively.⁶¹

1.4. Antibacterial Nanomaterials for Food Packaging Applications

Nanocrystals have been used in a wide range of applications in our daily life due to their diverse properties. Antibacterial property is one of the many interesting and important properties of nanomaterials that enable them to be used for bacterial infection treatment as an alternative to antibiotics. A fast-developing area in research and industry is to use biocidal nanomaterials for antibacterial food packaging as a solution to food safety issues. Among all the nanomaterials, metallic Ag nanoparticles and semiconducting metal oxide nanoparticles (e.g., TiO₂, ZnO, and MgO NPs) are the most studied active antibacterial agents. Ag nanoparticles are known to possess highly efficient antibacterial activity for Gram-positive and Gram-negative bacteria.⁸¹⁻⁸⁴ Although the antibacterial mechanisms of Ag NPs are still not fully understood, several theories on the microbicidal effect of Ag NPs have been proposed.⁸⁵ First, Ag NPs can anchor to and penetrate the bacterial cell wall, thereby causing structural changes in the cell membrane and leading to the death of the cell.⁸⁶ In addition, it has been reported that when Ag NPs are in contact with bacteria, the NPs can form free radicals which are capable of damaging the cell membrane and ultimately cause the cell death.^{87, 88} It has also been proposed that silver ions released from NPs have the ability to interact with the thiol groups present in many vital enzymes, inactivate them, and generate reactive oxygen species (ROS) that attach to the cell.^{89, 90} Moreover, researchers have claimed that silver, as a soft acid, tends to react with sulfur and phosphorus (which are soft bases and major components of cells) and DNA and thus terminate the microbes.^{91, 92} Ag NPs have also been found to be able to modulate and inhibit signal transduction in bacteria and stop cell growth (**Figure 1.9 a**).⁹³ Despite excellent antimicrobial performance, safety concerns over the potential nanotoxicity of Ag to human body greatly limit their commercialization.⁹⁴⁻⁹⁶ Notably, semiconducting NPs can also create ROS to terminate bacteria via photocatalytic reaction under irradiation (generally UV light), as shown in **Figure 1.9 b**. Unfortunately, the need for UV to

trigger photocatalytic reaction represents a significant barrier towards practical application of this class of nanomaterials as UV photons are able to deteriorate food quality, particularly for meat products.^{97, 98} Nonetheless, the implementation of Ag and TiO₂ NPs together displayed improved antibacterial efficiency due to a series of synergic effects, including Ag reduces electron-hole recombination in TiO₂ under UV light by trapping photogenerated electrons which can then generate ROS,^{99, 100} and electron transfer from Ag NPs, as a result of their surface plasmonic resonance under visible light, to the conduction band of TiO₂ where ROS can be generated.¹⁰¹⁻¹⁰³

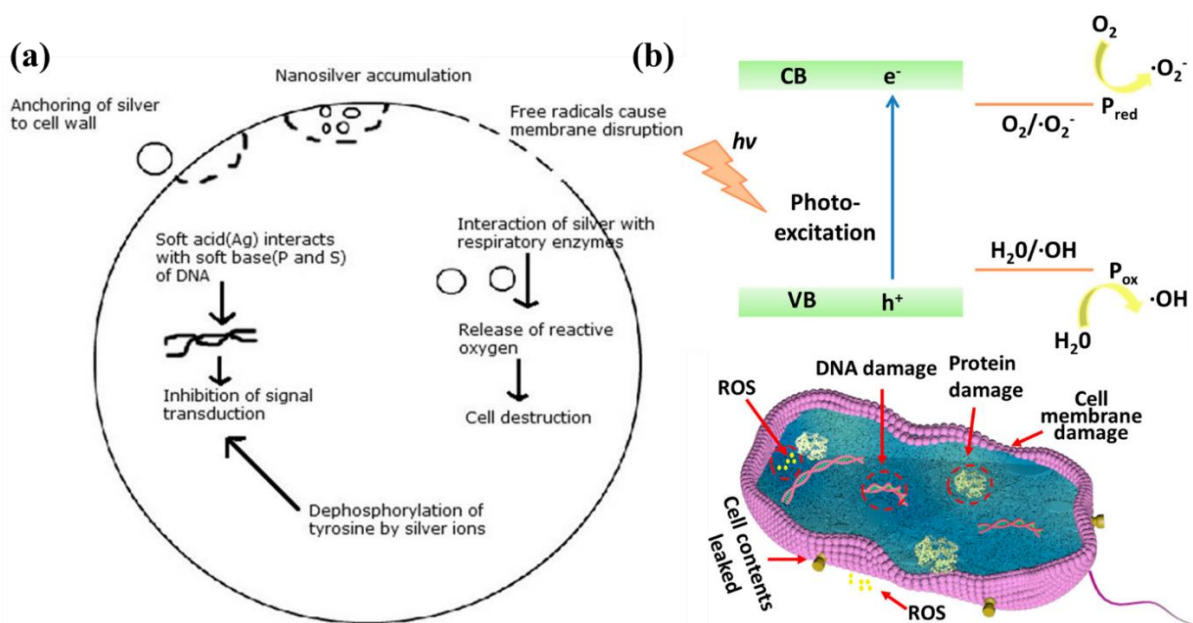


Figure 1.9. (a) Modes of action of Ag NPs on bacteria.¹⁰⁴ (b) Electronic structure of semiconductor and generation of ROS from photocatalytic reactions (top); Diagram of ROS' action on bacteria (bottom).¹⁰⁵

Chapter 2. Motivations, Goals and Objectives

2.1. Motivations and Goals

Colloidal nanocrystals possess a variety of intriguing properties that are contingent upon their size, shape, composition, and surface chemistry. The past several decades have witnessed the rapid development in conventional synthetic methods for controlled synthesis of a great number of nanocrystals, which enables the investigation into their dimension-dependent properties and exploration of their applications.

However, as discussed in Chapter 1, conventional synthetic methods using ligands to cap on the surface of nanocrystals have their limitations. In particular, dissociation of ligands from nanocrystal surface as a result of weak interaction, which can be interrupted under many stimuli, often cause deterioration in their chemical integrity, physical properties, stability, and practical applications. The other challenge the conventional methods is facing is the synthesis of 1D nanocrystals. Although some nanorods such as Au, Fe₃O₄, and metal halide perovskite have been demonstrated, a general strategy to synthesize more 1D nanocrystals is lacking. It is largely due to the difficulty in identifying appropriate ligands that can selectively cap certain facets of nanocrystal and lead to anisotropic growth of the nanocrystals.

A specific example of the restricted application of nanocrystals is the use of nanomaterials for antibacterial food packaging. Potential toxicity of Ag nanoparticles and the need of UV irradiation for TiO₂ nanoparticles have significantly limited their application in food packaging industry. Reducing the use of Ag and UV lights while keeping good antibacterial performance is a promising direction of related research.

Our broad interests in low dimensional nanomaterials also led us to the investigation of functional 2D perovskites. We have gained experience in using responsive polymers containing responsive functional groups in each repeating unit to adjust the functionality of nanoparticles synthesized via our nanoreactor strategy. Here, we aim to move on step further and utilize our experience to synthesize responsive 2D perovskites, which could find great potential in a vast range of areas such as optoelectronic devices and energy related applications.

Therefore, the overall goal of my thesis is to (1) craft a set of 0D and 1D nanocrystals with tunable sizes, shapes, and compositions via nonlinear block copolymer nanoreactor strategy. (2) Scrutinize their dimension-dependent physical properties (magnetic, catalytic, photothermal, etc.) upon the success in producing these nanocrystals. (3) Explore new responsive 2D perovskite nanocrystals using knowledges gained from functional nanoreactors.

2.2. Objectives

- Ternary nanocomposite for antibacterial applications

(1) Prepare ternary antibacterial nanocomposite consisting of Ag nanoparticle, TiO_2 nanoparticle, and UCNPs

(2) Investigate their composition-dependent antibacterial property under different lighting conditions

(3) Produce antibacterial films using the ternary nanocomposite and cellulose nanofibrils for food packaging application

- Nanoparticles via star-like diblock copolymer nanoreactors
 - (1) Rationally design and synthesize star-like block copolymer nanoreactor with well-controlled molecular weight and narrow molecular weight distribution
 - (2) Craft uniform 0D nanoparticles (with a focus on CoFe_2O_4 (CFO) nanoparticles) via star-like block copolymer nanoreactor synthesized in (1)
 - (3) Explore the size effect of CFO nanoparticles and CFO (core)-PS (shell) ratio on the electrocatalytic property.
 - (4) Study the magnetic field enhancement in the OER activity of the surface reconstructed $\text{CFO}/\text{CoFe}_2\text{O}_x\text{H}_y$ NPs
- Nanorods via bottlebrush-like diblock copolymer nanoreactors
 - (1) Rationally design and synthesize bottlebrush-like block copolymer nanoreactor with well-controlled molecular weight and narrow molecular weight distribution
 - (2) Scrutinize the reaction conditions for the preparation of high-quality bottlebrush-like block copolymers with uniformly grown side chains
 - (3) Craft a set of uniform metal oxide 1D nanorods (with a focus on NiFe_2O_4 (NFO) nanorods) via bottle-like block copolymer nanoreactor synthesized in (1)
 - (4) Explore the size- and shape-dependent properties of NFO nanorods, including their magnetic, photothermal, and electrocatalytic properties.
- Reversible Photo Crosslinkable 2D Organic-Inorganic Metal Halide Perovskite Nanoplates

- (1) Rationally design and synthesis coumarin derivatives as organic cation spacers for RP type 2D perovskite nanoplatelets
- (2) Synthesize and characterize coumarin containing 2D perovskite nanoplatelets
- (3) Study the reversible and photo controllable assembly induced property

Chapter 3. Ternary Biocidal-Photocatalytic-Upconverting Nanocomposites for Enhanced Antibacterial Activity Preliminary Results

3.1. Introduction

Antibacterial food packaging has emerged as an effective route to reducing foodborne diseases by preventing microbial contamination of foods via modifying the environment inside the packaging and interacting with the headspace or packed foods.¹⁰⁶ Nanotechnology has been widely applied in all areas of food science, including food processing, security, and packaging. In the latter context, metal and metal oxide nanoparticles (NPs),¹⁰⁷ carbon nanomaterials (e.g., graphene, carbon dots, and carbon tubes¹⁰⁸), and mesoporous particles¹⁰⁹ have garnered much attention for food packaging owing to their intrinsic biocidal properties. Among them, metallic Ag NPs and semiconducting metal oxide NPs (e.g., TiO₂, ZnO, and MgO NPs) are the most studied active antibacterial agents. Ag NPs are known to possess highly efficient antibacterial activity for Gram-positive and Gram-negative bacteria.⁸¹⁻⁸⁴ They inactivate bacteria via destroying cell membrane,⁸⁷ forming reactive oxygen species (ROS),⁸⁹ or interfering signal transduction.⁹³ Despite excellent antimicrobial performance, safety concerns over the potential nanotoxicity of Ag to human body greatly limit their commercialization.⁹⁴⁻⁹⁶ Notably, semiconducting NPs can also create ROS to terminate bacteria via photocatalytic reaction under irradiation (generally UV light). Unfortunately, the need for UV to trigger photocatalytic reaction represents a significant barrier towards practical application of this class of nanomaterials as UV photons are able to deteriorate food quality, particularly for meat products.^{97, 110} Nonetheless, the implementation of Ag and TiO₂ NPs together displayed improved antibacterial efficiency due to a series of synergic effects, including Ag reduces electron-hole recombination in TiO₂ under UV light by trapping photogenerated electrons which can then generate ROS,^{99, 100} and electron transfer from Ag NPs, as a result of their surface plasmonic resonance under visible light, to the conduction band of TiO₂ where ROS can be

generated.¹⁰¹⁻¹⁰³ Other techniques including antifouling surfaces^{111, 112} and natural extracts^{113, 114} have also shown their potential in antibacterial food packaging, yet face some issues associated with low efficiency, short life-time, and fragility.

Lanthanide-doped upconverting nanocrystals (UCNCs) are a class of nanomaterials that are capable of absorbing long-wavelength low-energy near infrared (NIR) photons and then emitting short-wavelength high-energy visible and UV via upconverting process.^{115, 116} They find applications in biomedical field,^{117, 118} optics,^{119, 120} security,¹²¹ and energy.^{122, 123} Yb³⁺ and Tm³⁺ co-doped NaYF₄ (i.e., β -phased NaYF₄@Yb:Tm) has been proven to be one of the most efficient NIR-to-UV upconverters.^{124, 125} When combined with suitable semiconductors of interest, such as TiO₂^{126, 127} and ZnO,^{128, 129} NaYF₄@Yb:Tm could activate the photocatalytic reaction of these semiconducting NPs under NIR lights, dispensing with the need for use of high-energy UV source. As such, the NaYF₄@Yb:Tm/semiconductor nanohybrids carry the potential to be employed as photocatalytic antibacterial nanomaterial under NIR irradiation, yet this has yet to be largely explored.¹³⁰

Herein, we report, *for the first time*, ternary multifunctional nanocomposites comprising biocidal Ag, photocatalytic TiO₂, and upconverting NaYF₄@Yb:Tm NPs for antibacterial application by capitalizing on the synergic effect among the three constituents. Interestingly, the ternary nanocomposites manifest superior antibacterial activity against *E. coli* under ambient light and solar simulator irradiation with UV photons filtered, outperforming Ag NPs as well as Ag/TiO₂ nanocomposites. The multifunctional Ag/TiO₂/NaYF₄@Yb:Tm nanocomposites are mixed with cellulose nanofibrils and processed into films to demonstrate their potential for antibacterial food packaging.

3.2. Experimental Section

3.2.1. Materials

Silver acetate (AgNO_3 , 99.9995%), ammonium hydrogen carbonate (NH_4HCO_3 , 98%), and oleic acid (OA, technical grade, 90%) were purchased from Alfa Aesar. Sodium trifluoroacetate (NaTFA , 98%), ytterbium (III) oxide (Yb_2O_3 , $\geq 99.99\%$), trisodium citrate dihydrate (99-100.5% anhydrous basis), rhodamine B ($\geq 95\%$) were purchased from Aldrich. Thulium(III) oxide (Tm_2O_3 , 99.9% trace metal basis) was purchased from BTC. Trifluoroacetic acid (TFA, $\geq 99.5\%$), acetonitrile ($\geq 99.8\%$), and anhydrous N,N-dimethylformamide (DMF, 99.8%) were purchased from Millipore Sigma. Oleylamine (OAm, $>50\%$), triethylamine ($\geq 99.0\%$), cyclohexane, ($>99.5\%$) and polyvinylpyrrolidone (PVP, MW=40,000) were purchased from TCI. Nitrosonium tetrafluoroborate (NOBF_4 , 97%) and titanium(IV) n-butoxide ($\text{Ti}(\text{OBu})_4$, 99%) were purchased from Acros Organics. 1,4-benzoquinone (99%) and ethylenediaminetetraacetic acid (99+%) were purchased from Thermo Scientific. TEMPO-oxidized cellulose nanofibril (CNF, 1.1 wt% CNF in water, 1.5 mmol $-\text{COONa}/\text{g}$ dry CNF) was purchased from University of Maine Process Development Center. Acetone ($\geq 99.5\%$), isopropyl alcohol ($\geq 99.5\%$), and hexane ($\geq 98.5\%$) were purchased from VWR Chemicals BDH. Ethanol (200 proof) was purchased from Koptec. *Escherichia coli* (*E. coli*, ATCC 10798) was obtained from the American Type Culture Collection (ATCC). Dehydrated Luria-Bertani (LB) broth and LB agar were purchased from BD Difco. The LB broth and agar plates were prepared following the manufacturer's instructions, in which all solutions were autoclaved at 121°C for 15 min for sterilization before use. All chemicals were used as received without any further purification. DI water ($18\text{ M}\Omega\text{ cm}$) from Direct Q system was used throughout the entire experiment, and all aqueous solutions were prepared with DI water.

3.2.2. Method

(a) Synthesis of water-dispersible Ag NPs : Water-dispersible Ag NPs were synthesized by a simple wet chemistry method modified from literature.¹³¹ 17 mg AgNO₃ was first dissolved in 50 ml DI water. The AgNO₃ solution was then brought to boiling under refluxing. 2 ml of 1% trisodium citrate aqueous solution was then rapidly injected into the solution under vigorous stirring. The solution was kept boiling for 30 min, during which the reaction solution gradually changed from colorless to yellow to yellow-grey. The Ag NPs were purified by centrifugation at 13,000 rpm for 10 min, washed with DI water for three times, and dispersed in DI water.

(b) Synthesis of water-dispersible TiO₂ NPs: Water-dispersible TiO₂ NPs were synthesized in two steps. TiO₂ NPs capped with hydrophobic oleic acid were first prepared by solvothermal method modified from previous report.¹³² In a typical reaction, NH₄HCO₃ (1 g), triethylamine (5 ml), cyclohexane (5 ml) and OA (23 ml) were mixed at room temperature by stirring. 1 ml of Ti(OBu)₄ was then added dropwise into the solution. After stirring for 5 min, the reaction solution was transferred into a Teflon-lined, stainless autoclave at 180 °C for 16 h. The TiO₂ NPs were purified by wash with ethanol three times and dispersed in hexane. A quick ligand exchange treatment was applied to convert non-polar solvent dispersed TiO₂ NPs into water-dispersible NPs.¹³³ The treatment involves two steps. First, TiO₂ NP hexane dispersion (~10 mg/ml) was combined with NOBF₄ acetonitrile solution (~10 mg/ml) to form a two-phase mixture (1:1 by volume), which was then stirred for about 5 min until NPs were transferred from the upper hexane layer to the bottom acetonitrile layer. The NOBF₄ ligand-covered NPs can be easily redispersed in DMF after washing with toluene and hexane (1:1 by volume). A secondary ligand exchange reaction was then conducted to transfer the NPs to the aqueous medium. About 100mg PVP was

added to 10 ml of DMF dispersion of TiO₂ NPs (~10 mg/ml), followed by vigorous stirring for 1 hr. The NPs were washed with acetone and redispersed in DI water.

(c) Synthesis of RE(TFA)₃ (RE=Y, Yb, and Tm): Approximately 1 g of RE₂O₃ was added to 10 ml of water and TFA (1:1 by volume) in a round bottom flask. The suspension was heated to 80 °C and stirred under refluxing until clear. The reaction solution was then allowed to cool to room temperature. The solvent was evaporated off using a rotary evaporator, leaving behind the RE(TFA)₃ powder.

(d) Synthesis of water-dispersible β -NaYF₄@Yb:Tm NPs: The two-step strategy was also used to prepare water-dispersible NaYF₄@Yb:Tm NPs (UCNPs). OAm-capped UCNPs were synthesized by a thermal decomposition approach.¹¹⁵ RE(TFA)₃ (1 mmol in total, 79.8% Y, 20% Yb, 0.2% Tm) and NaTFA (2 mmol) were added to 20 ml OAm into a three neck flask and heated to 110 °C under vacuum for 45 min to form a transparent yellowish solution. The reaction vessel was then filled with N₂ and heated to 325 °C using heating mantle in approximately 1 hr. The reaction was kept at 325 °C for 30 min and cooled down to room temperature. The UCNPs were purified by hexane and ethanol and redispersed in hexane. Same ligand exchange procedure as TiO₂ NPs was taken to transfer the UCNPs into aqueous media.

(e) Preparation of CNF-based antibacterial films: 2,2,6,6-tetramethylpiperidine-1-oxyl radical (TEMPO)-oxidized CNF water slurry (1.1 wt%) was diluted 50 times with DI water. Ag nanoparticles, TiO₂ nanoparticles, and UCNPs water dispersions were mixed to form a 1:1:1 (by weight of nanoparticles) mixture, which was then added to the diluted TEMPO-oxidized CNF water slurry at different weight fraction, followed by vigorous stirring. The mixture was poured into petri dishes and dried at 70°C overnight to yield the CNF-Ag/TiO₂/UCNP nanocomposite films.

(f) Evaluation of antibacterial performance: *E. coli* was used to study the antibacterial activity of the Ag/TiO₂/UCNP ternary nanocomposites with different compositions under various environmental conditions. The *E. coli* was cultured in the LB broth to log phase (35 °C overnight) and harvested by centrifugation at 4000 rpm. After washing with DI water three times, the *E. coli* suspension was dispersed and diluted in DI water to the desired concentration of $\sim 10^7$ CFU ml⁻¹. 1 ml of nanocomposite water dispersions with different composition and concentration were added into 9 ml of *E. coli* suspension and well mixed. Each sample was placed at room temperature under various conditions (i.e., dark, ambient light, and solar irradiation generated by solar simulator with UV portion blocked by a UV filter) for 30 min. The *E. coli*-nanocomposite suspensions were then diluted 10 to 10⁵ times. 100 μ L of each suspension were then spread on LB agar petri dishes and incubated on the petri dish at 35 °C in dark for 24 h.

The antibacterial property of the CNF-Ag/TiO₂/UCNP nanocomposite films was examined based on a disk diffusion method. The *E. coli* water suspension with a concentration of approximately 10⁹ CFU ml⁻¹ prepared in the way described above were transferred and spread onto the LB agar. The test film samples were placed on the *E. coli* agar plates, kept under different conditions for 30 min, and incubated at 35 °C for 24 h in dark.

3.2.3. Characterizations

The morphologies of as-synthesized Ag, TiO₂, UCNPs and ligand-exchanged TiO₂ NPs and UCNPs were obtained using a JEOL 100CX-II transmission electron microscope operated at 100kV. TEM samples were prepared by depositing NP hexane or water dispersion on a carbon film-supported copper grid. X-ray diffraction (XRD) data were recorded by a Panalytical XPert

PRO Alpha-1 diffractometer using Cu-K α radiation (1.54 Å, at 45 kV and 40mA) with a step of 0.08° per 16 s. The UV-vis spectra of Ag and TiO₂ NPs and RhB photocatalytic degradation were obtained with a Shimadzu UV-2600 spectrometer. The upconversion spectra of UCNPs were acquired with a homemade system. 980 nm laser was generated using an MDL-III diode laser (2W). Upconversion photoluminescence emission spectra were recorded with an Ocean Optics USB4000 spectrophotometer with detection range from 200 nm to 1100 nm under the excitation of the 980 nm laser. A Newport AM 1.5G solar simulator (100mW cm⁻²) applied with a UV(C) filter (Hoya) was used to generate sun light for the antibacterial tests. Temperature of testing samples was measured with a FLIR ONE Pro thermal imaging camera. The mechanical property of CNF based films was achieved using a TA Q800 dynamic mechanical analyzer (DMA).

3.3. Results and Discussion

Water-dispersible NPs were synthesized either directly in an aqueous medium using citrate as hydrophilic ligand or in a non-polar medium, followed by ligand exchange to replace hydrophobic OA and OAm with hydrophilic PVP. The morphologies of water-dispersible NPs were examined by TEM (**Figure 3.1 a-c**). No obvious aggregation was observed in ligand-exchanged TiO₂ and UCNPs, suggesting the successful anchoring of PVP on the NP surface. **Figure 3.2 a and b** show TEM images of as synthesized TiO₂ and UCNP. XRD analysis confirmed the crystal structures of Ag, TiO₂ and UCNPs. A typical absorption peak at 426 nm in the UV-vis spectrum was seen in the as-synthesized Ag NP water suspension, further verifying the formation of Ag NPs (**Figure 3.1d**). XRD patterns of the three nanoparticles are shown in **Figure 3.1e**. The peaks at 38.1°, 44.3°, 64.5°, and 77.4° can be indexed to the (111), (200), (220), and (311) planes of a face-centered cubic (FCC) Ag crystal. The peaks at 25.3°, 37.6°, 48.1°, 54.0°, and 62.7° can be assigned to the (101), (004), (200), (105), and (204) planes of an anatase phased TiO₂ crystal. The XRD pattern

of the UCNPs displayed in **Figure 3.1e** shows that they possess the reflection of a $P6_3/m$ space group, substantiating the formation of β - NaYF_4 host. It is worth noting that the β - NaYF_4 @Yb:Tm is critically important in this study as it is the optimal host lattice for upconverting due to its suitable interatomic distance, low phonon threshold, and lack of energy states for non-radiative cross-relaxation, compared to α - NaYF_4 , another common phase of NaYF_4 .^{134, 135}

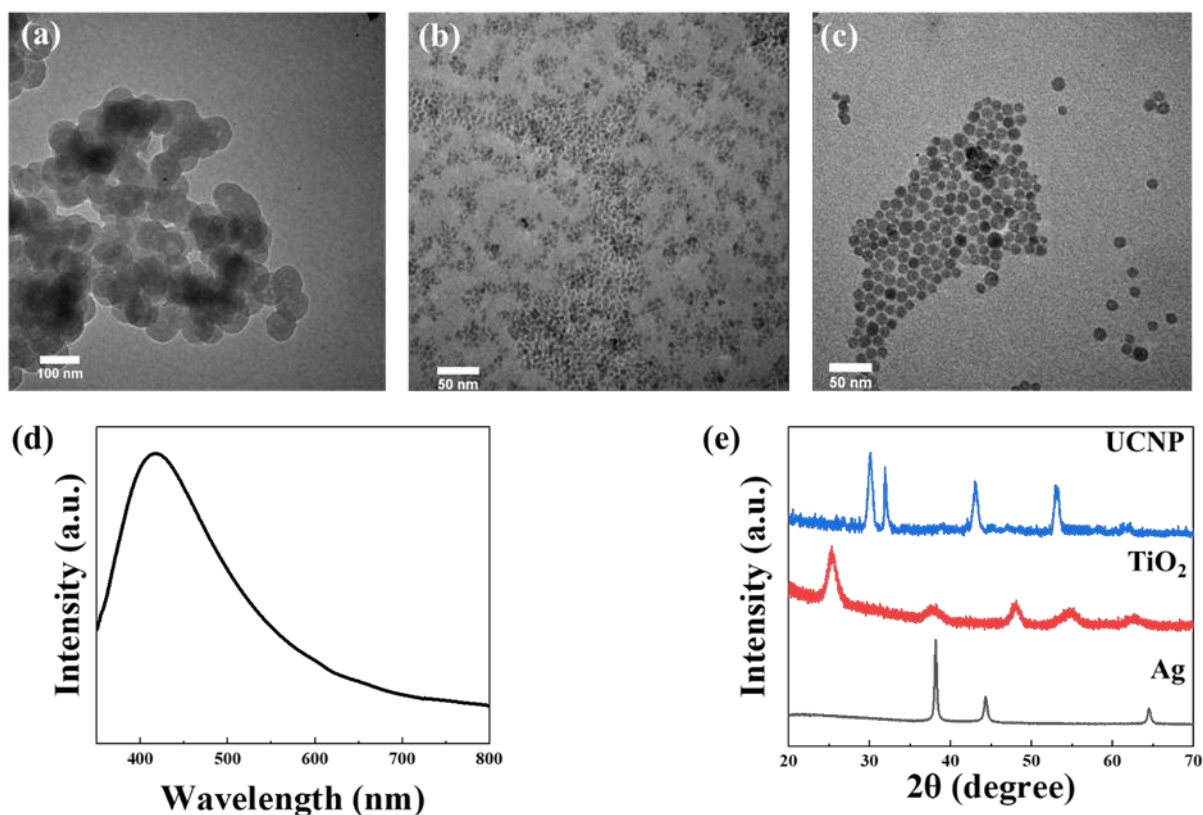


Figure 3.1. (a-c) TEM images of (a) Au NPs, (b) TiO_2 NPs, and (c) UCNPs dispersed in water. (d) UV-vis absorption spectrum of Ag NPs. (e) XRD profiles of Ag, TiO_2 , and UCNPs.

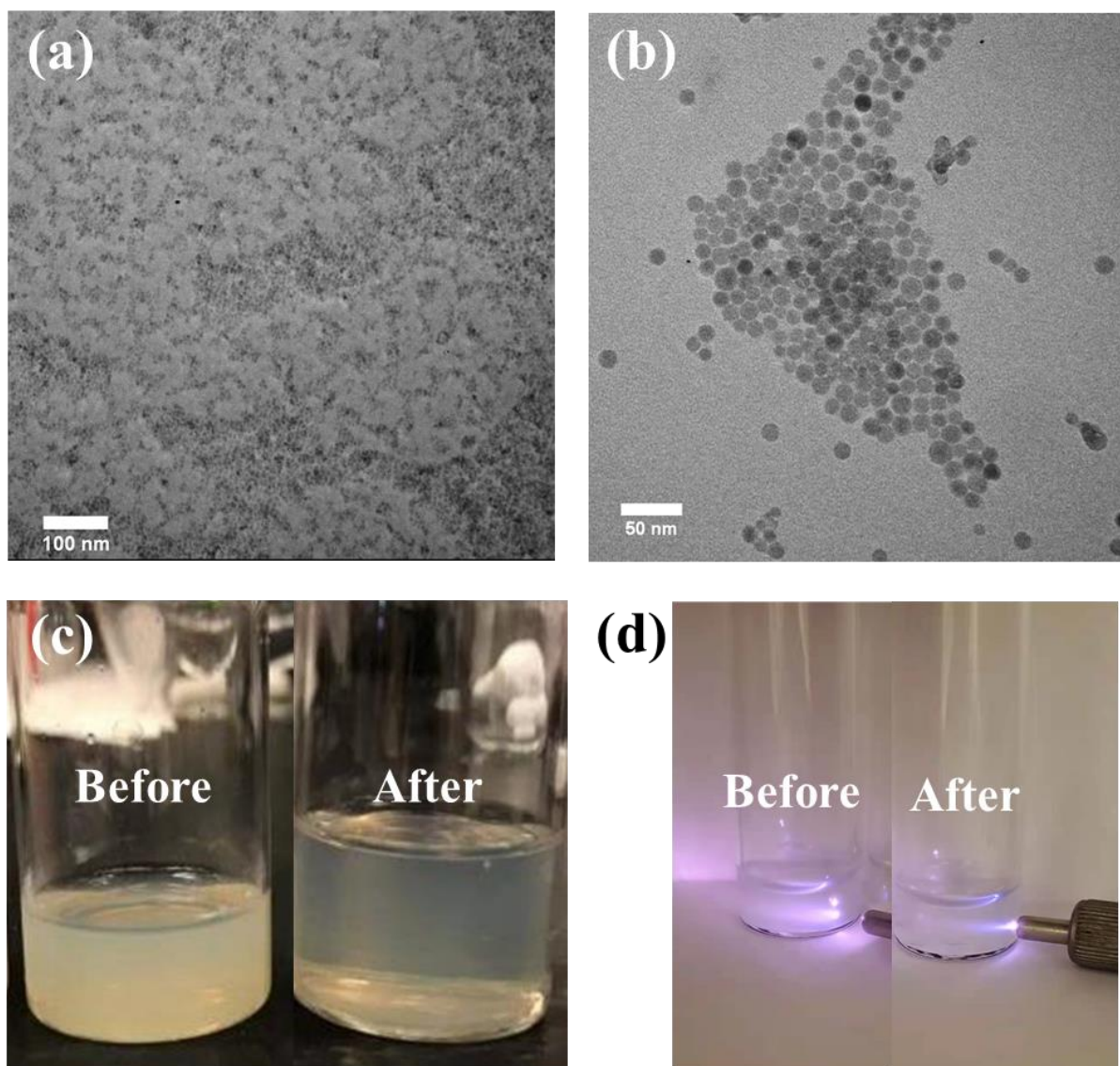


Figure 3.2. TEM images of synthesized (a) TiO_2 NPs, and (b) UCNPs dispersed in hexane. Digital image of (c) TiO_2 NPs and (d) UCNPs solutions before and after ligand exchange.

The ligand exchange process was then implemented to transfer TiO_2 and UCNPs from organic solvent to aqueous media to afford the miscibility in hydrophilic TEMPO-oxidized CNF and form the film with CNF as the matrix. UV-vis spectra were taken for TiO_2 NPs before and after ligand

exchange and showed no obvious change in the optical properties of TiO₂ NPs (**Figure 3.3a**). Upconversion spectra of the UCNPs before and after ligand exchange under the excitation of a 980-nm diode laser were obtained by using a house-made upconversion spectroscopy. Two emissions in the UV region (346 and 362 nm) and two emissions in the visible region (450 and 477 nm) are clearly evident (**Figure 3.3b**). Emissions from low to high wavelength corresponding to the transition of $^1\text{I}_6 \rightarrow ^3\text{F}_4$, $^1\text{D}_2 \rightarrow ^3\text{H}_6$, $^1\text{D}_2 \rightarrow ^3\text{F}_4$, $^1\text{G}_4 \rightarrow ^3\text{H}_6$ in Tm^{3+} ions, respectively.^{136, 137} These upconverted emissions are achieved in a process, in which two or more photons of 980 nm light are absorbed by sensitizer Yb^{3+} , the energy is then transferred to the neighboring activator Tm^{3+} ions, and finally the Tm^{3+} ions relax radiatively to the ground state. The upconversion emission intensity of PVP-covered UCNPs are slightly stronger than original OAm-capped UCNPs. This is due to the improved protection of the NP surface as well as the higher refractive index of PVP than OAm, which leads to less reflective loss of the emitted light.^{138, 139} Digital images of TiO₂ and UCNP solutions before (in hexane) and after (in water) ligand change further confirm the effective replacement of hydrophobic ligands by PVP. (**Figure 3.2 c and d**)

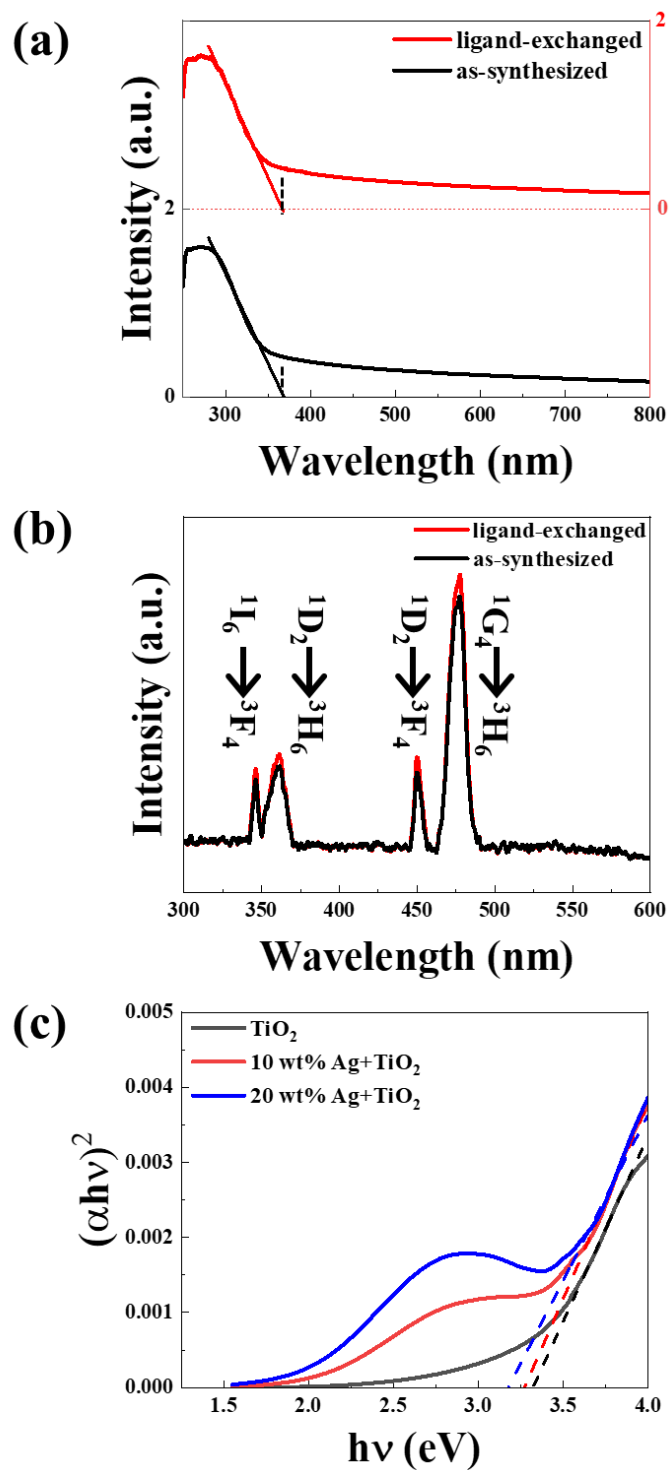


Figure 3.3. (a) UV-vis absorption spectra of TiO_2 NPs before and after ligand exchange. (b) Upconversion spectra of UCNPs before and after ligand exchange. (c) Tauc plot obtained from UV-vis absorption spectra of TiO_2 NPs and Ag/ TiO_2 nanocomposites in water.

The synergistic effect of Ag/TiO₂ nanocomposite is shown by the Tauc plot obtained from UV-vis absorption spectra in **Figure 3.3c**. Compared to pure TiO₂, the bandgap of Ag/TiO₂ is smaller. According to the previous studies, the narrowed bandgap can be attributed to a two-fold mechanism: (1) the photoexcited electrons generated from the plasmon resonance of Ag under visible light illumination are transferred to the conduction band of TiO₂,¹⁴⁰ and (2) the interaction between Ag and TiO₂ results in a higher ratio of Ti(III) oxide on the surface of TiO₂, which is proven to be a narrow bandgap semiconductor whose energy levels are between the valence and conduction band of TiO₂.^{141, 142} Such synergy has been shown to cause increased photocatalytic and antibacterial properties of the Ag/TiO₂ composite.^{101, 143}

The antibacterial performance of the as-prepared nanocomposites (i.e. ternary Ag/TiO₂/UCNP) was tested using the colony counting method. Two control samples, that is, Ag NPs only and binary Ag/TiO₂ NPs nanocomposites, were also prepared and used for comparison. 1 ml of nanocomposites water suspension (1 mg/ml for each active species) was mixed with *E. coli* water suspension (9 ml, 10⁷ CFU/ml) and treated under dark, ambient light, and vis-IR light generated from solar simulator (yet with UV photons filtered; see *Method Section*) at room temperature for 30 min. It is worth noting that *E. coli* could be killed at high temperature (> 70 °C).¹⁴⁴ Therefore, the temperature of all samples was monitored with an IR temperature camera and found to be not exceeding 35 °C (**Figure 3.4.**), signifying that the relatively strong illumination from the solar simulator would not kill the bacteria thermally.

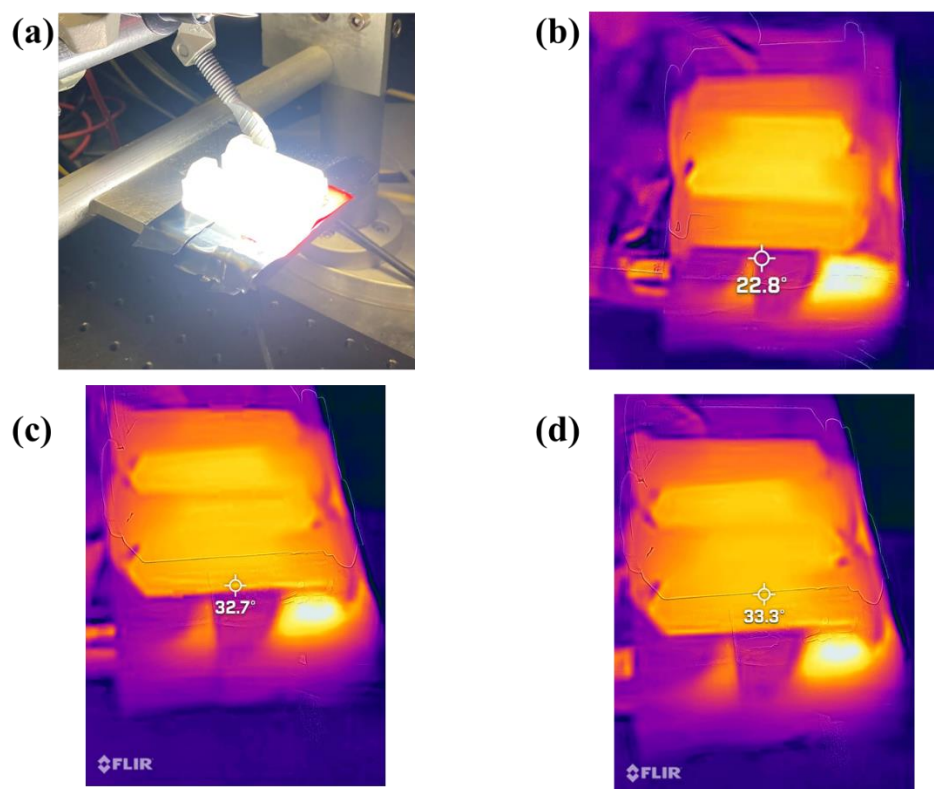


Fig 3.4. (a) Digital image of test sample under solar simulator; IR image showing temperature of samples under irradiation for (b) 0 min, (c) 15 min, and (d) 30 min.

As noted above, a UV filter was applied on the solar simulator as otherwise the UV portion from the simulated sun light is strong enough to terminate all the *E. coli* without any antibacterial agents added (**Table 3.1**). The *E. coli*-nanocomposite mixtures were then diluted to different extent and directly plated on LB agar disk. The number of residual *E. coli* colonies after 24 h incubation at 35 °C in dark was counted. From **Figure 3.5**, it is clear that the number of residual *E. coli* in all three samples (Ag NPs only, binary Ag/TiO₂ nanocomposites, and ternary Ag/TiO₂/UCNP nanocomposites) under dark were comparable with the slight decrease in the two nanocomposites samples (Ag/TiO₂ and Ag/TiO₂/UCNP). This result suggests no synergistic effect from any

nanocomposites when no light exposure. Upon the irradiation with ambient light, obvious enhancement in the bactericidal performance in Ag/TiO₂ was achieved due to the synergy from the two constituents, in consistence with previous studies.^{99, 145, 146} A further improvement was seen for Ag/TiO₂/UCNP nanocomposites, signifying the effectiveness of introducing UCNP under ambient environment. The improvement was more significant when stronger illumination generated from solar simulator (1 sun) equipped with a UV filter was shined on the samples. The results for Ag and Ag/TiO₂ samples were moderately improved after switching the light source. In sharp contrast, the percentage of bacteria reduction in the Ag/TiO₂/UCNP nanocomposites sample was greatly increased. The much stronger NIR portion of the irradiation from solar simulator excited the β -NaYF₄@Yb:Tm UCNP to emit more UV and visible photons,¹⁴⁷⁻¹⁴⁹ thereby boosting the photocatalytic reactivity of the Ag/TiO₂ and in turn markedly enhanced antibacterial efficiency.

Table 3.1. Comparison of *E. coli* reduction percentage with and without UV filter

Test condition	Solar simulator without UV filter				Dark	Solar simulator with UV filter
	No NPs	Ag	Ag+TiO ₂	Ag+TiO ₂ +UCNP	No NPs	No NPs
Reduction(%)	100	100	100	100	0	7.2±0.4

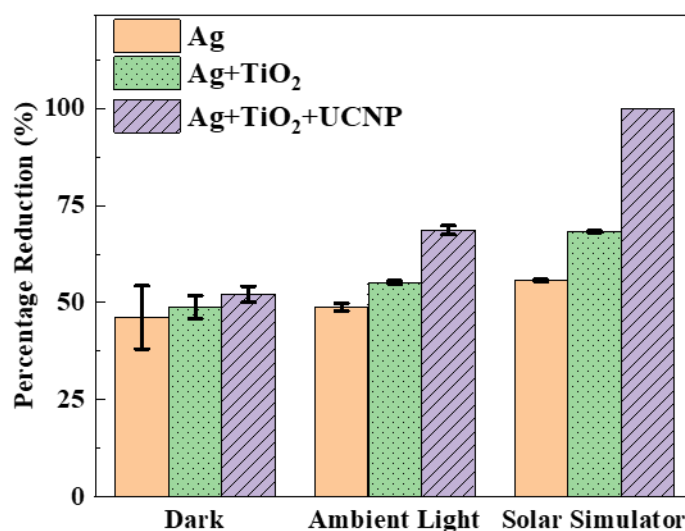


Figure 3.5. Comparison of antibacterial performance of Ag NPs, Ag/TiO₂ NPs nanocomposites, and Ag/TiO₂/UCNP NPs nanocomposite against *E. coli* in dark, under ambient light, and under solar simulator equipped with a UV filter (i.e., removal of UV photons).

Clearly, introducing UCNP to Ag/TiO₂ NPs nanocomposites can effectively strengthen the ability of the nanocomposite to terminate *E. coli*. The concentration of the three constituents in the ternary nanocomposite was then varied to further investigate the influence of β -NaYF₄@Yb:Tm UCNP in the biocidal event. To this end, solar simulator with a UV filter was used as light source for all the tests. It is notable that the concentration of each constituent NPs was controlled at a low level because we found that the *E. coli* were killed completely when the concentration was too high, and the results became indistinguishable. Thus, the concentration of Ag NPs in each sample was 0.2 mg/ml in the test. The concentrations of TiO₂ and β -NaYF₄@Yb:Tm UCNP were maintained the same and increased from 0.2 to 1 and 2 mg/ml (designated as Groups 1-3, respectively; **Figure 3.6**). Meanwhile, TiO₂ NPs concentration was kept at 0.2 mg/ml yet UCNP contents were increased to 1 and 2 mg/ml (designated as Groups 4 and 5, respectively; **Figure 3.6**). A clear trend can be seen that higher concentration of TiO₂ and UCNP renders a better

performance (**Figure 3.6.**). Moreover, solely increasing the amount of UCNP also improves the biocidal efficiency, corroborating that the upconverted emissions from the UCNPs can effectively activate Ag and TiO₂ NPs. The mechanism of the greatly-enhanced antibacterial efficiency in the ternary nanocomposites is illustrated in **Figure 3.7.** As shown in the energy level of Yb³⁺ and Tm³⁺ in UCNP, the ¹I₆→³F₄ and ¹D₂→³H₆ transitions in Tm³⁺ produce 350 nm and 365 nm UV emissions, which are capable of exciting TiO₂ and generating electron-hole pairs. The photogenerated holes can react with the surrounding water to produce •OH and the photogenerated electrons could reduce O₂ to yield •O₂⁻; these two types of ROS are able to damage cell membrane and lead to the death of bacteria.^{105, 150} In the meantime, visible emissions from UCNPs (450 and 470 nm) can be absorbed by Ag NPs via plasmonic resonance ($\lambda = 426$ nm; **Figure 3.1d**) and the photogenerated electrons can easily transfer from the noble metal (Ag) to the conduction band of the semiconductor (TiO₂) and reduce the O₂ to form •O₂⁻ radicals. The •O₂⁻ can then react with water and transform to •OH radicals, which been proven to be one of the most active antibacterial ROS.¹³⁰

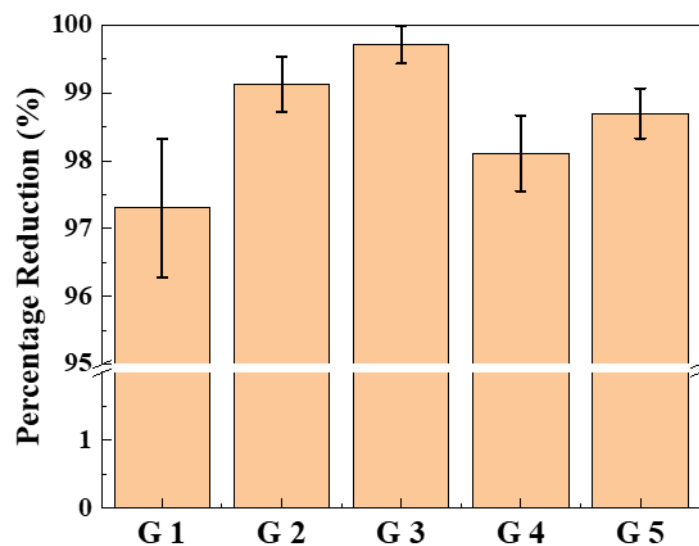


Figure 3.6. Comparison of antibacterial performance of ternary nanocomposite systems with different compositions against *E. coli*.

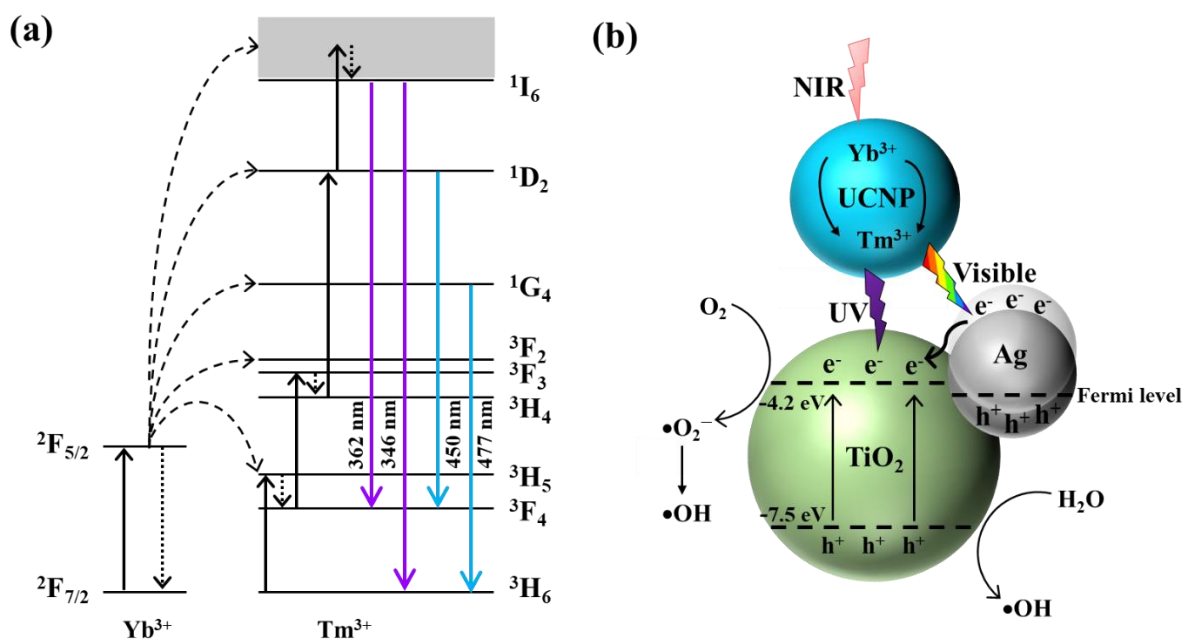


Figure 3.7. (a) Energy level diagram of NaYF₄@Yb:Tm NPs. (b) Antibacterial mechanism of the ternary Ag/TiO₂/β-NaYF₄@Yb:Tm UCNP nanocomposite system.

Photocatalytic degradation of rhodamine B (RhB) was conducted to further evaluate the active species generated from the ternary nanocomposites and understand the antibacterial mechanism of the system.^{145, 151} A trapping experiment was carried out by adding different scavengers in the RhB aqueous solution. Specifically, ethylenediaminetetraacetic acid (EDTA), isopropyl alcohol (IPA), and 1,4-benzoquinone (BQ) was individually dissolved in RhB solution to quench h^+ , $\bullet OH$, and $\bullet O_2^-$, respectively^{115, 152} and the concentration of the scavengers were fixed at 2 mM. The scavengers dissolved RhB solutions were then mixed with the ternary nanocomposite aqueous solution (10 mg/ml of each species) via vigorous stirring and placed under a solar simulator with a UV filter. All reaction conditions were the same except for the type of scavengers in the solutions. Samples were taken during the light exposure at 0 min, 15 min, 30 min, 45 min to monitor the degradation of RhB.¹⁵³ **Figure 3.8 a** depicts the change in the absorption intensity of the peak at $\lambda = 550$ nm, reflecting the degradation of RhB when no trapping scavenger was present. When EDTA and BQ were added into the solution, the photocatalytic degradation was slightly reduced (**Figure 3.8 b** and **Figure 3.9**), signifying that h^+ and $\bullet O_2^-$ were generated from the nanocomposites under visible and IR irradiation. Moreover, a significant reduction in the photodegradation of RhB was seen when IPA was added (**Figure 3.8 b** and **Figure 3.9**). These results suggest that $\bullet OH$ is a predominant active species originated from the ternary nanocomposites, while $\bullet O_2^-$ and h^+ were also produced yet with a much smaller amount, correlating well with the antibacterial mechanism discussed above.

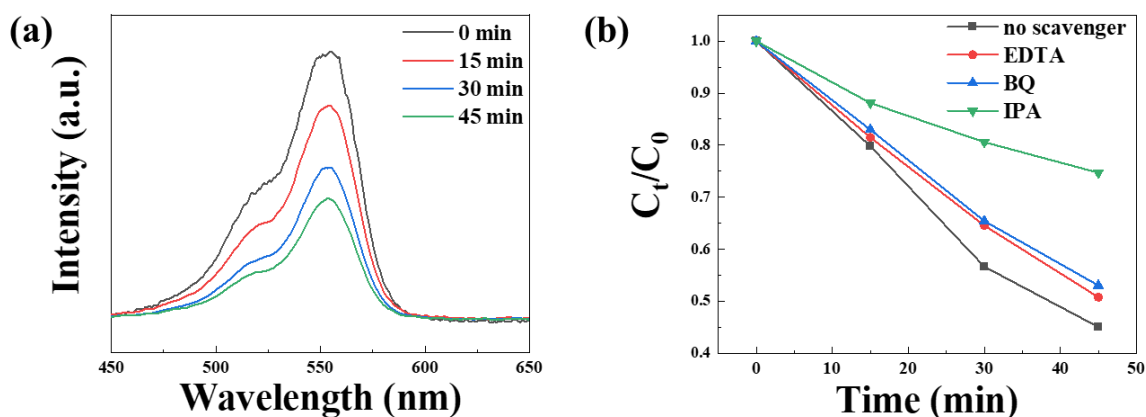


Figure 3.8. (a) Absorption spectra depicting photodegradation of RhB by the ternary nanocomposites aqueous solution in the absence of trapping scavenger under solar simulator with a UV filter. (b) Photodegradation of RhB as a function of time with no trapping scavenger, EDTA, BQ, and IPA, respectively.

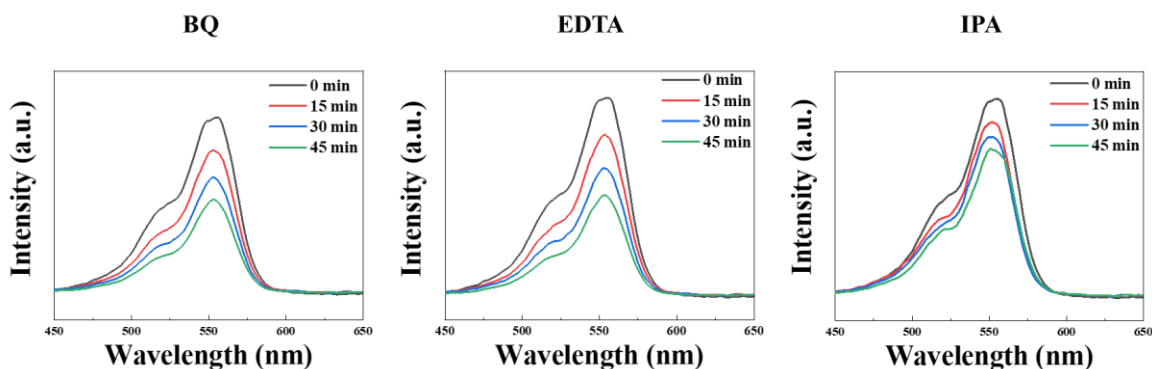


Figure 3.9. Change in UV-Vis absorption spectra of RhB in the ternary nanocomposites solution in the presence of BQ, EDTA, and IPA.

To further demonstrate the potential application of the ternary antibacterial nanocomposites in active biocidal food packaging, the nanocomposites were mixed with TEMPO-oxidized

cellulose nanofibrils (CNF) to form a biodegradable film. Four nanocomposite films composed of TEMPO-oxidized CNF and Ag/TiO₂/UCNP with the weight percentages of ternary Ag/TiO₂/UCNP nanocomposites (1:1:1 weight ratio of the three constituents) at 0%, 1%, 5%, and 10% were prepared (denoted Film-1 to Film-4, respectively). The thickness of the four films were approximately the same, that is, 20±1.2 μm, 19±1.0 μm, 22±2.2 μm, and 25±2.0 μm, respectively. The data was acquired by measuring the thickness at five different positions for each film. The tensile strength of the films measured by DMA and the resulting stress-strain curve is shown in **Figure 3.10 a**. The mechanical property of the film was obviously improved from approximately 6.8 MPa in Film 1 to 15.5 MPa in Film 4 (representing a 125 % increase). The higher tensile strength is a direct consequence of the addition of inorganic NPs into the film, which is commonly seen in inorganic NPs-reinforced polymer films. The films were cut into small discs with a diameter of ~7 mm for the disc diffusion test. The film-attached test agar plates were kept in dark, under ambient, and solar simulator generated light (with a UV filter) at room temperature for 30 min prior to being incubated at 35 °C in dark for 24 h. **Figure 3.10 b-d** compares the results of the disc diffusion tests. Clearly, the inhibition area for each film became larger when the light intensity shined on the film increased. The inhibition area also increased with the increase in the content of antibacterial active species, while no inhibition area can be detected by naked eyes for pure CNF films under all the test conditions, indicating the antibacterial property was attributed to the ternary Ag/TiO₂/UCNP nanocomposites. We note that the inhibition areas are relatively small compared to the reported studies in literature, which is likely due to the larger distance between UCNP and Ag (and TiO₂) NPs in the films, thus reducing their visible (for Ag) and UV (for TiO₂) absorption from β-NaYF₄@Yb:Tm UCNP. Future work will be focused on engineering the ternary

nanocomposite by crosslinking NPs or exploiting core/shell NPs to improve the utilization efficiency of the emissions from UCNPs.

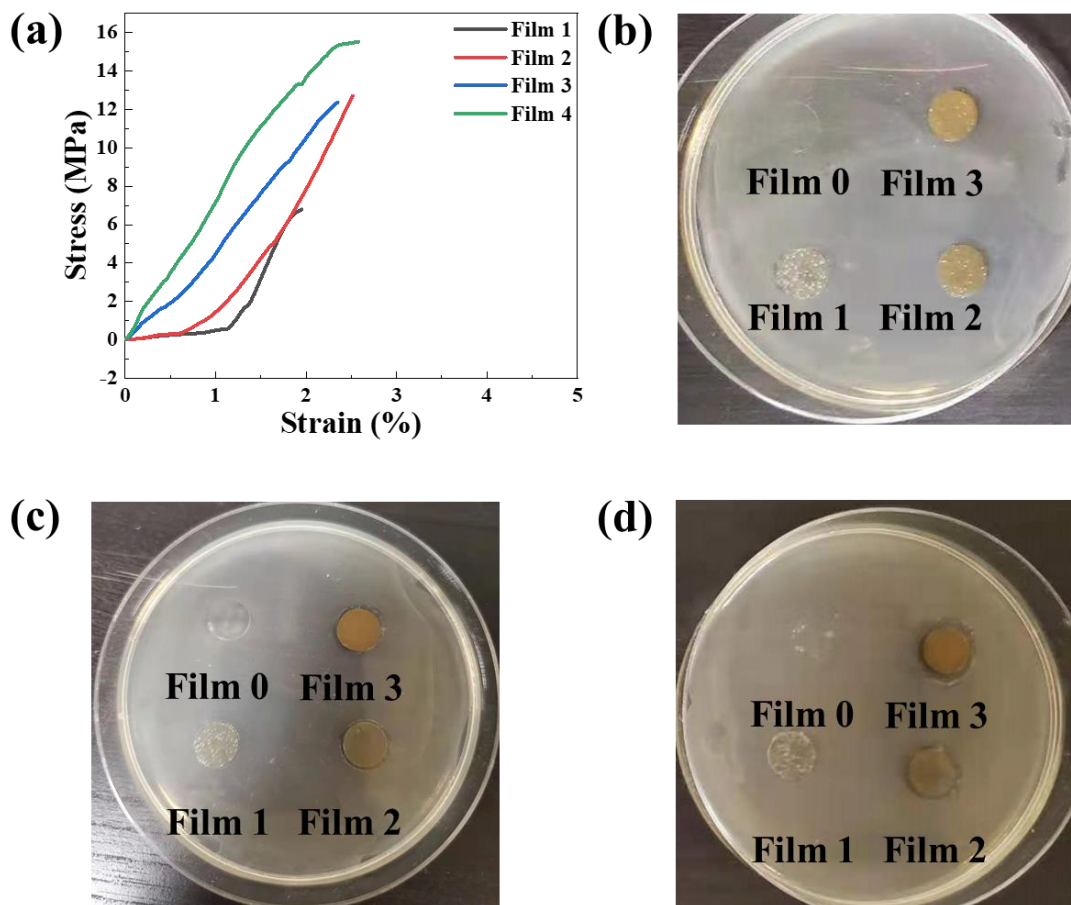


Figure 3.10. (a) Stress-strain curves of TEMPO-oxidized CNF-based nanocomposite films with 0 wt%, 1wt%, 5wt%, and 10wt% of the ternary Ag/TiO₂/UCNP nanocomposites. (b-d) Digital images of disc diffusion antibacterial tests of the CNF/Ag/TiO₂/UCNP nanocomposite films (b) in dark, (c) under ambient light, and (d) solar simulator with UV filter.

3.4. Conclusion

In summary, we developed a viable strategy to enhance antibacterial activity of nanomaterials by engineering ternary multifunctional nanocomposites composed of metallic Ag NPs, semiconducting TiO₂ NPs, and upconverting NaYF₄@Yb:Tm UCNPs. The rational introduction

of UCNPs markedly improves the biocidal efficiency of Ag/TiO₂ as NaYF₄@Yb:Tm UCNPs effectively convert NIR photons into visible and UV photons that are absorbed by Ag and TiO₂, respectively, to generate antibacterial ROS. Notably, the as-prepared nanocomposites display excellent bactericidal properties in water under 1 sun irradiation (with UV photons filtered) and good performance under moderate ambient light. The water-dispersible nanocomposites can be readily integrated with hydrophilic biopolymers such as TEMPO-oxidized CNF for film processing and showcase their potential for use as antibacterial packaging materials. This study highlights the possibility of not only reducing the use of potentially toxic Ag NPs, but also exerting efficient antibacterial activity in the absence of UV source, thereby avoiding the UV-induced deterioration of food quality.

Chapter 4. Nanoparticles via Star-like Block Copolymer as Nanoreactor and Their Applications in Electrocatalysis

4.1. Introduction

As discussed above, star-like block copolymers are stable unimolecular micelles with linear arms covalently connected to a central core, rendering supreme structural stability against various environmental perturbations. Using of star-like BCPs as nanoreactors to direct the synthesis of polymer-ligated NCs has garnered considerable interest due to the following appealing features. First, size and architecture of NPs can be delicately controlled because they are defined by the coordination blocks in the star-like BCP, which are synthesized by controlled/living radical polymerizations and possess well-defined MWs and low PDI. Therefore, plain, hollow, and core/shell NPs with precisely tailored dimensions (i.e., diameter of plain NPs, diameter of hollow interior and shell thickness of hollow NPs, and the core diameter and shell thickness of core/shell NPs) can be crafted. In addition, NPs with different chemical compositions can be readily produced by simply selecting proper inorganic precursors thanks to the robustness of the nanoreactor strategy. Moreover, surface chemistry, which is determined by the outer blocks of star-like BCP functioning as surface ligands can be easily tuned to yield polymer-ligated NPs with intriguing polarity, conductivity, stimuli responsivity, etc., endowed by the functional outer blocks. Also, the outer blocks are intimately and permanently capped on the NP surfaces as these polymer chains are covalently connected to the inner and intermediate blocks of star-like BCP, thereby effectively preventing the aggregation of NPs and facilitating their dispersion in both solvents (liquid state) and polymer nanocomposites (solid state). Finally, star-like triblock copolymer nanoreactor strategy could be capitalized on to generate a variety of core/shell NPs of interest with even large lattice mismatch between the core and shell materials because the growth of nanocrystals is not interface dependent like conventional colloidal synthesis, which are otherwise

challenging to be achieved by conventional methods. In this chapter, a set of star-like lock copolymers were synthesized and used as nanoreactors for the synthesis of several distinct types of plain nanoparticles, e.g., metallic, transition metal oxide, and perovskite nanoparticles. Furthermore, CoFe_2O_4 nanoparticles were studied in detail for their magnetic field assisted OER catalytic studies.

Recently, the use of externally applied magnetic fields enhance OER electrocatalytic performance has gained significant attention. It has been reported that kinetics of OER exhibits strong dependence on the spin of catalyst surfaces, especially the step where triplet O_2 is generated from singlet reactants (OH^- and H_2O). It is because the spins in the ground state of reactants are in singlet state and paired while the production of O_2 with a singlet state requires more energy than producing a triplet O_2 .^{154, 155} In this regards, magnetization has been reported to be able to reduce this kinetic barrier by aligning the spin ordering of ferromagnetic (FM) electrocatalysts.¹⁵⁶ However, some of the most active OER catalysts, such as transition metal oxyhydroxides, are paramagnetic (PM), which lose their spin order after the removal of magnetic field.^{157, 158} In this context, a spin pinning effect in FM/PM core/shell materials could be utilized to maintain the spin ordering in high OER efficient yet paramagnetic surfaces, which has already been successfully demonstrated in a bulk CFO/ CoFeO_xH_y system,¹⁵⁹ but has yet to be explored in nanoscale.

In this work, the star-like diblock copolymer nanoreactors are utilized to produce a set of CFO/ CoFeO_xH_y core-shell nanoparticles via forming CFO NPs first and then performing controlled surface reconstruction. The effects of nanoparticle size and core-to-shell ratio on the magnetic field assisted OER enhancement was conducted.

4.2. Experimental Section

4.2.1. Materials

Toluene (99.5%), dichloromethane (>99.5%), α -bromoisobutyryl bromide (BiBB, 98%), anisole (99%), 2-butanone (99.0%), anhydrous dimethylformamide (DMF, >99.8%) anhydrous 1-methyl-2-pyrrolidinone (NMP, 99.5%), N,N,N',N',N''-pentamethyldiethylene triamine (PMDETA, 99%), trifluoroacetic acid (TFA, 99.9%), diethyl ether (anhydrous, 99.0%), ethanol (anhydrous, 99.5%), calcium hydride (CaH₂, for synthesis,) sodium bicarbonate (NaHCO₃, 99.7%), aluminum oxide powder (activated, neutral, ~325 mesh), tetrahydrofuran (THF, 99.0%), acetone (99.5%), magnesium sulfate (MgSO₄, anhydrous, 99.5%), benzyl alcohol (BA, anhydrous, 99.8%), diphenyl ether (DPE, 99%), deuterated chloroform (CDCl₃, 99.96%), deuterated dimethylformamide (DMF-d₇, 99.5%), lithium bromide (LiBr, 99%), acetic acid (99.7%) were purchased from Sigma-Aldrich and used as received.

β -cyclodextrin (β -CD, >97.0%, Sigma-Aldrich) were dried under vacuum for 48 hours at 60°C and azeotropic distilled in toluene for 2 hours at 120°C prior to the esterification reaction. Copper (I) bromide (CuBr, 98%, Sigma-Aldrich) was stirred for 2 hours in acetic acid, filtered, washed with ethanol and diethyl ether, and dried in vacuum at room temperature overnight. Styrene (St, 99.9%, Sigma-Aldrich), tert-butyl acrylate (tBA, 98%, Sigma-Aldrich) were distilled over CaH₂ under reduced pressure prior to use.

4.2.2. Methods

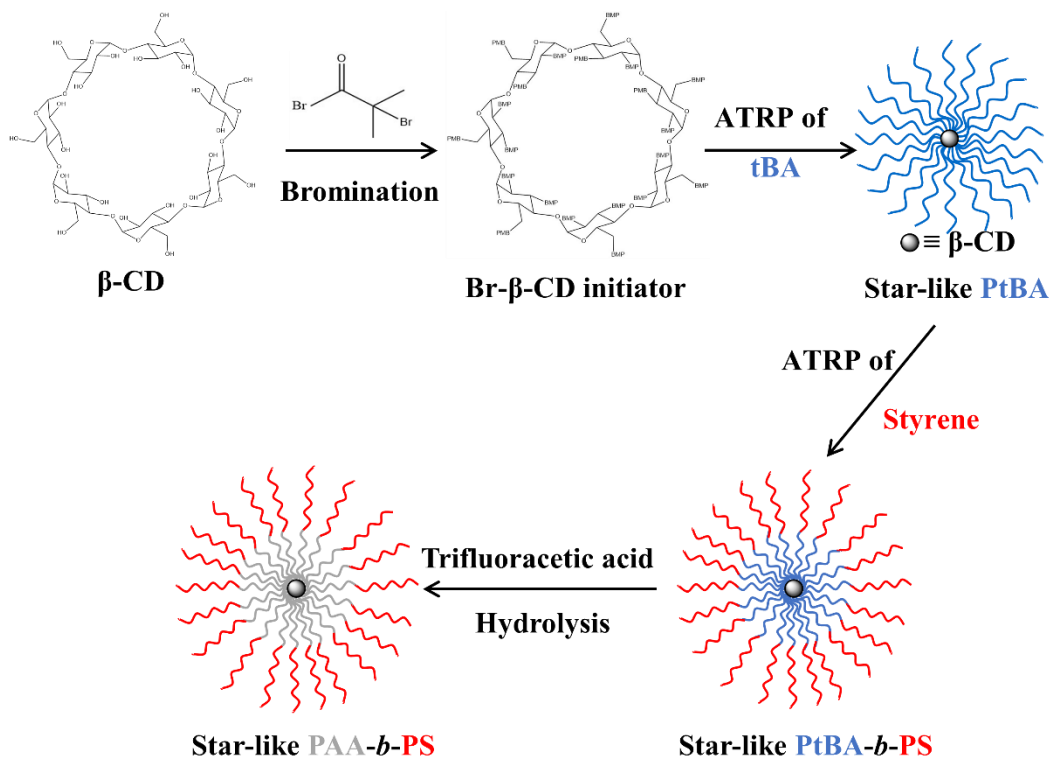


Figure 4.1. Schematic illustration of the synthesis of star-like nonlinear block copolymer (i.e., star-like PAA-*b*-PS) nanoreactor.

Figure 4.1. shows the synthetic route of the star-like PAA-*b*-PS nanoreactor. The detailed synthetic procedure is summarized as following:

(1) Synthesis of brominated β-CD initiator (Br-β-CD): β-CD was first dissolved in anhydrous 1-methyl-2-pyrrolidone (NMP) and then cooled to 0 °C in ice bath. 2-bromoisobutyl bromide (BiBB) was added into the solution dropwise under vigorous stirring in one hour. The reaction was let stirring for 1 hour at 0 °C and brought to room temperature and kept stirring for 223 hours. The crude solution was diluted with dichloromethane (DCM) and washed with saturated NaHCO₃ aqueous solution and DI water for several times. After washing, the product

was collected via removing DCM by rotary evaporator and dried in vacuum oven overnight at room temperature.

(2) Synthesis of poly(*tert*-butyl acrylate) (PtBA) star-like nonlinear polymer: Br- β -CD (macroinitiator), CuBr (catalyst), N,N,N',N'',N''-pentamethyldiethylenetriamine (PMDETA) (ligand), *tert*-butyl (*t*BA) (monomer) and methyl ethyl ketone (MEK) (solvent) were mixed in an ampoule and degassed by N₂ bubbling for 1 hour. Afterwards, the ampoule was sealed and put into an oil bath at 60 °C. The ampoule was taken out from the oil bath and dipped into ice bath and open to atmosphere at different desired time to terminate the polymerization. The crude solution was diluted with acetone, passed through neutral alumina column to remove the catalyst, and precipitated in a water/methanol mixture (v:v=1:1). After filtration, the product was dried in vacuum oven at room temperature.

(3) Synthesis of poly(*tert*-butyl acrylate)-*block*-polystyrene (PtBA-*b*-PS) star-like nonlinear polymer: PtBA star-like nonlinear polymer, CuBr, PMDETA, styrene and anisole were mixed in an ampoule and degassed by N₂ bubbling for 1 hour. Afterwards, the ampoule was sealed and put into an oil bath at 90 °C. The ampoule was taken out from the oil bath and dipped into ice bath and open to atmosphere at different desired time to terminate the polymerization. The crude solution was diluted with tetrahydrofuran (THF), passed through neutral alumina column to remove the catalyst, and precipitated in a water/methanol mixture (v:v=1:1). After filtration, the product was dried in vacuum oven at room temperature.

(4) Synthesis of poly(acrylic acid)-*block*-polystyrene (PAA-*b*-PS) star-like nonlinear polymer: PtBA-*b*-PS star-like nonlinear block copolymer was first dissolve in DCM into which trifluoroacetic acid (TFA) was added dropwise under vigorous stirring at room temperature for

hydrolysis. After 24 hours, the DCM was removed by rotary evaporator. The PAA-*b*-PS product was purified by dissolution-precipitation with DMF and methanol and dried in vacuum oven at room temperature.

4.2.3. Characterization

The molecular structure and bromination of efficiency of Br- β -CD was characterized by proton nuclear magnetic resonance spectroscopy (^1H NMR). The molecular weight and polydispersity of star-like PtBA and star-like PtBA-*b*-PS were collected by gel permeation chromatography (GPC) with a G1362A refractive detector, a G1314A variable wavelength detector, one 5 μm LP gel mixed bed column (molecular range: 200~3 $\times 10^6$ g/mol), and one 5 μm LP gel column (500 \AA , molecular range: 500~2 $\times 10^4$ g/mol), calibrated using monodisperse linear PS as standard. THF was used as mobile phase with a flow rate of 1.0 ml/min at 35°C. The molecular weight of each arm of PtBA and PtBA-*b*-PS in the star-like nonlinear polymers were determined by ^1H NMR using Bruker Avance III 400 nuclear magnetic resonance spectroscopy using CDCl_3 as solvent. The successful hydrolysis of PtBA-*b*-PS into PAA-*b*-PS was confirmed by Nicolet 6700 Fourier-transform infrared spectroscopy (FT-IR). The morphologies of inorganic NPs were obtained using Hitachi HT7700 transmission electron microscopy (TEM) operating at 120 kV. TEM samples were prepared by depositing NP hexane or water dispersion on a carbon film-supported copper grid.

4.2.4. Synthesis of 0D Nanoparticles

(a) Synthesis of CFO, NFO, and Fe_3O_4 nanoparticles: Star-like PAA-*b*-PS nanoreactor was dissolved in diphenol ether (DPE) followed by adding certain amount of precursors ($\text{Co}(\text{acac})_2$ and $\text{Fe}(\text{acac})_3$, $\text{Ni}(\text{acac})_2$ and $\text{Fe}(\text{acac})_3$, $\text{Fe}(\text{acac})_2$ and $\text{Fe}(\text{acac})_3$ at stoichiometric ratio, for CFO, NFO, and Fe_3O_4 , respectively). The mixture was stirred under Ar flow at elevated temperature

overnight to enable the coordination between metal moieties in precursors and -COOH in the PAA blocks and remove residual water in the solvent and precursor. Certain amount of benzyl alcohol (BA) was added to enhance the solubility of inner PAA blocks. The reaction was then brought to 200 °C slowly in 2 hours and kept for 30 minutes. The slow heating up process is aimed to suppress the nucleation of metal oxide nanoparticles outside the nanoreactors, which can be easily formed under a rapid heat up process. Afterwards the reaction was quickly heated to 250 °C and kept at the temperature for 2 hours for the thermal decomposition of precursors and the formation of CFO NPs. The product was purified by dispersion-precipitation with toluene and ethanol for three times. The procedure of synthesis of NFO and Fe₃O₄ nanoparticles was the same as CFO except changing Co(ac)₂ to Ni(ac)₂ and Fe(ac)₂ respectively.

(b) Synthesis of BTO nanoparticles: Star-like PAA-*b*-PS nanoreactor was dissolved in diphenol ether (DPE) and heated up to 130 °C to remove residual water in the solvent. A specific amount of bimetallic alkoxide precursor (barium titanium ethyl hexano-isopropoxide (BaTi(O₂CC₇H₁₅)[OCH(CH₃)₂]₅) was added and stirred at 130 °C overnight to remove the isopropanol in the precursor, which is poor solvent for both PAA and PS blocks. Certain amount of benzyl alcohol (BA) was added to enhance the solubility of inner PAA blocks. The reaction was then started by addition of a certain amount of hydrogen peroxide and kept for 24 hours after temperature was lowered to 100 °C. The product was purified by dispersion-precipitation in toluene and ethanol for three times.

(c) Synthesis of Au nanoparticles: Star-like PAA-*b*-PS nanoreactor was dissolved in anhydrous DMF:BA mixture (v:v=9:1) followed by addition of gold (III) chloride trihydrate (HAuCl₄·3H₂O). The mixture was stirring for several hours to provide enough time for the precursor to coordinate with the inner PAA blocks. Afterwards, the mixture was heated to elevated

temperature under Ar flow, followed by adding certain amount of reducer *tert*-butylamine borane (TBAB) dropwise. The color of the reaction solution gradually changed from yellow to dark red, indicating the formation of Au nanoparticles. The product was purified by dispersion-precipitation in toluene and ethanol for three times.

(d) Synthesis of CsPbBr₃ perovskite nanoparticles: Star-like PAA-*b*-PS nanoreactor was dissolved in anhydrous DMF followed by addition of certain amount of cesium bromide (CsBr). After fully dissolution of CsBr, stoichiometric amount of lead bromide (PbBr₂) was added and stirred for several hours. Small amount of nanoreactor-precursor solution was then dropped in toluene to trigger the nucleation of CsPbBr₃. The toluene solution color changed from colorless to green under UV light, indicating the formation of CsPbBr₃ nanoparticles. The product was purified by centrifugation and redispersion in toluene.

4.3. Results and Discussion

As shown in **Figure 4.2.**, the esterification of 21 hydroxyl groups on β -CD with BiBB was confirmed by the ¹H NMR spectrum with CDCl₃. The bromination efficiency was calculated to 95% be from the ratio of integral area of peak a to peak b, indicating that almost all the hydroxyl groups on β -CD were converted into bromine containing ATRP initiating site.⁴⁴ In theory, 21 polymer chains with similar molecular weight could be grafted from the Br- β -CD macroinitiator by ATRP.

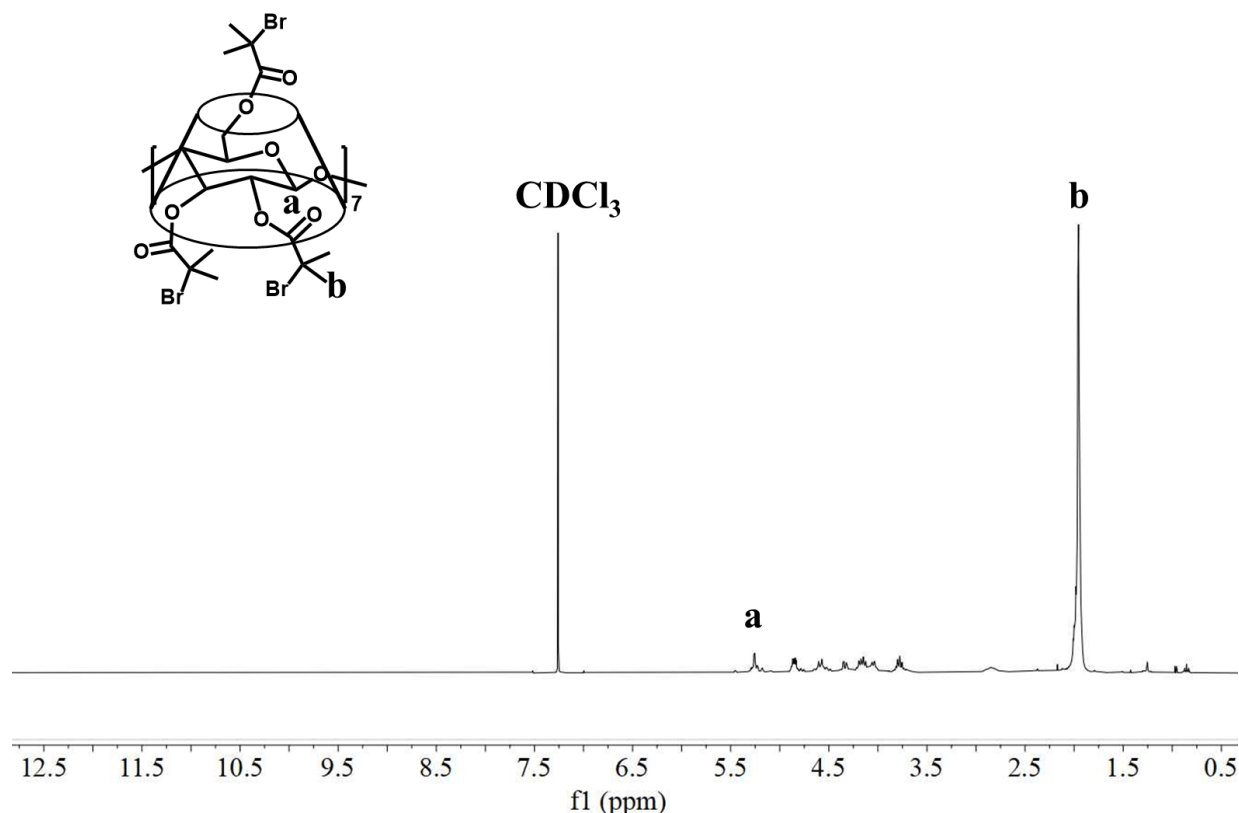


Figure 4.2. ^1H NMR spectrum of the Br- β -CD macroinitiator.

The total molecular weight and polydispersity index (PDI) of the PtBA and PtBA-b-PS star-like nonlinear block copolymer were obtained by GPC. Three batches of PtBA star-like polymer with different molecular weight were synthesized, showing the ability to control length of PtBA blocks which determine the size of the nanoparticles formed inside the nanoreactors. (**Figure 4.3. a**) Meanwhile, the outer block PS with various molecular weights were also synthesized to find an optimal ratio between the length of PAA (converted from PtBA) and PS so that the PS are not too long to restrict the diffusion of precursors into the PAA region nor too short to expose the surface of nanoparticles to the environment.

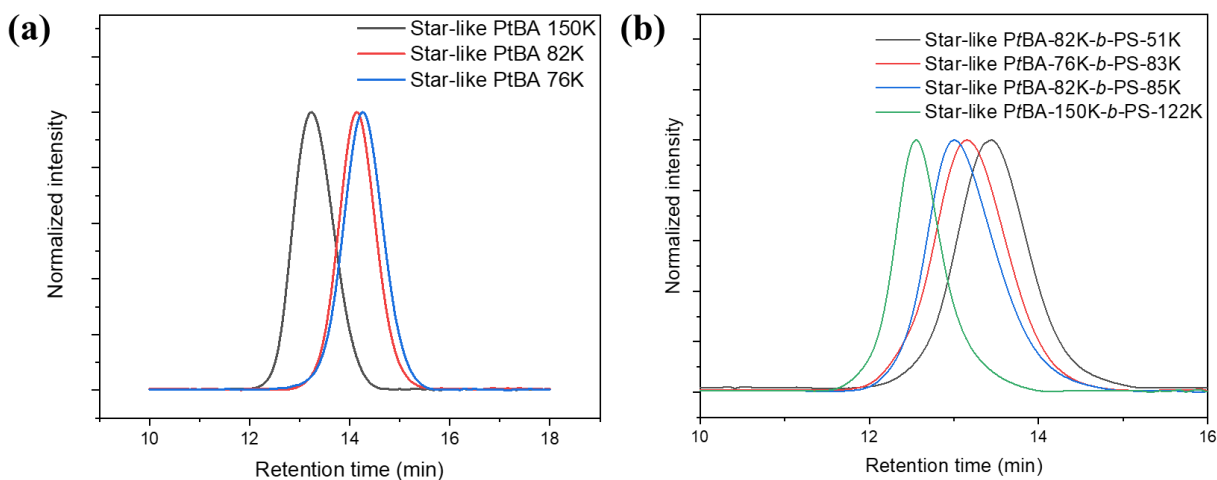


Figure 4.3. GPC traces of (a) PtBA star-like polymers; and (b) PtBA-*b*-PS star-like block copolymers.

^1H NMR was also used to confirm the molecular structure of PtBA star-like polymer and to determine the degree of polymerization and molecular weight of single chain of PtBA grafted onto the Br- β -CD macroinitiator. As shown in **Figure 4.4.**, the molecular weight of each arm of PtBA can be calculated from the ratio between area of peak b ($\delta=1.45$ ppm, methyl protons in *tert*-butyl group) and peak a ($\delta=1.21$ ppm, methyl protons at the α -end of PtBA chain).^{44, 80}

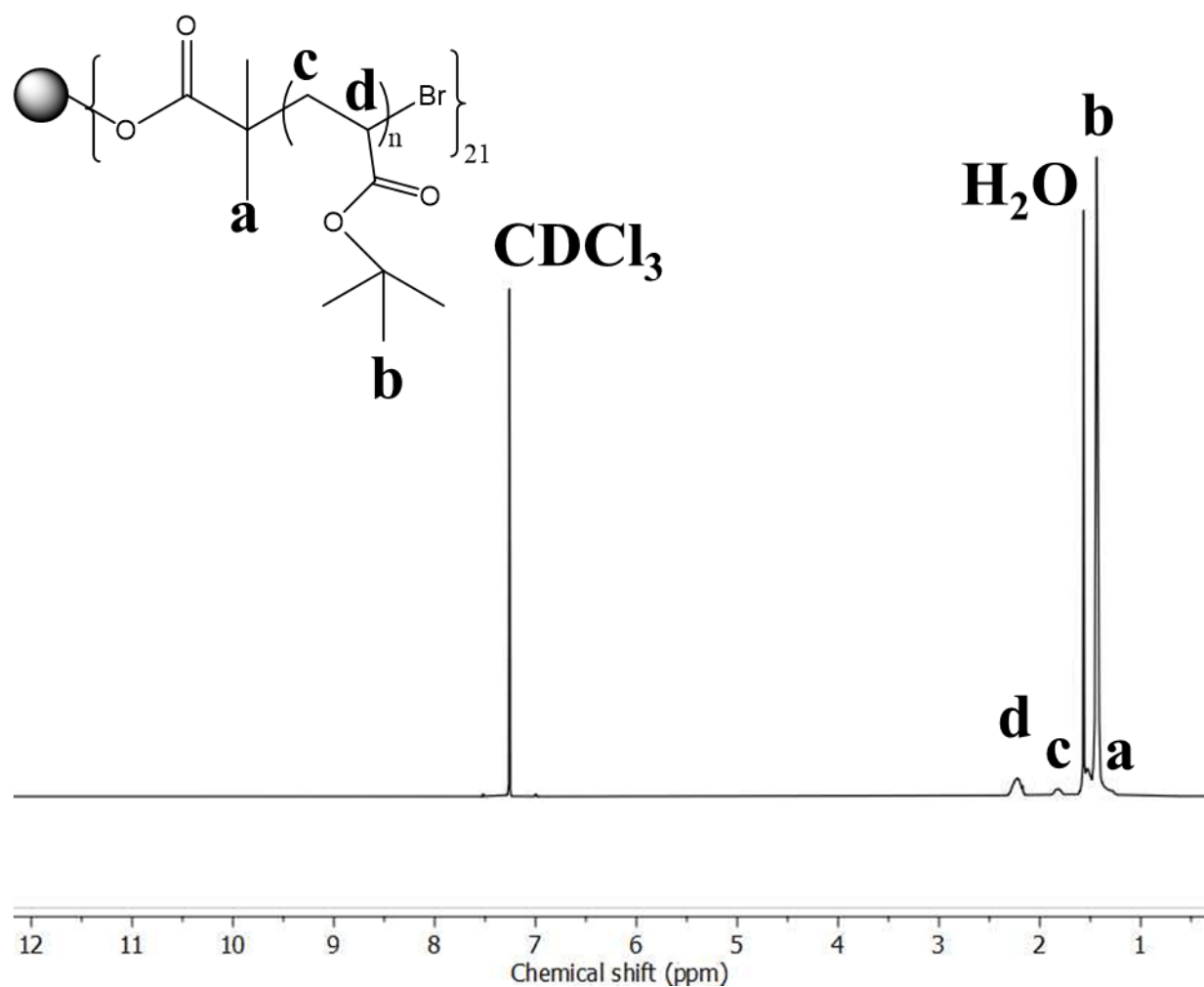


Figure 4.4. Typical ^1H NMR spectrum of the PtBA star-like polymer.

After ATRP of PtBA, the star-like polymer can be used as macroinitiator to further grow the second block on each arm. As shown in **Figure 4.5.**, ^1H NMR spectrum confirms the successful grafting of PS from the PtBA star-like macroinitiator. Similarly, the degree of polymerization and molecular weight of PS on each arm can be calculated from the ratio of area of peak g (all protons in the benzyl ring) to peak a ($\delta=1.21$ ppm). Detailed molecular weight and molecular weight distribution about each polymer sample can be seen in **Table 4.1**. It is noticeable that the molecular

weights obtained from GPC deviate from the results calculated from ^1H NMR. IT is because of the inaccuracy of using GPC to measure the molecular weight of non-linear polymers as the standard used for the calibration of GPC are linear PS polymers. Hydrodynamic volume of a nonlinear polymer is smaller than that of a linear polymer with the same molecular weight and therefore their retention times from the GPC are different.^{160, 161} As a result, the total molecular weight of the star-like polymers obtained from GPC measurements are smaller than the actual molecular weight calculated from ^1H NMR. However, GPC measurements are still necessary and informative in terms of indicating the living-controlled nature of ATRP by the symmetrical shape of the trace curve.

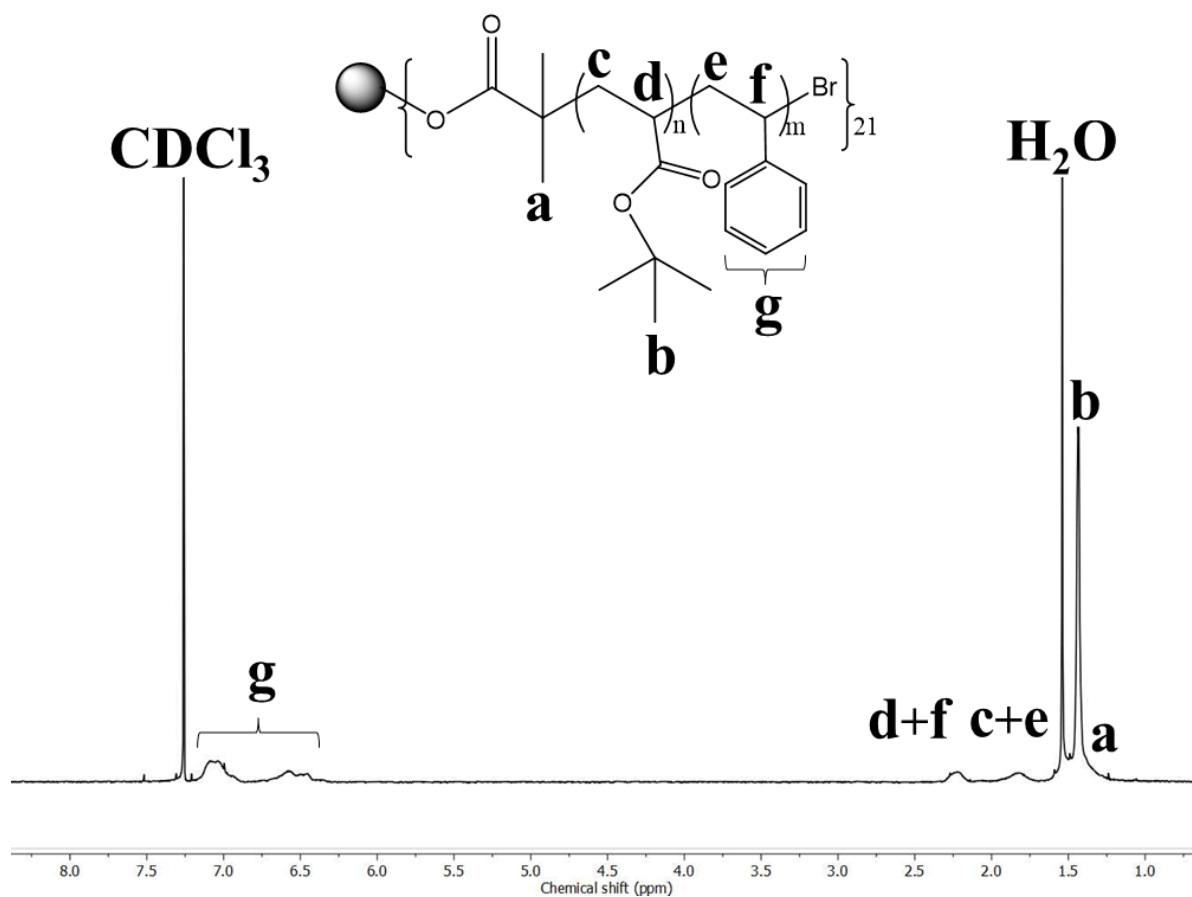


Figure 4.5. Typical ^1H NMR spectrum of the PtBA-*b*-PS star-like block copolymer.

Table 4.1. Molecular Weight of PtBA-*b*-PS star-like block copolymers

	^a M _n , PtBA	^b M _n , PtBA single chain	^c M _n , PtBA-PS	^d M _n , PS single chain	^e PDI
PtBA- <i>b</i> -PS-1	82 kg/mol	7.9 kg/mol	133 kg/mol	3.5 kg/mol	1.11
PtBA- <i>b</i> -PS-2	76 kg/mol	7.4 kg/mol	159 kg/mol	4.3 kg/mol	1.16
PtBA- <i>b</i> -PS-3	82 kg/mol	7.9 kg/mol	167 kg/mol	4.3 kg/mol	1.13
PtBA- <i>b</i> -PS-4	150 kg/mol	13.9 kg/mol	272 kg/mol	6.3 kg/mol	1.13

^{a,c}Total number average molecular weights of PtBA and PtBA-*b*-PS star-like polymer were determined by GPC. ^{b,d}Number average molecular weight of each PtBA and PS block were calculated from ¹H NMR. ^ePolydispersity index (PDI) were determined by GPC

The successful hydrolysis of PtBA block into PAA block can be confirmed by comparing the FT-IR spectra of the polymer before and after the reaction. As shown in **Figure 4.6.**, the appearance of a broad absorption peak at 2500 to 3600 cm⁻¹ indicates the formation of carboxylic acid group in the PAA blocks. In addition, the carbonyl stretching shifted from 1726 cm⁻¹ in PtBA to 1700 cm⁻¹ in PAA, further confirming the conversion of PtBA into PAA. The molecular weight of PAA blocks can be calculated from the difference in molecular weight of *t*BA group and acrylic acid group. The molecular weight and distribution of amphiphilic PAA-*b*-PS star-like block copolymer are summarized in **Table 4.2.**

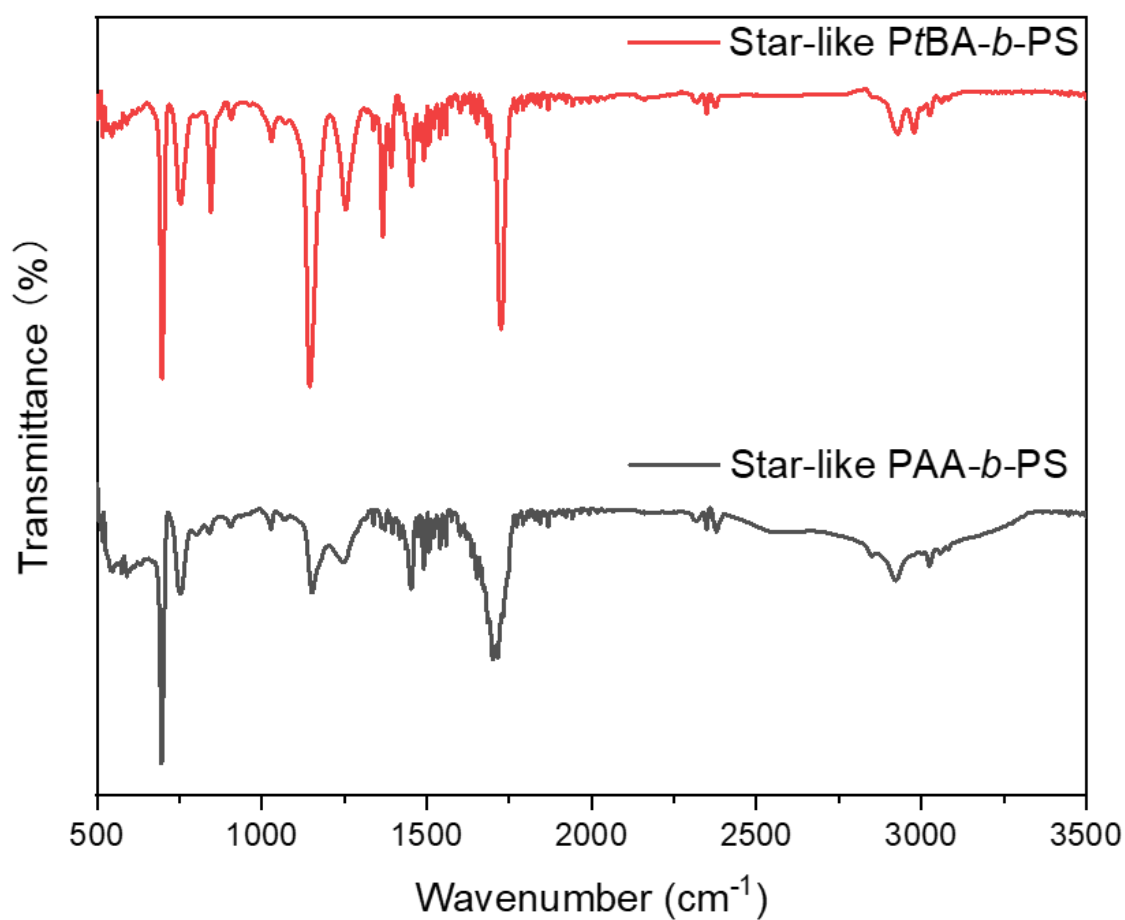


Figure 4.6. FT-IR spectra of PtBA-*b*-PS and PAA-*b*-PS star-like polymers.

Table 4.2. Molecular Weight pf PAA-*b*-PS star-like block copolymers

	^a M_n , PtBA single chain	^b M_n , PAA single chain	^c M_n , PS single chain
PtBA-<i>b</i>-PS-1	7.9 kg/mol	4.4 kg/mol	3.5 kg/mol
PtBA-<i>b</i>-PS-2	7.4 kg/mol	4.1 kg/mol	4.3 kg/mol
PtBA-<i>b</i>-PS-3	7.9 kg/mol	4.4 kg/mol	4.3 kg/mol
PtBA-<i>b</i>-PS-4	13.9 kg/mol	7.8 kg/mol	6.3 kg/mol

^{a,c}Number average molecular weight of each PtBA and PS block were calculated from ¹H NMR.
^bNumber average molecular weights of PAA blocks calculated from the molecular weight difference between *t*BA and acrylic acid.

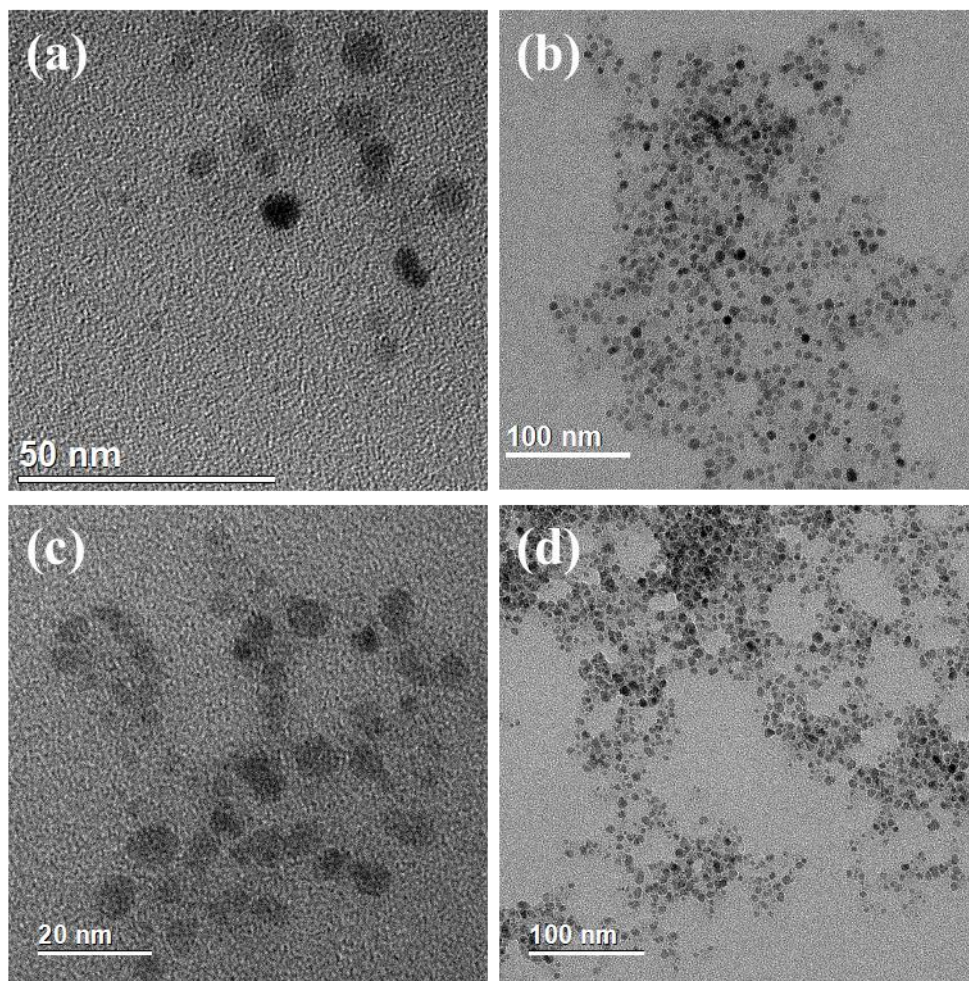


Figure 4.7. TEM images of CFO nanoparticles synthesized with PAA-*b*-PS star-like nanoreactor. (a) and (b) are 6.5 nm CFO nanoparticles using PAA-*b*-PS-1; (c) and (d) are 10 nm CFO nanoparticles using PAA-*b*-PS-4.

As shown in **Figure 4.7.**, CFO nanoparticles with different size were synthesized by using PAA-*b*-PS-1 (**Figure 4.7 a, b**) and PAA-*b*-PS-4 (**Figure 4.7 c, d**) as nanoreactors. The as prepared

CFO nanoparticles exhibit narrow size distribution and uniform spherical structure. The permanently ligated PS out chains enable good dispersity and stability of the CFO nanoparticles in toluene. As shown in **Figure 4.8.**, well dispersed CFO nanoparticles can be accumulated on the vial wall by a magnet bar in 12 mins and redispersed after the removal of magnet by shaking the vial for a few seconds.

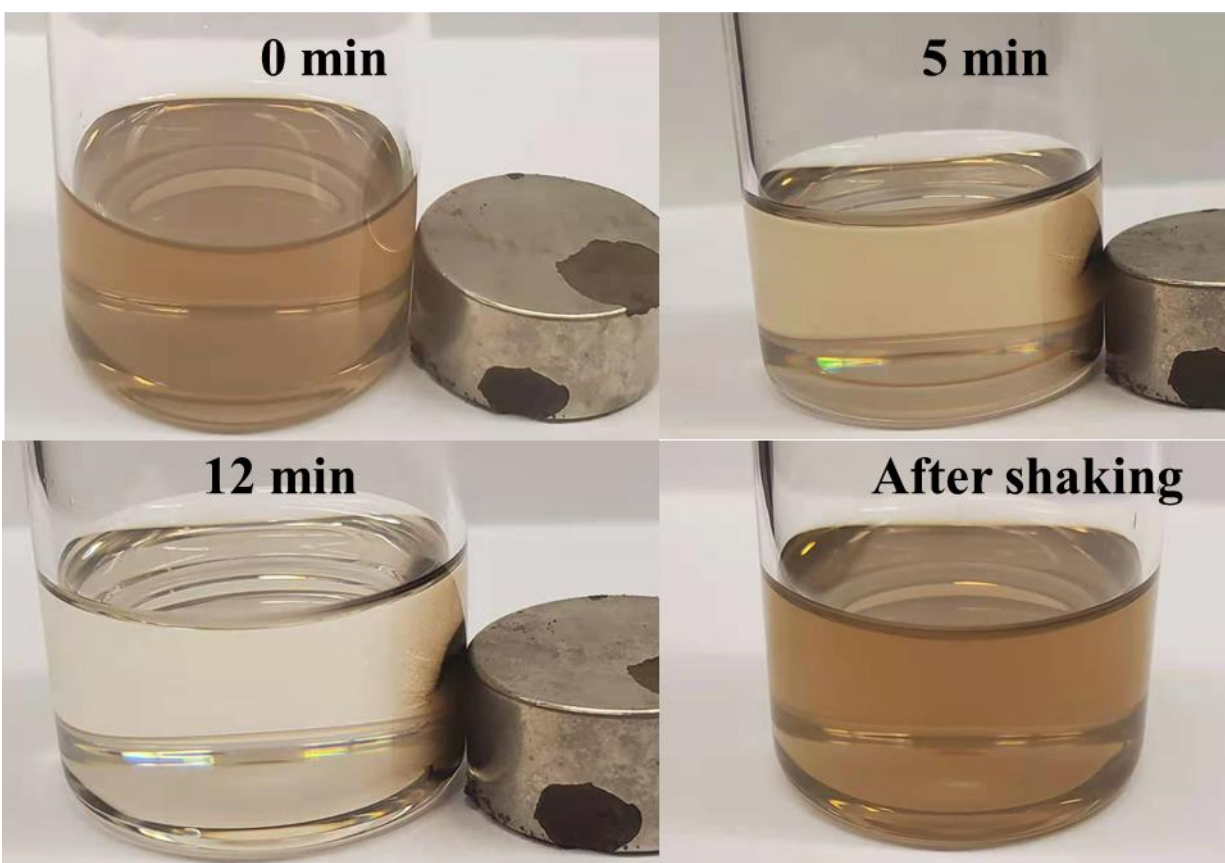


Figure 4.8. Digital images of CFO nanoparticles made from PAA-*b*-PS-41 dispersed in toluene. The nanoparticles can be attracted by magnet placed near the vial and redispersed in toluene easily by hand shaking.

In addition to CFO, other metal oxide nanoparticles including NFO and Fe_3O_4 nanoparticles were also synthesized using PAA-*b*-PS star-like nanoreactors. Perovskite type metal

oxide BTO nanoparticles were also prepared using the nanoreactors via a different synthetic method. As demonstrated in **Figure 4. 9.**, size and shape of the nanoparticles are uniform, showing the capability of the nanoreactors to craft an array of high-quality nanocrystals.

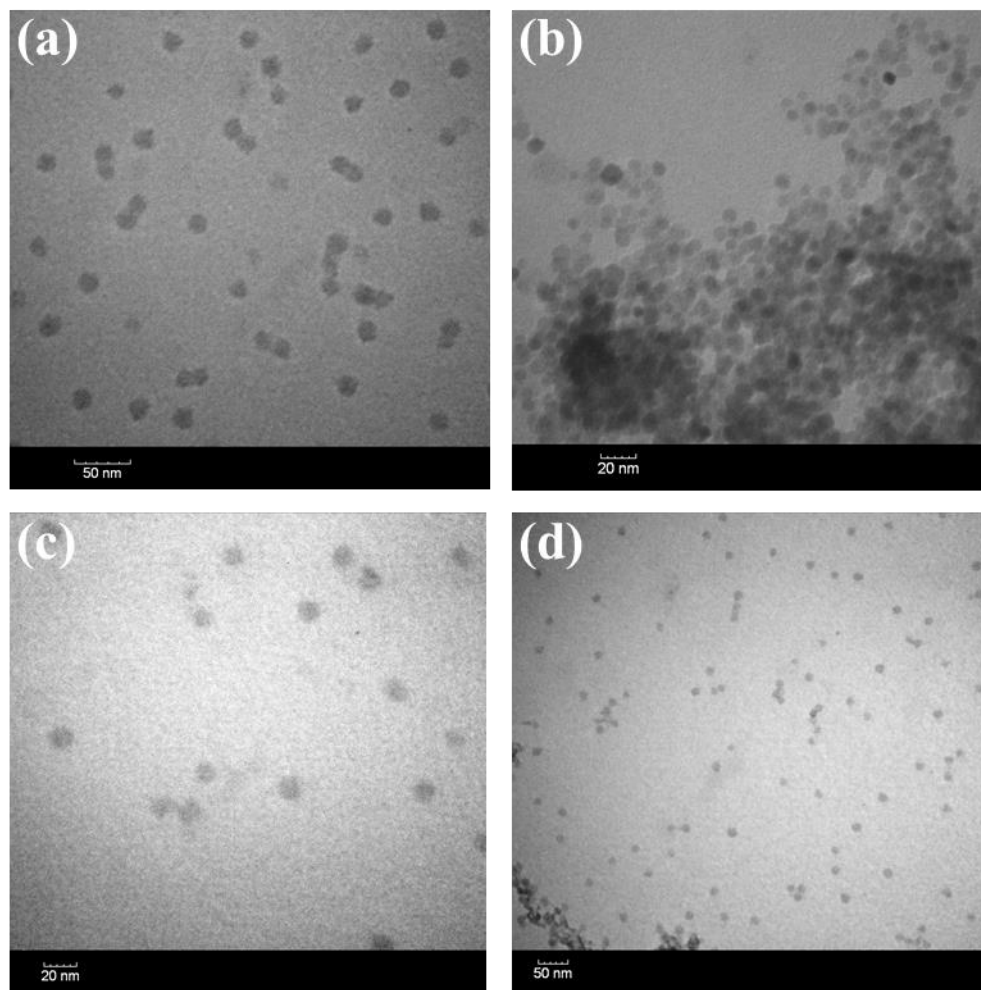


Figure 4.9. TEM images of metal oxide nanoparticle synthesized using PAA-*b*-PS nanoreactors. (a) 12.5 nm NFO nanoparticles synthesized with PAA-*b*-PS-4. (b) 7.3 nm Fe₃O₄ nanoparticles using PAA-*b*-PS-1; (c) and (d) 13.6 nm BTO nanoparticles using PAA-*b*-PS-4.

Moreover, other types of nanoparticles were also prepared with PAA-*b*-PS star-like nanoreactors. For example, plasmonic Au and luminescent CsPbBr₃ perovskite nanoparticles were

prepared and showed in **Figure 4.10**. The results further confirm that the nonlinear block copolymer nanoreactor strategy is a general and robust method for the synthesis of a group of well controlled 0D nanoparticles.

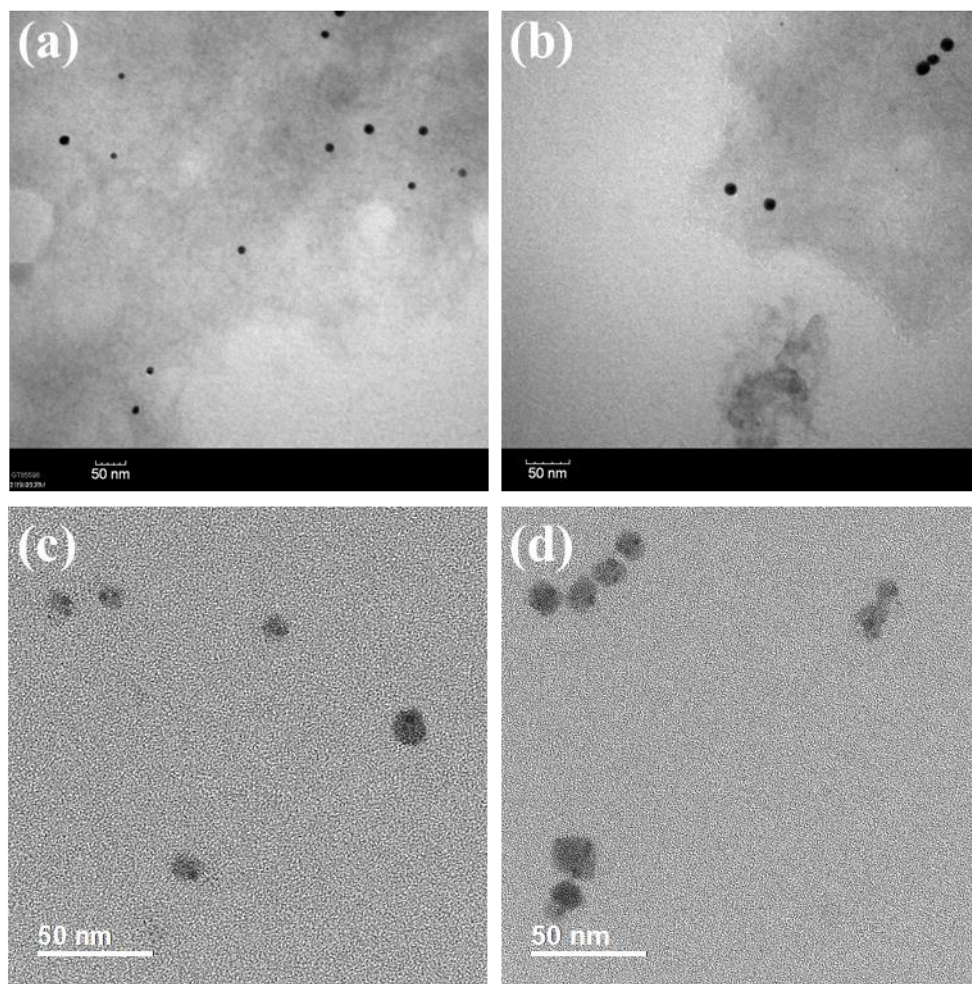


Figure 4.10. TEM images of (a) 13.6 nm Au nanoparticle synthesized using PAA-*b*-PS-4; and (b) 12.6 nm CsPbBr₃ perovskite nanoparticles synthesized with PAA-*b*-PS-4.

It is worth noting that the covalently connected PS out blocks offer a superior stability of the nanoparticles. **Figure 4.11.** shows CsPbBr₃ nanocrystals synthesized using star-like nanoreactors maintained their photoluminescence under UV after even 10 months of storage in

ambient environment, indicating excellent stability against environment, especially moistures. As a comparison, CsPbBr₃ nanocrystals prepared without nanoreactor, or conventional ligands exhibit no luminescent after 2 months (more tests should be done in a shorter period after the synthesis).

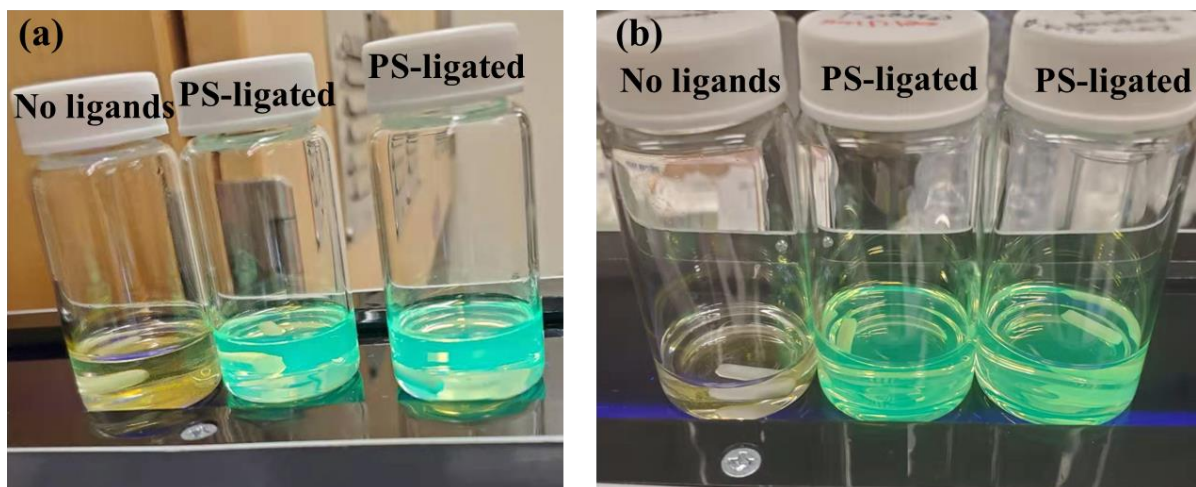


Figure 4.11. CsPbBr₃ nanoparticle dispersed in toluene and store in lab for (a) 2 months and (b) 10 months. The nanoparticles prepared using star-like nanoreactors show excellent stability.

The ability to craft a series of nanoparticles out of the star-like nanoreactor built on solid foundation for the further investigation of the size dependent properties of nanoparticles of interests. In this study, I systematically studied and size and core-shell ratio dependent magnetic field assisted OER enhancement in CFO nanoparticles, more detailed studies were conducted. The precisely controlled size of CFO nanoparticles was realized via carefully exploring and adjusting the reaction condition and purification process.

First, the heating process effect was investigated. When reaction mixture was quickly heated up to 250 °C, intense decomposition of precursors during the heating process both inside and outside the nanoreactor templates, resulting in much lower yield, more tedious purification,

and wide size distribution of the final products. When slow heat-up strategy is applied, the nucleation happens slowly and predominantly in the space taken by PAA blocks inside the nanoreactors because heterogeneous nucleation in the presence of PAA polymer chains is more energy favorable over the homogeneous nucleation in solution.

Since nanoscale spinel structured metal oxides can be easily formed at high temperature even without ligands or surfactant. It is necessary to separate the “naked” NPs formed outside the nanoreactors from the polymer ligated CFO NPs. Fortunately, due to the lack of ligands on the surface and the magnetic nature of the nanoparticles formed outside the nanoreactors, they turned to aggregate strongly. (**Figure 4.12.**) In sharp contrast, as shown in **Figure 4.13.**, nanoparticles formed inside nanoreactors are well dispersed in appropriate solvents (such as toluene and THF), even when the reaction time is extended to 12 hours. Moreover, obvious precipitation could be observed by eyes after overnight storage of CFO nanoparticles without template in solvents, as demonstrated in **Figure 4.14. (a)**. After centrifugation at 6000 rpm for 10 minutes, vast majority of the nanoparticles are easily isolated from the solvents. On the other hand, CFO NPs prepared via nanoreactor strategy remain well dispersed in solution even after overnight storage and centrifugation in toluene or THF (good solvents for PS), as can be confirmed in **Figure 4.14 (b)**. The substantial difference between NPs with and without polymer “hairs” makes it possible to separate them completely.

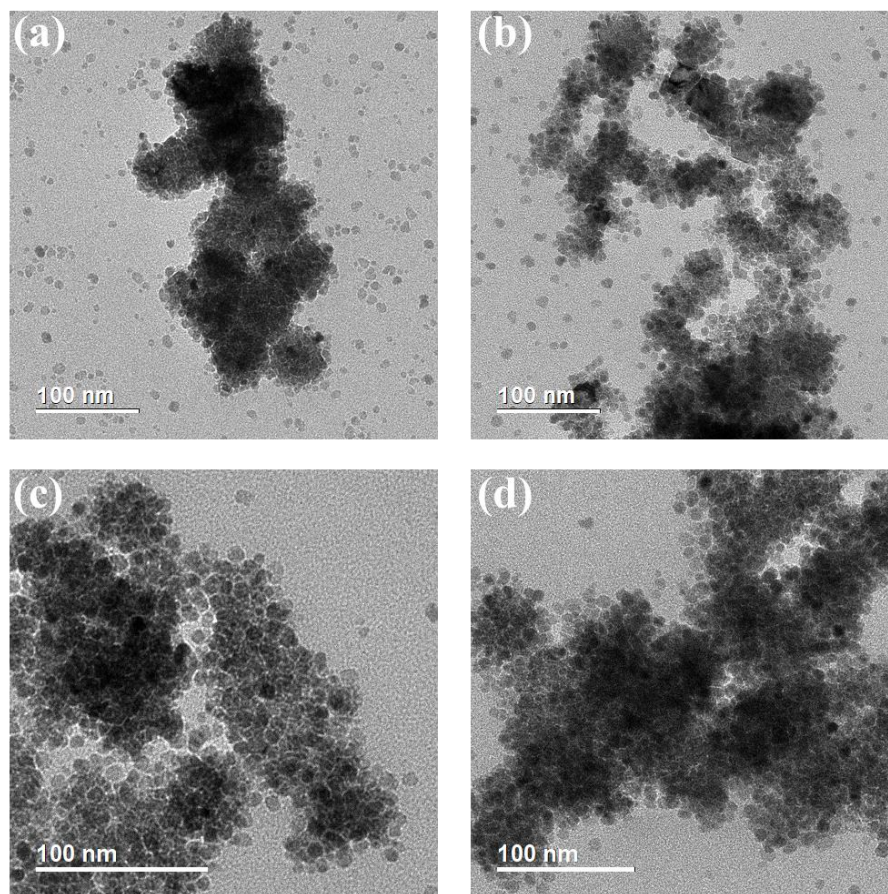


Figure 4.12. TEM images of as synthesized CFO NPs reacted for (a) 2 hours, (b) 5 hours, (c) 8 hours, and (d) 12 hours at 250 °C, without template.

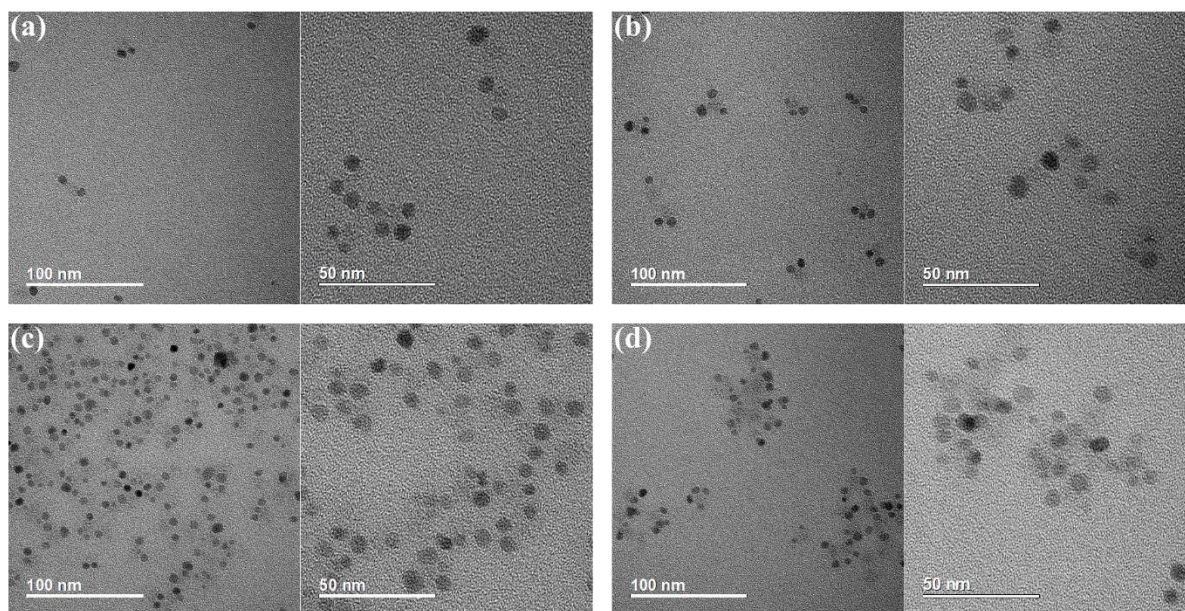


Figure 4.13. TEM images of as synthesized CFO NPs reacted for (a) 2 hours, (b) 5 hours, (c) 8 hours, and (d) 12 hours at 250 °C, using PAA-*b*-PS-1 as nanoreactor.

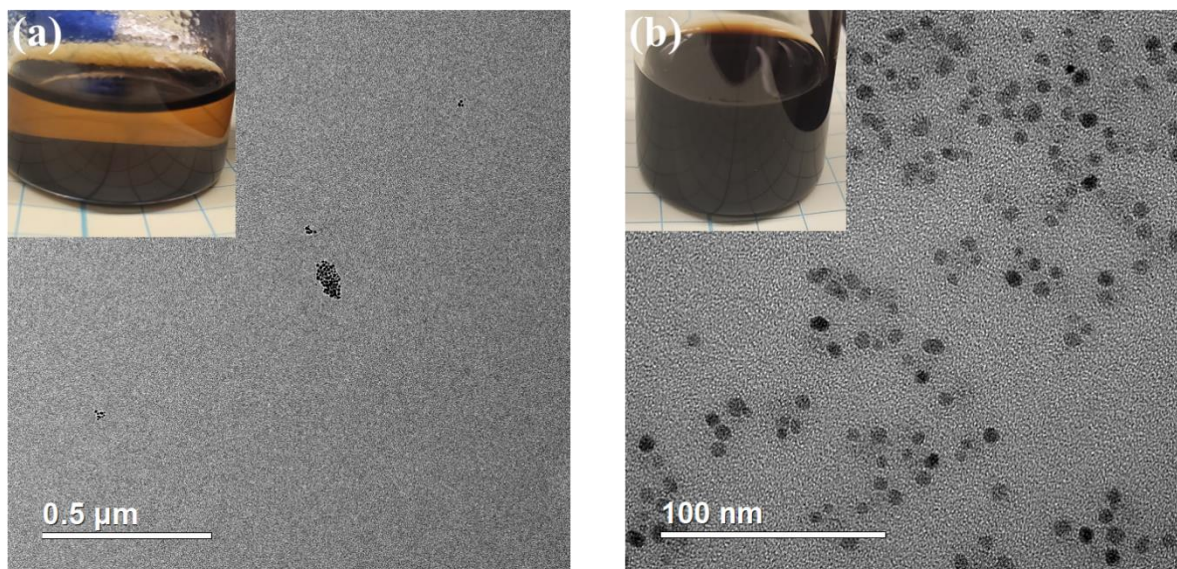


Figure 4.14. TEM images of CFO NPs synthesized (a) without template and (b) using PAA-*b*-PS-1 as nanoreactor after storing in THF for overnight and centrifugation at 6000 rpm for 10 minutes.

minutes. Insets are digital images of NP dispersion in THF after overnight storage, showing the supreme dispersity of PS-ligated CFO NPs in THF.

Furthermore, the reaction kinetics were also carefully examined by taking aliquots from reaction mixture at different time at the decomposition temperature. As shown in **Figure 4.15. (a-h)**, the decomposition and nucleation has already taken place during the heating-up process. As the reaction progresses, NPs continued to increase in size until their growth is restricted by the nanoreactor. (**Figure 4.15. (I)**)

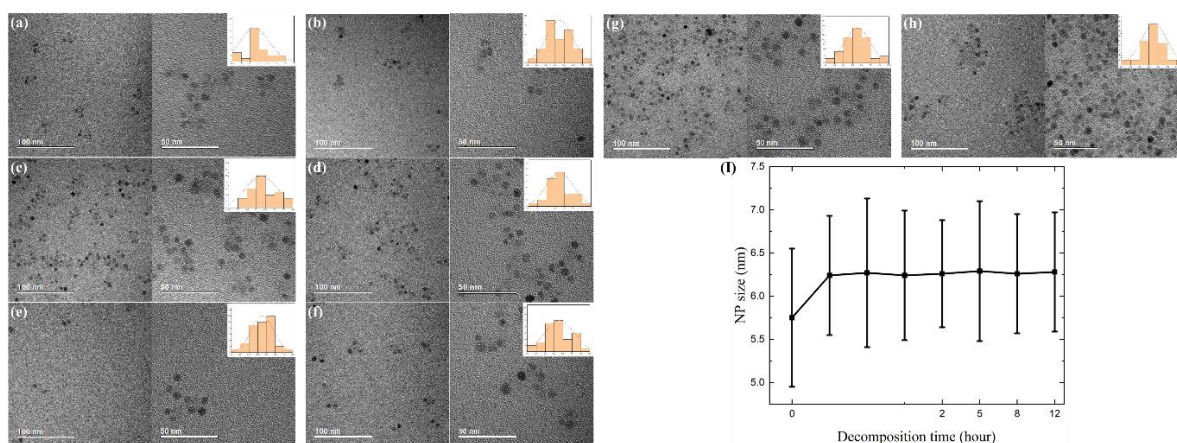


Figure 4.15. (a-h) TEM images of CFO NPs synthesized using PAA-*b*-PS-1 as nanoreactor at different times during the heating process and reaction; (I) plot of NP size as a function of reaction time

The successful preparation of high-quality PS-ligated CoFe_2O_4 NPs enable the further investigation of the surface reconstruction for generating $\text{CoFe}_2\text{O}_4/\text{CoFe}_2\text{O}_x\text{H}_y$ core/shell NPs. This process involves two steps, as illustrated in **Figure 4.16**. Firstly, sulfur doping at elevated temperature was performed to form a S-doped layer by heating the CFO NPs DMF solution to certain temperature under nitrogen followed by injection of $(\text{NH}_4)_2\text{S}/\text{DMF}$ solution. The resulting

product was washed with acetone and methanol and redispersed in toluene. Secondly, the samples were cycled via cyclic voltammetry in 1M KOH to trigger the surface reconstruction.

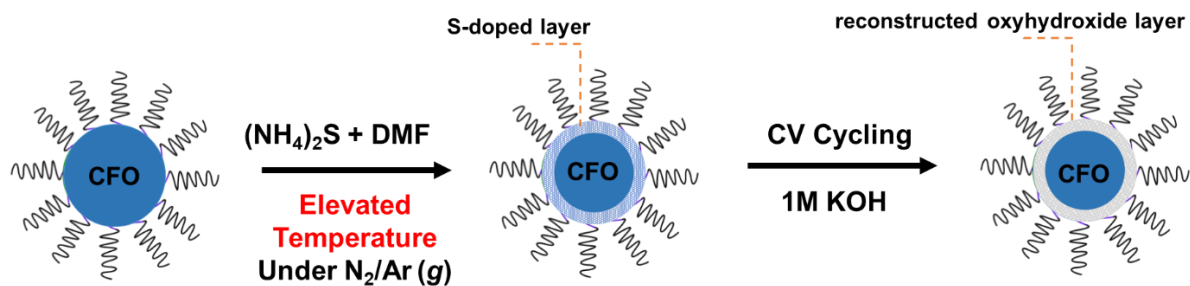


Figure 4.16. Illustration of the two-step surface reconstruction process.

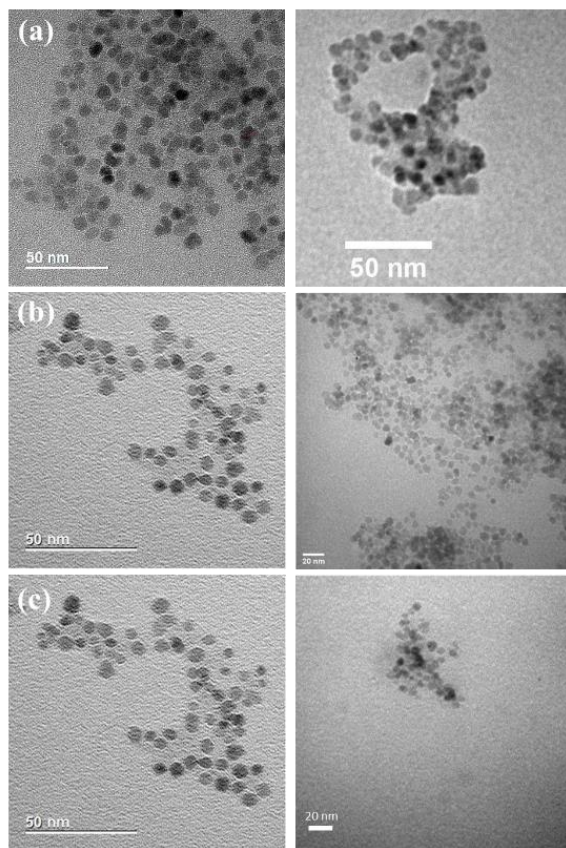


Figure 4.17. TEM images of PS ligated CFO NPs before (left column) and after (right column) S-doping at different reaction conditions. NP size changed from 9.6 ± 1.1 nm to 6.5 ± 1.4 nm when S-doping was conducted at 100 °C for 5 minutes (a); NP size remain almost unchanged when reaction temperature is lowered to 70°C and kept for 1 (b) or 2 minutes (c).

As can be observed in **Figure 4.17**, a too high temperature or a too long reaction time during sulfur doping process could lead to severe damage to the sample. Therefore, sample AE-1-PS-CFO and AE-2-PS-CFO were produced by sulfur doping at 70 °C for only 1 and 2 minutes, respectively, to avoid structural damage. However, the OER activity of surface reconstructed CFO/CoFe₂O_xH_y is decrease and a negative correlation between the degree of surface reconstruction and OER activity can be clearly noticed in **Figure 4.18**. One possible reason is material loss during cycling and reconstruction. In order to solve this problem, S-doped CFO NPs were deposited on nickel foams (NFs) via electrophoresis deposition. After CV cycling and magnetization under magnetic field (<0.5 T) for 1 hour, the samples showed enhanced performance compared to those did not undergo magnetization treatment (**Figure 4.19**). This result indicates that our strategy has the potential to keep enhancing the OER activity of CFO NPs. More detailed study is being conducted to systematically investigate the magnetic field enhancement OER activity of surface reconstructed CFO NPs by the collaborators of this project.

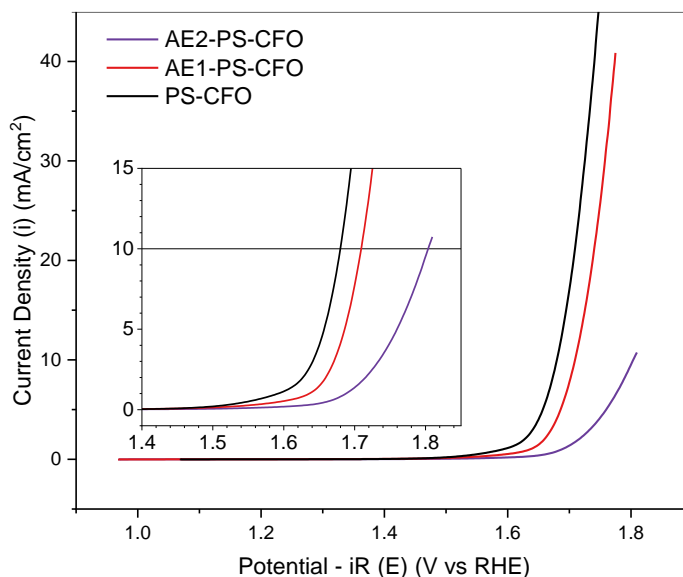


Figure 4.18. The linear sweep voltammetry (LSV) curve of CFO NPs after surface reconstruction.

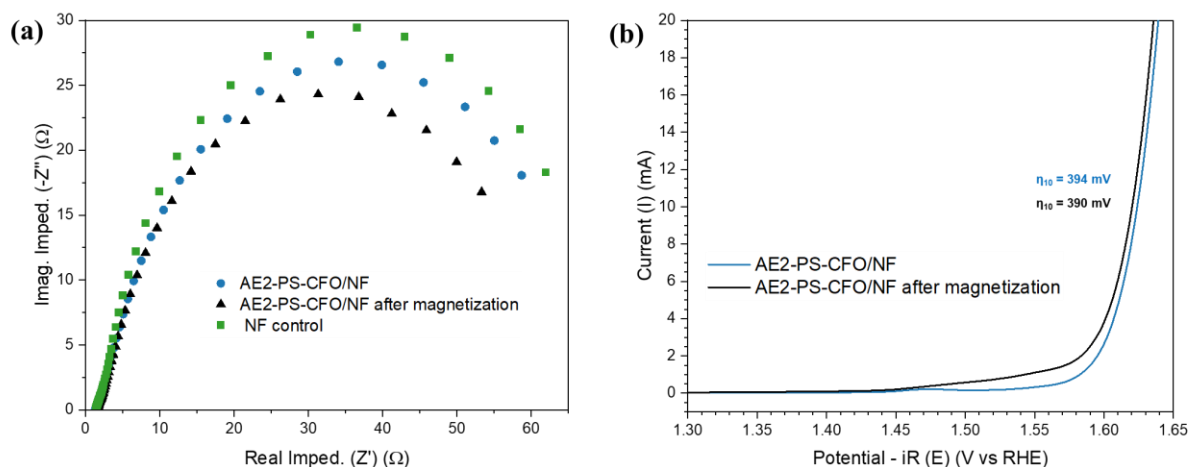


Figure 4.19. (a) Nyquist plots for pure nickel foam, surface reconstructed CFO NPs on NF, and surface reconstructed CFO NPs after magnetization obtained from electrochemical impedance spectroscopy. (b) LSV curves of surface reconstructed CFO NPs before and after magnetization.

4.4. Conclusion

In this chapter, it is successfully demonstrated that star-like block copolymers can be prepared by sequential ATRP and used as nanoreactors for the craft of a set of inorganic nanoparticles. Moreover, with the ability of precisely control the size of nanoparticles, the nanoreactor strategy provides a platform to study nanoparticles' size dependent properties. It is preliminarily demonstrated that with careful surface reconstruction and magnetization, paramagnetic CoFe_2O_4 nanoparticles could achieve an enhanced OER activity. More systematic study is still undergoing by my collaborators.

Chapter 5. Synthesis of Bottlebrush-like Block Copolymer as Nanoreactor for 1D Nanorods

5.1. Introduction

Cylindrical architecture of bottlebrush-like polymers offers them with unique properties and promising applications in photonic crystals,^{162, 163} biomedicine,^{164, 165} self-assembled superstructures,^{166, 167} solid electrolyte,^{168, 169} super elastomers^{170, 171}, etc. It is important to point out that bottlebrush-like polymers are unimolecular cylindrical micelles that are stable against external stimuli, unlike conventional micelles formed by assembly of linear polymers dynamically. The conceptually intuitive 1D structures of the bottlebrush-like block copolymers provide unprecedented access to unimolecular and anisotropic nanoreactors that will lead to straightforward synthesis of 1D nanomaterials. 1D cylindrical bottlebrush-like block copolymers not only provide excellent compartmentalized domains in the inner block of the side chains for the loading of the precursors, but also allow confinement to grow nanomaterials along the backbone. The outer block polymer chains provide tunable solubility of the resulting 1D nanomaterials and prevent agglomeration and precipitation in solution. Typically, 1D nanomaterials prepared via the nanoreactor strategy exhibit superior properties such as stability, flexibility, solubility, over other methods. In addition, the precise controllability of the bottlebrush-like block copolymer parameters such as backbone length, length of each both in the side chains, side chain compositions, and functionalities allows the bottlebrush-like block copolymers to be used as uniform nanoreactors for the template-directed preparation of 1D nanomaterials.

5.2. Experimental Section

5.2.1. Materials

1-Methylimidazole ($\geq 99\%$), allyl chloride (98%), Toluene (anhydrous, 99.8%), dichloromethane ($>99.5\%$), α -bromoisobutyryl bromide (BiBB, 98%), acetic acid (99.7%), diethyl ether (inhibitor-free, 99.9%), ethanol (anhydrous, 99.5%), anhydrous dimethylformamide (DMF, $>99.8\%$), 1-methyl-2-pyrrolidinone (NMP, anhydrous, 99.5%), sodium bicarbonate (NaHCO_3 , 99.7%), calcium hydride (CaH_2 , 95%), N,N,N',N',N''-pentamethyldiethylene triamine (PMDETA, 99%), aluminum oxide powder (activated, neutral, ~ 325 mesh), tetrahydrofuran (THF, inhibitor-free, $\geq 99.9\%$), acetone (99.5%), methanol (99.8%), anisole (99%), 2-butanone (99.0%), trifluoroacetic acid (TFA, 99.9%), deuterated dimethyl sulfoxide (DMSO-d_6 , 99.9%), and deuterated chloroform (CDCl_3 , 99.96%) were purchased from Sigma-Aldrich and used as received.

Cellulose (microcrystalline, powder) was dried in vacuum oven at 40 °C for 48 h and azeotropic distilled with toluene at 100 °C prior to bromination reaction. Copper (I) bromide (CuBr , 98%, Sigma-Aldrich) was mixed with excess acetic acid and stirred for 30 min, and then filtered to collect the precipitant. Afterwards, CuBr was washed with ethanol for 3 times, followed by washing with diethyl ether, and then dried in vacuum at room temperature overnight. Styrene (St, 99.9%, Sigma-Aldrich) and *tert*-butyl acrylate (*t*BA, 98%, Sigma-Aldrich) were distilled over CaH_2 under reduced pressure prior to use.

5.2.2. Methods

Figure 5.1. shows the synthetic route of the bottlebrush-like PAA-*b*-PS nanoreactor. The detailed synthetic procedure is summarized as following:

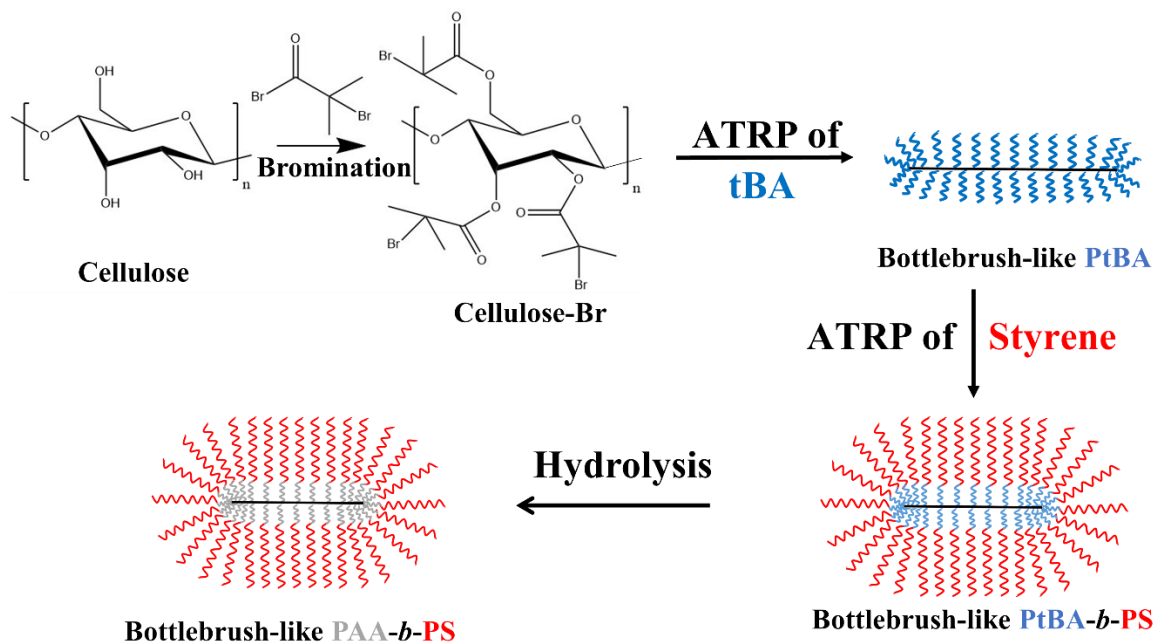


Figure 5.1. Schematic illustration of the synthesis of bottlebrush-like block copolymer (i.e., bottlebrush-like PAA-*b*-PS) nanoreactor.

(1) Synthesis of ionic liquid 1-allyl-3-methylimidazolium chloride (AMiMCl): The ionic liquid is synthesized by mixing allyl chloride and 1-methylimidazole in a round bottom flask and refluxing at 55°C for 5 hours under vigorous stirring. The crude solution was purified by removing unreacted materials via rotary evaporator and washing with ethyl ether. After evaporating ethyl ether, the product becomes bright yellow viscous liquid.

(2) Synthesis of brominated cellulose initiator (Cellulose-Br): Cellulose microcrystal powder was dried in vacuum oven at 80 °C overnight and residual water was further removed by azeotropic distillation with toluene in a large round bottom flask. AMiMCl ionic liquid was then added into the flask to dissolve cellulose. The viscous mixture was heated to 60 °C under slow stirring until complete dissolution of white cellulose powder, yielding a yellow transparent solution. Subsequently, anhydrous DMF and NMP were added into the solution to dilute the mixture and

generate a basic environment for the following bromination reaction. BiBB was then added dropwise into the mixture under stirring at 0 °C. After 2 hours, the temperature was raised to room temperature and the reaction was kept for 24 hours. After the reaction was finished, the crude solution was dropped in water to yield cellulose-Br powders. After filtering and drying, the cellulose-Br was purified by dissolving in acetone and precipitating in water for several times and dried in vacuum oven.

(3) Manual fractional precipitation of cellulose-Br: Because the raw cellulose microcrystal have a wide molecular distribution, manual fractional precipitation was applied to separate cellulose-Br into different batches with narrow molecular distribution that can be used as macroinitiator for the synthesis of bottlebrush-like nanoreactors (i.e., the length of backbone of the nanoreactor, which is the length of 1D nanorods, will be uniform). Typically, cellulose-Br was dissolved in large amount of acetone under stirring, water was added dropwise until the solution start to turn translucent. The flask was kept still until phase separation is finish. The precipitation was collected, and the clear solution was used for the next cycle of fractional precipitation following the same procedure.

(4) Synthesis of poly(*tert*-butyl acrylate) (PtBA) bottlebrush-like polymer: Cellulose-Br, CuBr, PMDETA, *t*BA and MEK were mixed in an ampoule and degassed by N₂ bubbling for 1 hour. Afterwards, the ampoule was sealed and put into an oil bath at 40 °C. The ampoule was taken out from the oil bath and dipped into ice bath and open to atmosphere at different desired time to terminate the polymerization. The crude solution was diluted with acetone, passed through neutral alumina column to remove the catalyst, and precipitated in a water/methanol mixture (v:v=1:1). After filtration, the product was dried in vacuum oven at room temperature.

(5) Synthesis of poly(*tert*-butyl acrylate)-*block*-polystyrene (PtBA-*b*-PS) bottlebrush-like block copolymer: PtBA bottlebrush-like polymer, CuBr, PMDETA, styrene and anisole were mixed in an ampoule and degassed by N₂ bubbling for 1 hour. Afterwards, the ampoule was sealed and put into an oil bath at 90 °C. The ampoule was taken out from the oil bath and dipped into ice bath and open to atmosphere at different desired time to terminate the polymerization. The crude solution was diluted with THF, passed through neutral alumina column to remove the catalyst, and precipitated in a water/methanol mixture (v:v=1:1). After filtration, the product was dried in vacuum oven at room temperature.

(6) Synthesis of poly(acrylic acid)-*block*-polystyrene (PAA-*b*-PS) bottlebrush-like block copolymer: PtBA-*b*-PS bottlebrush-like block copolymer was first dissolve in DCM into which trifluoroacetic acid (TFA) was added dropwise under vigorous stirring at room temperature for hydrolysis. After 24 hours, the DCM was removed by rotary evaporator. The PAA-*b*-PS product was purified by dissolution-precipitation with DMF and methanol and dried in vacuum oven at room temperature.

5.2.3. Characterization

The molecular structure and bromination of efficiency of Cell-Br was characterized by proton nuclear magnetic resonance spectroscopy (¹H NMR). The molecular weight and polydispersity of Cell-Br before and after fractional precipitation, bottlebrush-like PtBA, and bottlebrush-like PtBA-*b*-PS were collected by gel permeation chromatography (GPC) with a G1362A refractive detector, a G1314A variable wavelength detector, one 5 µm LP gel mixed bed column (molecular range: 200~3×10⁶ g/mol), and one 5 µm LP gel column (500 Å, molecular range: 500~2×10⁴ g/mol), calibrated using monodisperse linear PS as standard. THF was used as mobile phase with a flow rate of 1.0 ml/min at 35°C. The molecular weight of each arm of PtBA

and PtBA-*b*-PS in the bottlebrush like nonlinear polymers were determined by ^1H NMR using Bruker Avance III 400 nuclear magnetic resonance spectroscopy using CDCl_3 as solvent. The successful hydrolysis of PtBA-*b*-PS into PAA-*b*-PS was confirmed by Nicolet 6700 Fourier-transform infrared spectroscopy (FT-IR). Atomic force microscopy (AFM) were conducted with Bruker Dimension Icon 3100 in soft tapping mode.

5.3. Results and Discussion

As shown in **Figure 5.2.**, the esterification of hydroxyl groups on cellulose with BiBB was confirmed by the ^1H NMR spectrum with CDCl_3 . The bromination efficiency was calculated to be close to 100% from the ratio of integral area of peak a ($\delta = 1.6\text{-}2.0$ ppm, methyl protons of cellulose-Br) to protons of cellulose backbone ($\delta = 3.5\text{-}6.0$ ppm), indicating that almost all the hydroxyl groups on cellulose were converted into bromine containing ATRP initiating site.⁶¹

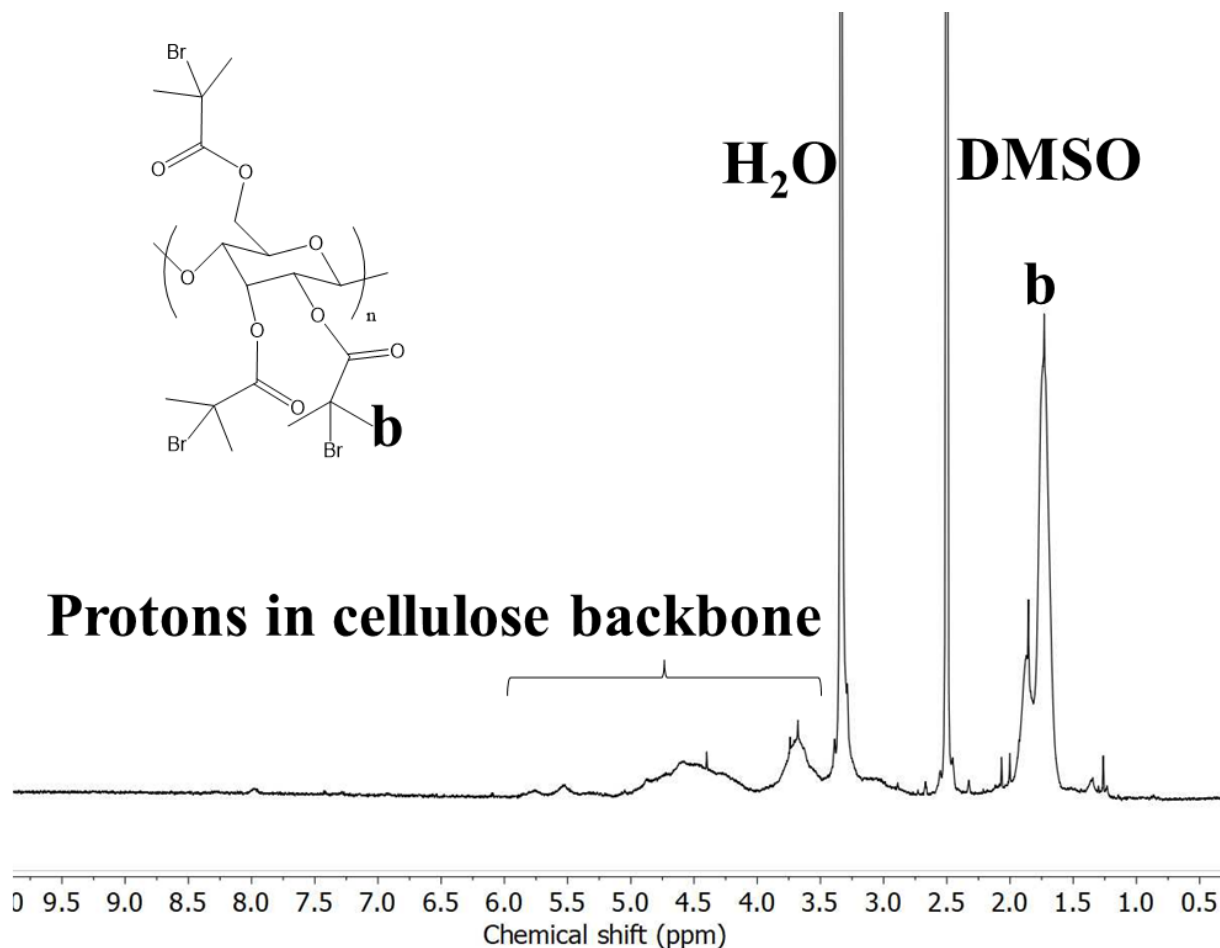


Figure 5.2. ^1H NMR spectrum of the cellulose-Br macroinitiator.

The total molecular weight and polydispersity index (PDI) of cellulose-Br obtained from fractional precipitation, as well as PtBA and PtBA-b-PS bottlebrush-like polymer and block copolymer were obtained by GPC. It can be observed that the original cellulose-Br has very wide molecular distribution. Yet, fractional precipitation produces narrowly distributed cellulose batches that can be used as initiators (**Figure 5.3a**). Three batches of PtBA bottlebrush-like polymer with different molecular weight was synthesized, showing the ability to control length of PtBA blocks which determine the diameter of the nanorods formed inside the nanoreactors.

(Figure 5.3 b) Meanwhile, the outer block PS could be uniformly grafted from the PtBA arms, as indicated by the symmetrical shaped of the GPC trace curve.

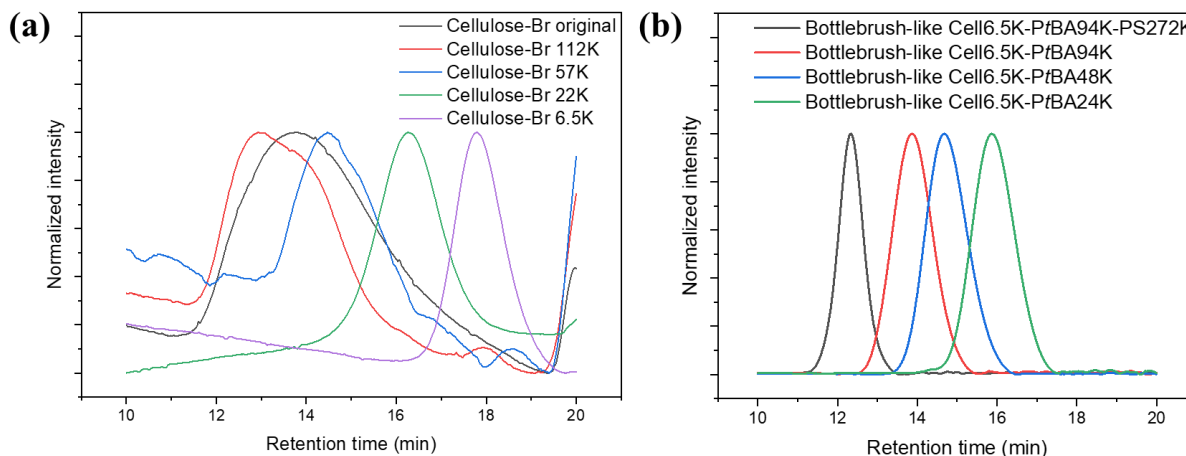


Figure 5.3. (a) GPC traces of cellulose-Br macroinitiators; (b) GPC traces of bottlebrush-like PtBA and PtBA-*b*-PS.

^1H NMR was also used to confirm the molecular structure of PtBA bottlebrush-like polymer and to determine the degree of polymerization and molecular weight of single chain of PtBA grafted onto the cellulose macroinitiator. As shown in **Figure 5.4.**, the molecular weight of each arm of PtBA can be calculated from the ratio between area of peak b ($\delta=1.45$ ppm, methyl protons in *tert*-butyl group) and peak a ($\delta=1.21$ ppm, methyl protons at the α -end of PtBA chain).⁴⁴,

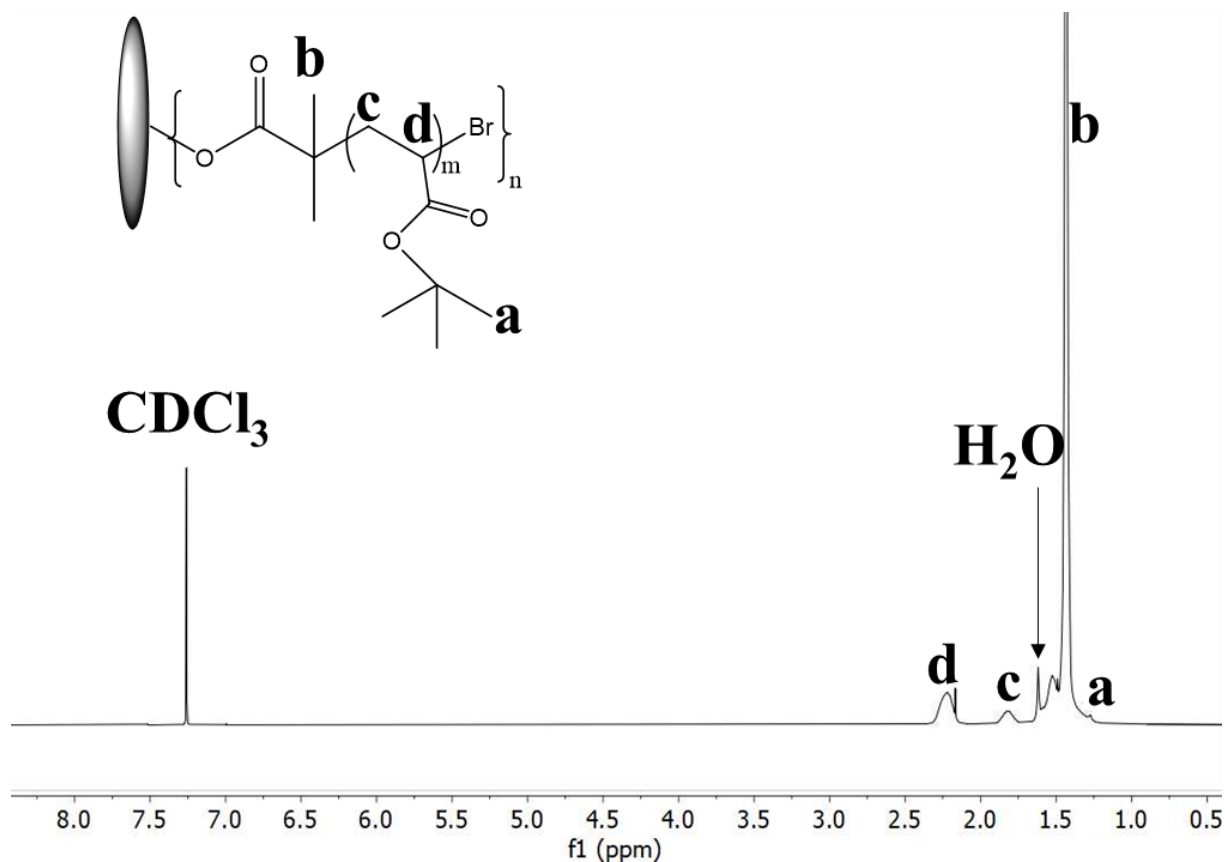


Figure 5.4. Typical ^1H NMR spectrum of the PtBA bottlebrush-like polymer.

After ATRP of PtBA, the bottlebrush-like polymer can be used as macroinitiator to further grow the second block from each arm. As shown in **Figure 5.5.**, ^1H NMR spectrum confirms the successful grafting of PS from the PtBA bottlebrush-like macroinitiator. Similarly, the degree of polymerization and molecular weight of PS on each arm can be calculated from the ratio of area of peak g (all protons in the benzyl ring) to peak a ($\delta=1.21$ ppm). Detailed molecular weight and molecular weight distribution about each polymer sample can be seen in **Table 5.1.**

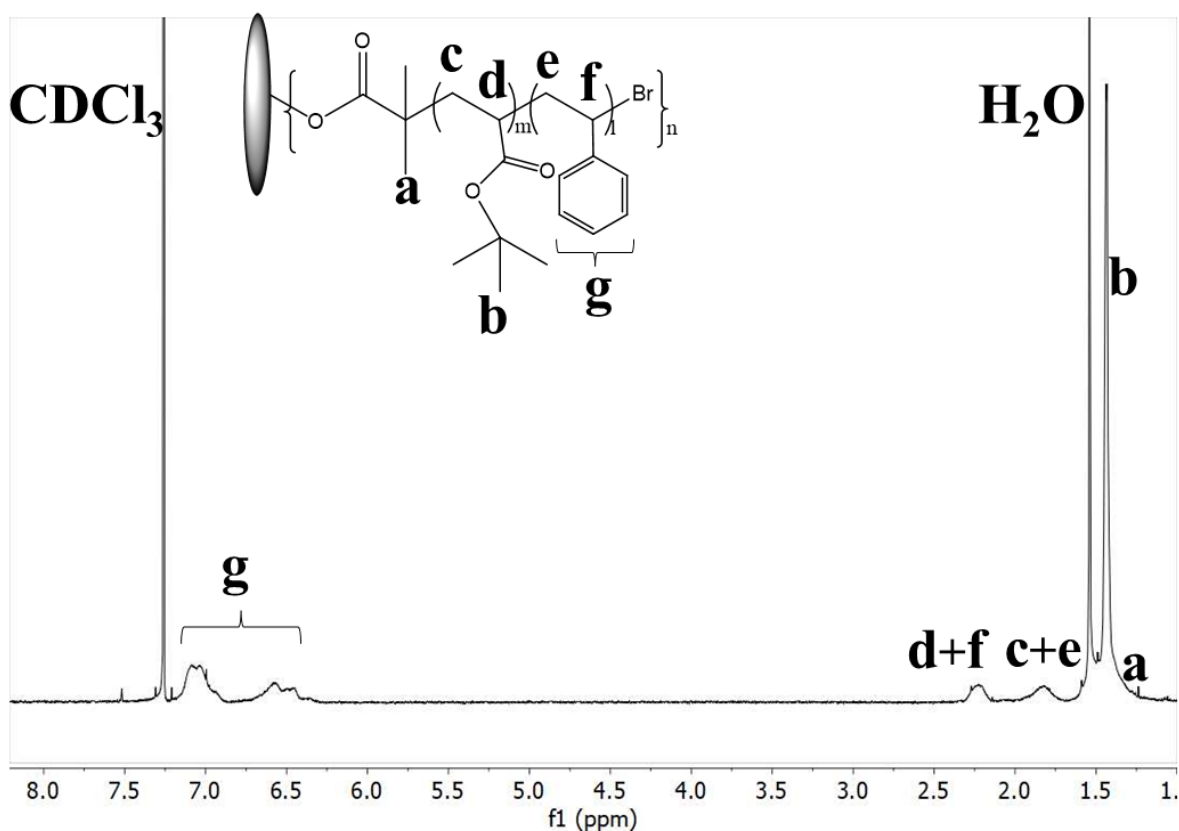


Figure 5.5. Typical ^1H NMR spectrum of the PtBA-*b*-PS bottlebrush-like block copolymer.

Table 5.1. Molecular Weight of PtBA-*b*-PS bottlebrush-like block copolymers

	$^a\text{M}_n, \text{PtBA}$	$^b\text{M}_n, \text{PtBA single chain}$	$^c\text{M}_n, \text{PtBA-PS}$	$^d\text{M}_n, \text{PS single chain}$	^ePDI
Cell6.5K-PtBA24K	24 kg/mol	1.6 kg/mol	-	-	1.08
Cell6.5K-PtBA48K	48 kg/mol	3.1 kg/mol	-	-	1.11
Cell6.5K-PtBA94K	94 kg/mol	5.8 kg/mol	-	-	1.15
Cell6.5K-PtBA94K-PS240K	94 kg/mol	5.8 kg/mol	272 kg/mol	11 kg/mol	1.21

$^a,^c$ Total number average molecular weights of PtBA and PtBA-*b*-PS star-like polymer were determined by GPC. $^b,^d$ Number average molecular weight of each PtBA and PS block were calculated from ^1H NMR. e Polydispersity index (PDI) were determined by GPC

The successful hydrolysis of *PtBA* block into PAA block was confirmed by comparing the FT-IR spectra of the polymer before and after the reaction. As shown in **Figure 5.6.**, the appearance of a broad absorption peak at 2500 to 3600 cm^{-1} indicates the formation of carboxylic acid group in the PAA blocks. In addition, the carbonyl stretching shifted from 1726 cm^{-1} in *PtBA* to 1700 cm^{-1} in PAA, further confirming the conversion of *PtBA* into PAA. The molecular weight of PAA blocks can be calculated from the difference in molecular weight of *tBA* group and acrylic acid group.

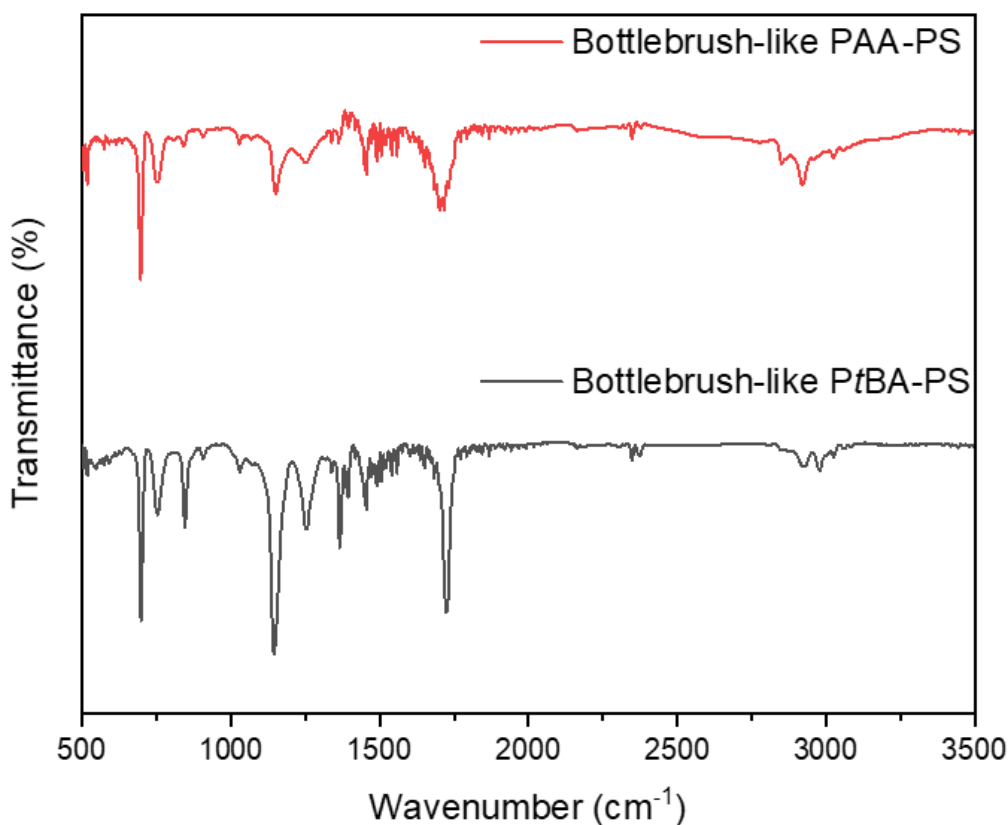


Figure 5.6. FT-IR spectra of *PtBA*-*b*-PS and PAA-*b*-PS bottlebrush-like polymers.

It is worth noting that it is more challenging to synthesize bottlebrush block polymers than star-like block copolymers due to the larger number of side chains on one Cell-Br macroinitiator (ranging from about 40 chains to more than 150 chains), high quality bottlebrush-like block copolymers are more challenging to synthesize than star-like block copolymers, which only have 21 arms. The ability to polymerize each chain in the bottlebrush polymer is a prerequisite to obtain high quality 1D nanoreactor and the 1D nanocrystals. Therefore, the main effort in this chapter is focused on the exploration of the appropriate polymerization conditions to achieve the ideal bottlebrush-like block copolymer nanoreactors.

As summarized in **Table 5.2.**, a common issue found in the synthesis of bottlebrush PtBA is the tailing in the low molecular weight in the GPC curve (**Figure 5.7**). This is usually caused by ununiform initiation of the side chain polymers and the appearance of dead chain ends during the reaction.¹⁷² Many parameters were tuned to prevent the appearance of the tail, including the ratio between -Br group and Cu(I)Br, ligand, monomer, and solvent, as well as adding Cu(II)Br₂ and Cu(I)Cl in the catalyst system. However, the improvement in the polymerization results is not consistent and the problems seemed to be hard to control.

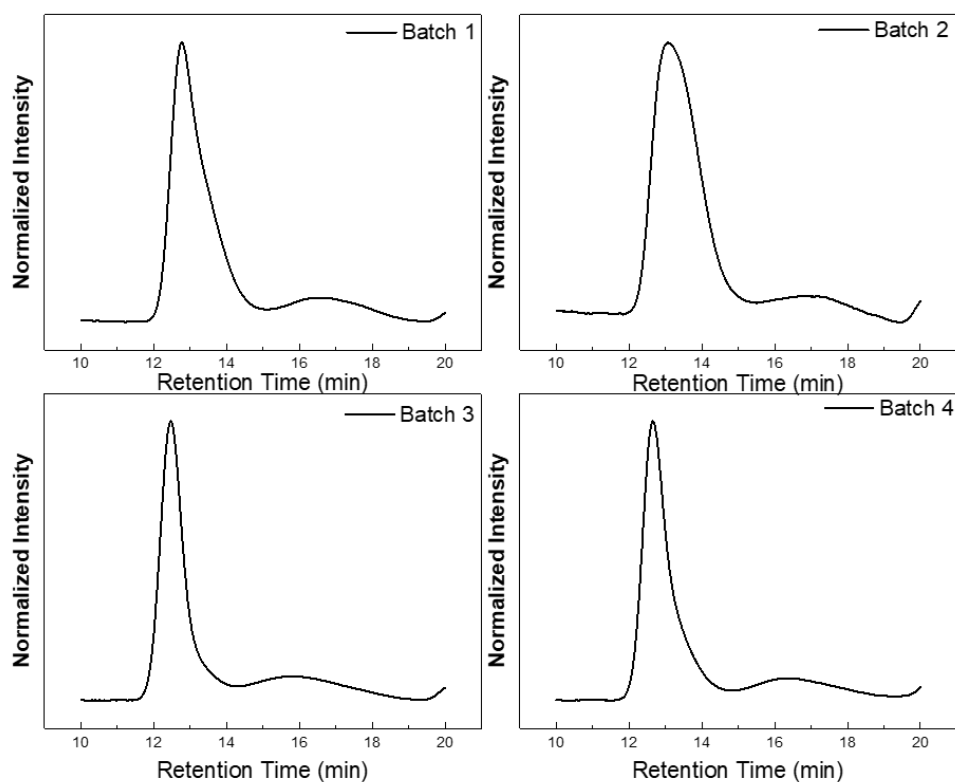


Figure 5.7. Examples of bottlebrush-like *PtBA* polymers with tailing in their GPC curves.

Although the tailing could be prevented in some trials list in Table 5.2., their reproducibility and kinetics between different batches using the same reaction condition are poor. Due to the inconsistency in the reaction kinetics and the uncontrollable tailing in the reaction, it is suspected that the bubbling method is not enough to remove oxygen thoroughly enough. Also, the freshness of CuBr catalyst was also found to be critical affecting the reaction. This is because Cu(I)Br, although stored in the fridge, still undergoes oxidization gradually, which could be evidenced by observing the color changing from white to green and then to blue. The partial oxidization of Cu(I)Br introduce uncertainty and inaccuracy in the polymerization. Therefore, freshly prepared Cu(I)Br was used for each polymerization. Yet, the polymerization kinetics kept changing from

batch to batch. Therefore, freeze-pump-thaw (FPT) method was employed to replace the more convenient inert gas bubbling method to completely and repeatably deoxygenize the system. In fact, FPT method led to the appearance of coupling peak in the high molecular weight region in GPC curves, likely due to the reaction kinetic became too fast because of more inert environment and fresh Cu(I)Br. This coupling could be easily prevented by diluting the reaction system.

Table 5.2. Reaction Parameter Tuning of ATRP of Bottlebrush P*t*BA

Cellulose-Br	Reaction Parameter (Br: CuBr: Ligand: monomer, solvent volume)	Result
15.9k	1:1:2:1000, 44mL	Small tail
15.9k	1:1:6:1000, 44mL	Small tail
15.9k	1:0.5:2:1000, 66mL	Small tail
15.9k	1:0.5:2:1300, 66mL	No tail
19k	1:1:2:1000, 44mL	Tail
19k	1:1:6:1000, 44mL	Small tail
19k	1:0.5:2:1000, 66mL	Small tail
19k	1:(0.25+0.25CuCl):2:1000, 44mL	Large tail

19k	1:0.5:4:1000, 44mL	Tail
19k	1:0.5:8:1300, 66mL	Small tail
19k	1:(0.45+0.05 CuBr ₂):4:1000, 66mL	No tail

With appropriate reaction condition and concentration, as well as higher deoxygenation efficiency, high-quality bottlebrush PtBA could be reproducibly synthesized when their molecular weight is not larger than 10 times of that of Cellulose-Br initiator. In order to be able to synthesize longer PtBA, more modifications are needed, such as higher bromination efficiency of the initiator and more purification of the initiator.

Owing to the relatively slow reaction kinetics, bottlebrush PS are easier to be achieved, if the first block is polymerized well. It is worth pointing out that the kinetic of PS polymerization varies largely based on the first block, probably due to different chain end fidelity achieved from the synthesis of the first block. Therefore, more experiment needs to be done to fully solve the tailing issue in the first block synthesis and be able to synthesize bottlebrush PtBA with larger molecular weight (i.e., larger than 10 times of the molecular weight of cellulose backbone).

After hydrolysis of PtBA into PAA block, bottlebrush like PAA-*b*-PS was fully dissolved in DMF and then spin-coated on silicon wafer to the visualization under AFM. As shown in **Figure 5.8**, wormlike 1D morphology was observed. The templates did not possess perfect 1D nanorod morphologies because of the extraordinarily long PS side chains and a partial coupling during the synthesis of PS block. Nevertheless, being able to observe 1D morphology is an important

milestone in this project, indicating that the quality of nanoreactor templates is close to the requirement for the craft of 1D inorganic nanorod. This work will also be continued by me as a postdoctoral fellow in Professor Lin's research group.

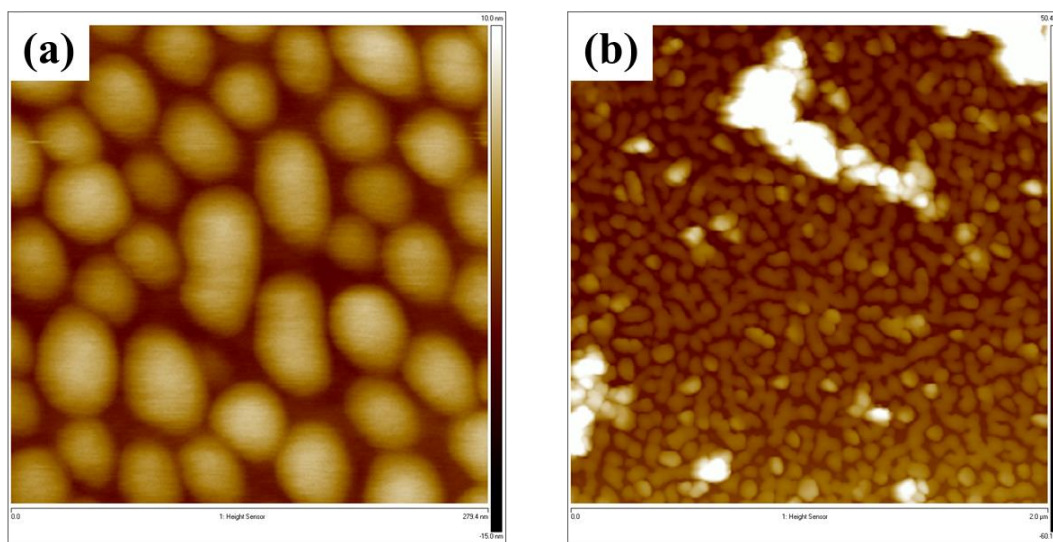


Figure 5.8. AFM images show the 1D worm-like morphology hydrolyzed Cell9K-PtBA113k-PS300k nanoreactor.

5.4. Conclusion

In summary, a comprehensive study was conducted to explore the synthesis of high-quality bottlebrush block polymers with uniform and densely grafted side chain block copolymers via sequential ATRP on a cellulose macroinitiator using the graft from strategy. Experiment conditions were examined individually and systematically to solve the tailing issue, which is commonly seen in bottlebrush polymer synthesis. 1D worm-like morphologies were successfully observed under atomic force microscopy, representing an important step towards to high quality rigid 1D nanoreactor, which could be applied in the inorganic nanorod synthesis.

Chapter 6. Reversible Photo Crosslinkable 2D Organic-Inorganic Metal Halide Perovskite Nanoplates for Advanced Optoelectronic Devices

6.1. Introduction

Halide perovskites, as an emerging class of semiconducting materials with outstanding optoelectronic properties, have a general chemical formula ABX_3 , where A^+ and B^{2+} are cations of different size and X^- are halide anions (Cl^- , Br^- , I^-) that coordinate with the B^{2+} cations and form corner sharing BX_6 octahedrons to construct the 3D structure.¹⁷³ 2D halide perovskites represent a subclass of halide perovskites. They are layered perovskite structures consisted of inorganic BX_6 octahedron slabs intercalated with organic cation spacers, which are normally large aliphatic or alkylammonium cations.^{174, 175} Currently, the most studied 2D perovskite is the so called Ruddlesden-Popper (RP) phase 2D perovskite where the perovskite layers are cut along the $\langle 100 \rangle$ crystallographic planes according to the 3D structure.^{176, 177} The RP compositions can be generally described as $L_2A_{n-1}B_nX_{3n-1}$, where L represents the large organic cation spacers and n indicates the number of BX_6 layers in the perovskite slab. The introduction of large organic cation spacers renders the RP 2D perovskites with superior stabilities compare to traditional 3D perovskite: First, 2D perovskites tend to have better humidity stability because the organic spacers are generally hydrophobic organic ammonium cations, which can prevent water molecules from contacting and penetrating into the 2D perovskite inorganic crystal lattice;¹⁷⁸ Second, 2D perovskite are more structurally stable because the strong van der Waals forces between the organic layers result in a higher formation energy to the RP perovskites.^{179, 180} An emerging research direction in the study of 2D perovskite is the investigation of the role of organic spacers in influencing the properties of the semiconductor. In this context, semiconducting organic cations are being heavily research recently.¹⁸¹⁻¹⁸³ Besides, it is also worth exploring the possibility of adding new functionality to the 2D perovskite such as responsibility towards stimuli by using responsible organic spacers.

Coumarin, a class of phenolic substances composed of fused benzene and α -pyrone rings, are naturally available in many plants and has been widely studied in biology, medicine and polymer science.¹⁸⁴ Coumarin undergo [2+2] photodimerization and photocleavage under irradiations with different wavelength. This unique reversible photo responsibility has attracted many research interests in liquid crystals,¹⁸⁵ photoactive surfaces,¹⁸⁶ light and energy harvesting,¹⁸⁷ etc. Recently, our group synthesis star-like PAA-b-PMAMC nanoreactor with coumarin in the repeating unit in the outer block polymers and successfully prepared Au NPs that undergo reversible photo induced self-assembly.⁴⁶ In this chapter, we plan to utilize the reversible photodimerization and photocleavage feature of coumarin molecules to craft coumarin containing 2D perovskites and investigate their photo-tunable properties.

6.2. Experimental Section

6.2.1. Materials

7-Hydroxy-4-methylcoumarin (**1**, 97%, Thermo Scientific), 7-amino-4-methylcoumarin (**2**, >98.0%, TCI), 2-(tert-butoxycarbonylamino)ethyl bromide (, 2-Boc ethyl bromide, >98%, TCI), 3-(tert-butoxycarbonylamino)propyl Bromide (3-Boc propyl bromide, >98%, TCI), 4-(tert-butoxycarbonylamino)butyl bromide (4-Boc butyl bromide, $\geq 90\%$, Sigma-Aldrich), toluene (ACS, VWR), dichloromethane (ACS, VWR), chlorobenzene (ACS, Beantown Chemical), anhydrous dimethylformamide (DMF, Millipore), lead bromide (99.99%, TCI), lead iodide (99.9985%, Alfa Aesar), butylamine (99%, Alfa Aesar), hydrobromic acid (48 wt%, Alfa Aesar), hydroiodic acid (57 wt%, Beantown Chemical), diethyl ether (ACS, Millipore Sigma), ethanol (200 proof, Koptec). All materials were used as received.

6.2.2. Methods

(a) Synthesis of 7-ammonium 4-methylcoumarin halide and butylammonium halide:

The preparations of 7-ammonium 4-methyl halide and butylammonium halide are modified according to literatures.^{188, 189} In short, excess amount of halide acids were dropped into an acetone/7-amino-4-methylcoumarin or a methanol/butylamine mixture at 0 °C. The reaction mixture was stirred for 2 hours and then washed with diethyl ether three times and dried in oven before use.

(b) Synthesis of 4-methylcoumarin-7-O-alkyl-Boc: In order to prepare 4-methylcoumarin-alkyl-ammonium bromide, a boc protecting strategy was applied based on literatures with modifications.¹⁹⁰ Typically, 1 g (5.68 mmol) 7-hydroxy-4-methylcoumarin is dissolved in 30 mL acetonitrile and 30mL acetone. After full dissolution, 3.91g (28.4 mmol) potassium carbonate is added to the solution and stirred for 1 hour. Then, 14.2 mmol Boc-alkyl bromide (i.e., 2-Boc ethyl bromide, 3-Boc propyl bromide, and 4-Boc butyl bromide) is added to the mixture and stirred under Ar or N₂ environment at 65 °C overnight. The reaction is then allowed to cool down to room temperature. Large amount of water is then added into the reaction flask and then acetonitrile and acetone are removed via rotary evaporation, resulting in white precipitates in water. The solid is separated by filtration, washed with copious amount of water and diethyl ether and dried in oven overnight.

(c) Synthesis of 4-methylcoumarin-7-O-alkyl-ammonium bromide: In a typical experiment, approximately 1 mmol dried products from step (b) is dissolved in 30 mL of acetone. 3 mmol of 48 wt% hydrobromic acid is then added to the solution and allowed to stir for 2 hours under Ar environment at 50 °C. After cooling down, the product was filtered and washed with copious amount of diethyl ether and dried in vacuum oven before use.

(d) Synthesis of $(R-NH_3)_2PbX_4$ nanoplatelets: Stock solutions were prepared by dissolving precursors (PbX_2 and LX) in DMF at concentration of 0.05 M for PbX_2 and 0.1 M for LX. 50 μ L of stock solution were then injected quickly into 10 mL of toluene under vigorous stirring at room temperature. For simplicity, 2D perovskite nanoplatelets synthesized from 7-ammonium-4-methylcoumarin halide are labeled as C_2PbX_4 , while nanoplatelets prepared using 4-methylcoumarin-7-O-alkyl- NH_3Br are labeled as CE_2PbBr_4 , CP_2PbBr_4 , and CB_2PbBr_4 , when an ethyl, propyl, and butyl group was between the coumarin group and ammonium end, respectively.

6.2.3. Characterization

The morphologies of as synthesized perovskite nanoplatelets were obtained using Hitachi HT7700 transmission electron microscopy (TEM) operating at 60 kV. X-ray diffraction (XRD) data were recorded by a Panalytical XPert PRO Alpha-1 diffractometer using $Cu-K\alpha$ radiation (1.54 \AA , at 45 kV and 40mA) with a step of 0.08° per 16 s. The UV-vis spectra were obtained with a Shimadzu UV-2600 spectrometer. The photoluminescence spectra were obtained by a PerkinElmer LS 55 fluorescence spectrometer. The molecular structure of coumarin containing A cations and intermediate products were analyzed by 1H NMR using Bruker Avance III 400 nuclear magnetic resonance spectroscopy using $DMSO-d_6$, $Acetone-d_6$, and $CDCl_3$ as solvents.

6.3. Results and Discussion

The successful conversion of **1** into 7-ammonium 4-methylcoumarin halide was confirmed by the 1H NMR spectrum using $DMSO-D_6$ as solvent, as shown in Figure 6.1.

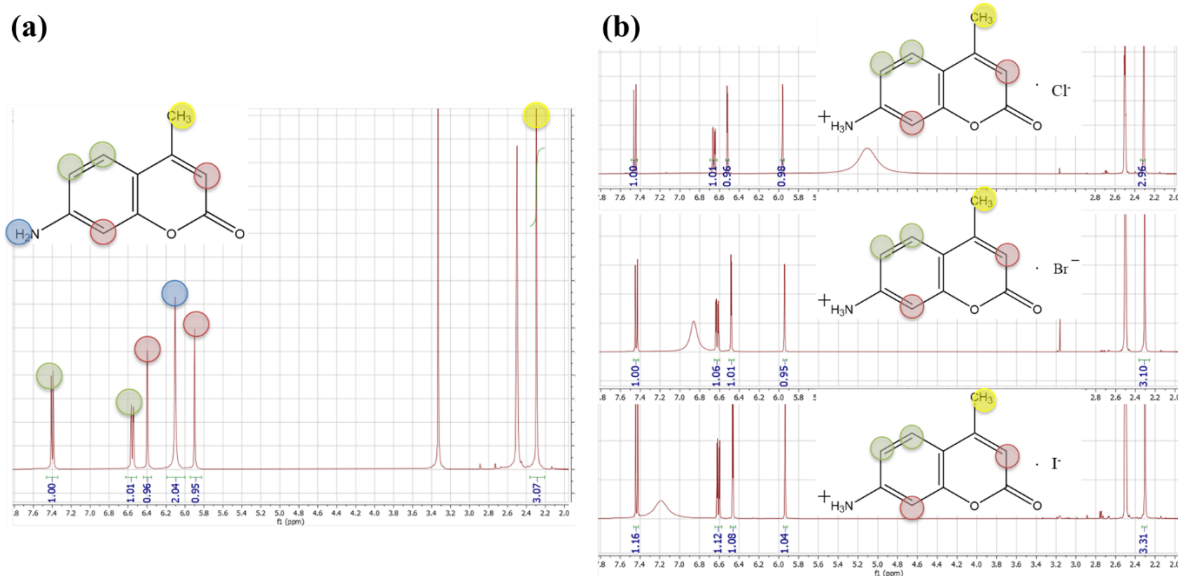


Figure 6.1. ^1H NMR spectra of (a) 7-amino-4-methylcoumarin and (b) 7-ammonium-4-methylcoumarin halides (chloride in the upper panel, bromide in the center panel, and iodide in the lower panel).

UV-vis absorption and PL spectra were used to characterize the optical properties of the 2D perovskite nanoplatelet (**Figure 6.2 (a)**). However, the poor solubility of coumarin group in non-polar solvents significantly limit the reproducibility of the experiment. As can be seen in **Figure 6.2 (b)** synthesis of C2PbBr_4 was repeated for three times under the exact same conditions but resulted in a drastic difference in the UV-vis absorption and PL results. Therefore, it is not practical to produce photo crosslinkable coumarin containing 2D perovskite nanoplatelets by directly and barely using 7-ammonium-4-methylcoumarin halide as A cation.

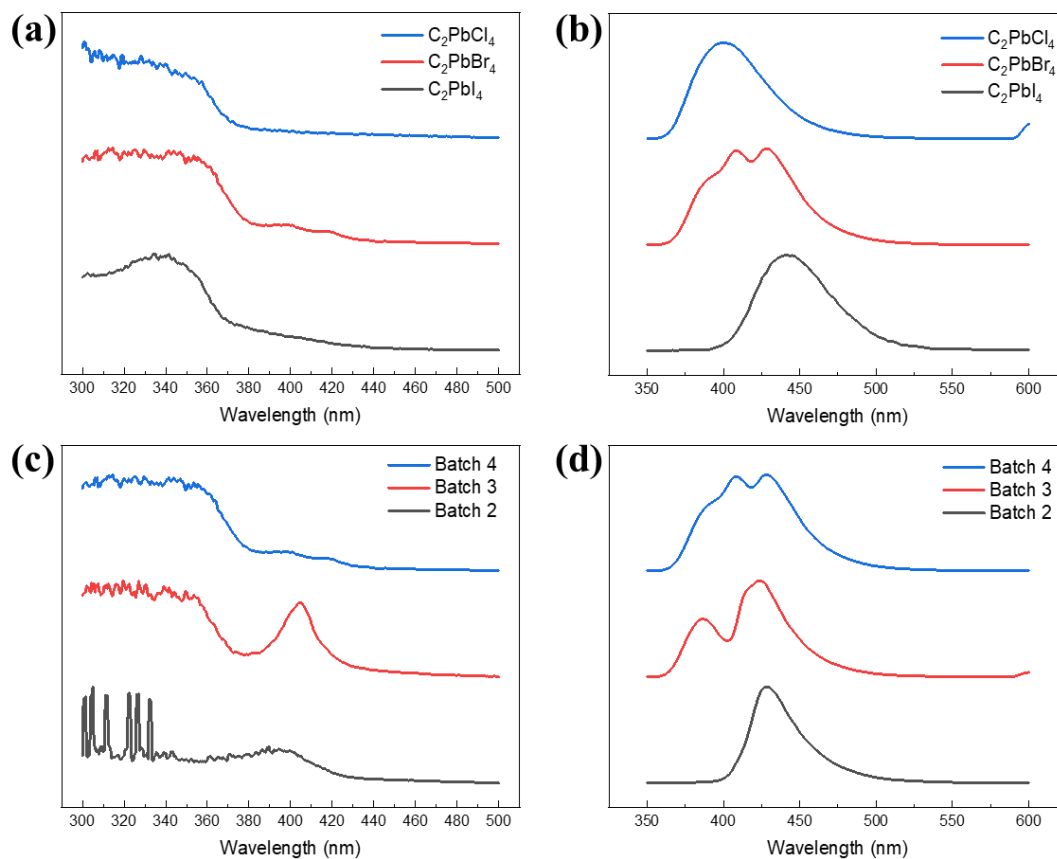


Figure 6.2. (a) UV-vis absorption and (b) PL spectra of as synthesized C_2PbX_4 nanoplatelets. (c) UV-vis absorption and (b) PL spectra of three as synthesized C_2PbBr_4 nanoplatelets batches, showing poor reproducibility.

To solve the problem of poor reproducibility, two strategies were applied. First, mixed A cations (butylammonium bromide plus 7-ammonium-4-methylcoumarin brodie) were used instead of single component. Butylammonium bromide (BABr) has been widely studied as bulky A cations in 2D perovskite nanoplatelets.^{175, 191} It is hypothesized that the formation of coumarin containing 2D perovskite will be better controlled with the addition of BABr, either through a mixed A cation route or a template assisted growth route. From **Figure 6.3**, it could be observed

that a new group of periodic peaks appeared in addition to the pure BA_2PbBr_4 peaks with smaller periodicity, when different ratios of BABr and 7-amonium-4-methylcoumarin bromide were used as mixed A cations. These new peaks may be attributed to the formation of C_2PbBr_4 , rather than $\text{C}_x\text{BA}_y\text{PbBr}_4$, because their positions and periodicity remained unchanged when the A cation composition is varied. As such, it is more likely that the C_2PbBr_4 grow and stack under the guidance of BA_2PbBr_4

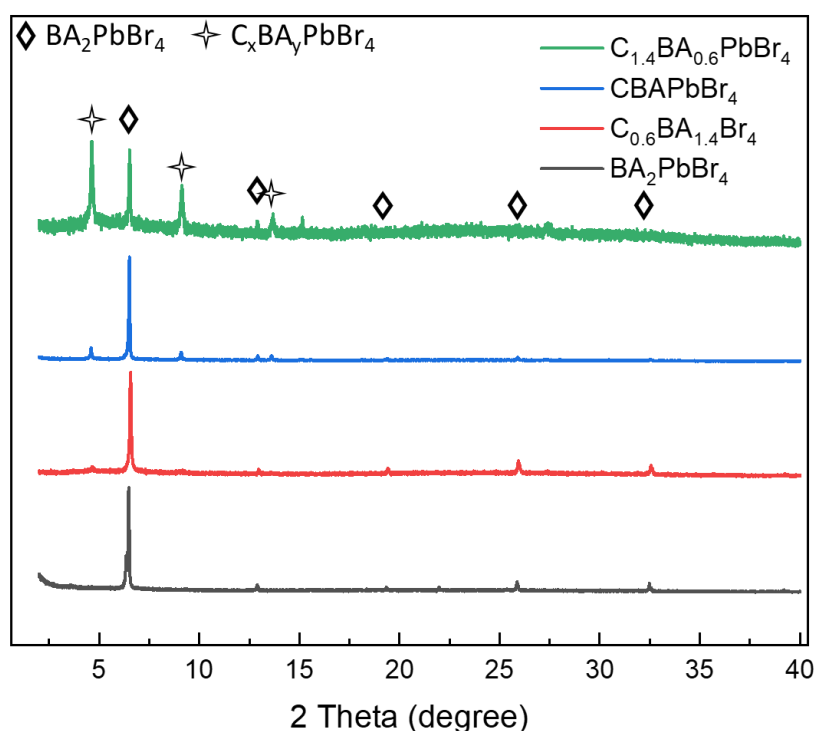


Figure 6.3. XRD patterns of pure BA_2PbBr_4 2D perovskite and 2D perovskite made from mixed A cations consisted of coumarin containing A cation and BABr at different ratios.

TEM images (Figure 6.4) also confirmed the formation of 2D nanoplatelet morphologies in the mixed A cation 2D perovskite samples. However, a big challenge remains is that the separation of C_2PbBr_4 from BA_2PbBr_4 . Therefore, despite of the potential to produce photo

crosslinkable coumarin containing 2D perovskite, the mixed A cation approach is not very suitable for device application.

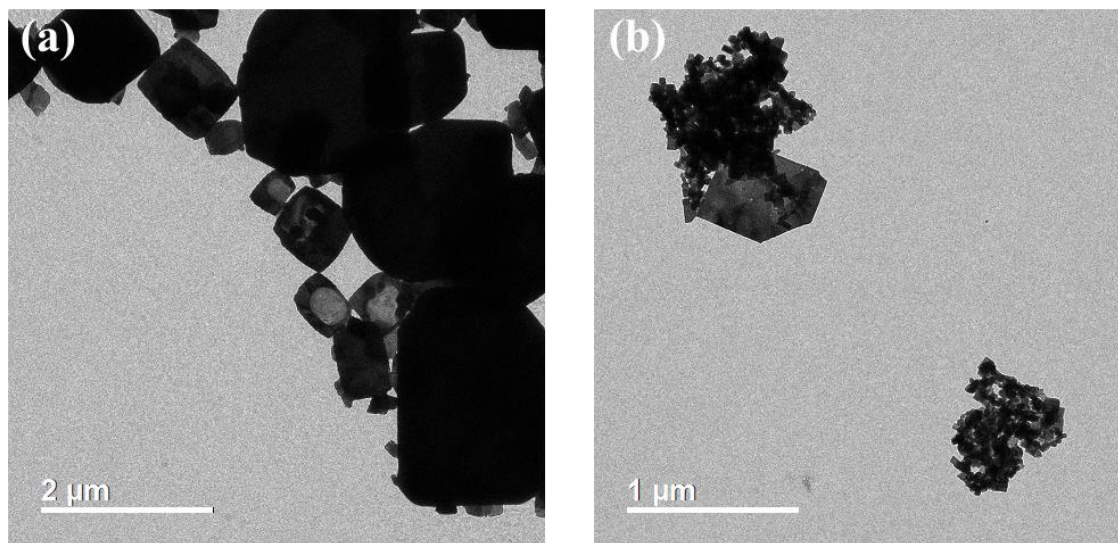


Figure 6.4. TEM images of (a) BA_2PbBr_4 nanoplatelets and (b) nanostructures resulted from synthesis using BA:coumarin 1:1 mixed A cations.

The second method could be used to solve the solubility issue is molecular modification of the coumarin containing A cations to enhance their solubility in non-polar solvent inherently. We attempted to attach alkyl chains of varied chain length as spacers between ammonium group and the coumarin groups and explore their influence on the synthesis of 2D perovskite. To synthesize coumarin containing A cations with spacers of distinct length, a two-step reaction was conducted, as detailed in the *Experimental Section*. ^1H NMR was used to confirm the successful preparation of the A cations (e.g., using propyl group as spacer, shown in **Figure 6.5**)

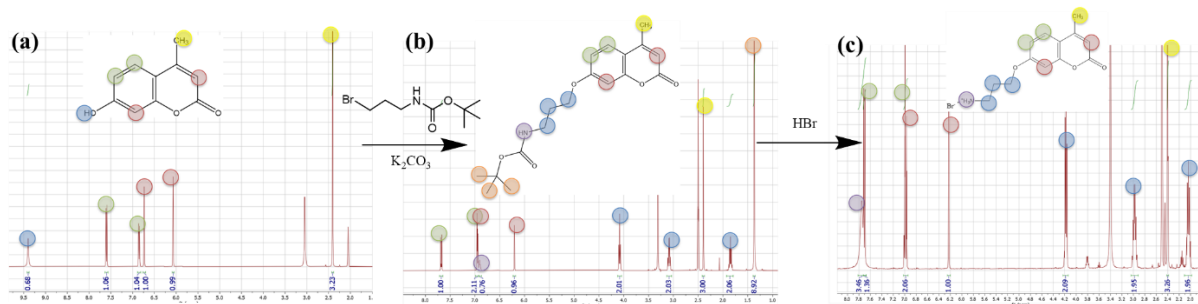


Figure 6.5. ^1H NMR spectrum of (a) 7-hydroxyl-4-methylcoumarin, (b) 4-methylcoumarin-7-O-propyl-Boc, and (c) 4-methylcoumarin-7-O-propyl-ammonium bromide.

Ethyl, propyl, and butyl groups have been used as spacers for the modification. Based on the observation, when butyl groups are anchored onto coumarin groups, the solubility of the produced 2D perovskite nanoplatelet was improved. Yet, the enhancement is not significant enough to be detected by eyes when ethyl and propyl groups were applied as spacers. Despite the poor solubility, UV-vis absorption and PL emission results still show characteristic features of 2D perovskite. (**Figure 6.6 (d-f)**) With the sharp contrast with the optical properties of coumarin containing ammonium bromides shown in **Figure 6.6 (a-c)**, it is convincing that 2D perovskite nanoplatelets have been formed.

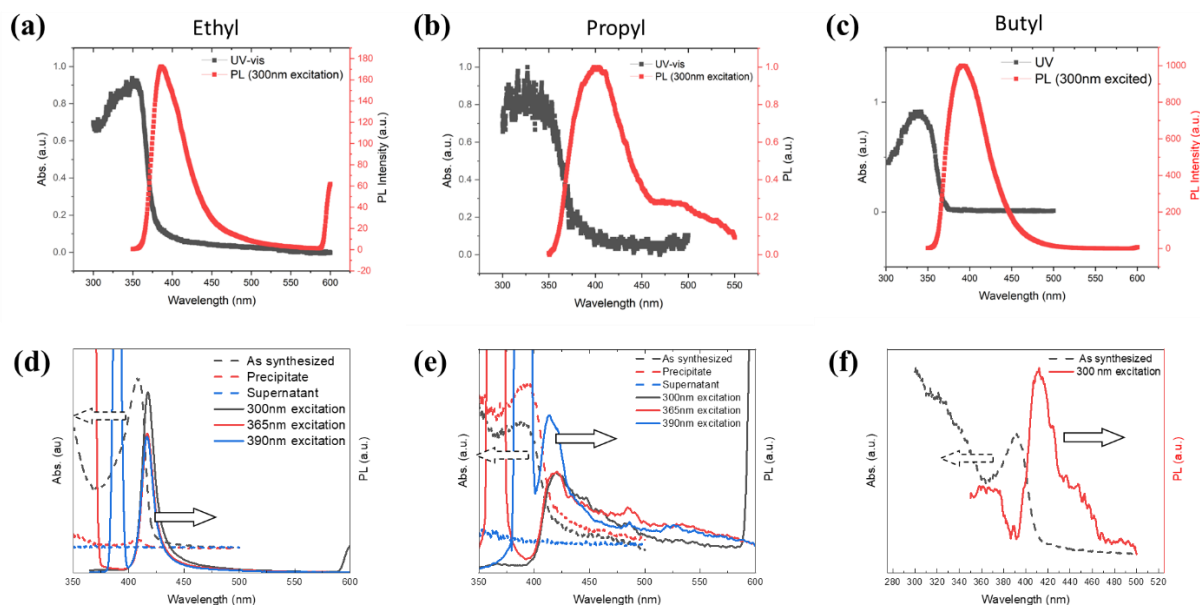


Figure 6.6. UV-vis absorption and PL emission spectra of coumarin containing A cations with (a) ethyl (b) propyl (c) butyl group as spacers and 2D perovskites synthesized from coumarin containing A cation with (d) ethyl (e) propyl (f) butyl group as spacers.

TEM was used to observe the morphologies of obtained nanocrystals. It can be seen that some 2D nanostructures were formed. However, they lack uniform morphology and have very different morphology when spacer species changed. Due to the limitation in solubility and the ease of degradation of perovskite nanocrystals against many solvents due to their ionic structure, purification becomes a big challenge. Fortunately, a trend in the increase in solubility has been noticed, indicating the possibility of completely solving the problem when alkyl spacers are even longer than butyl group.

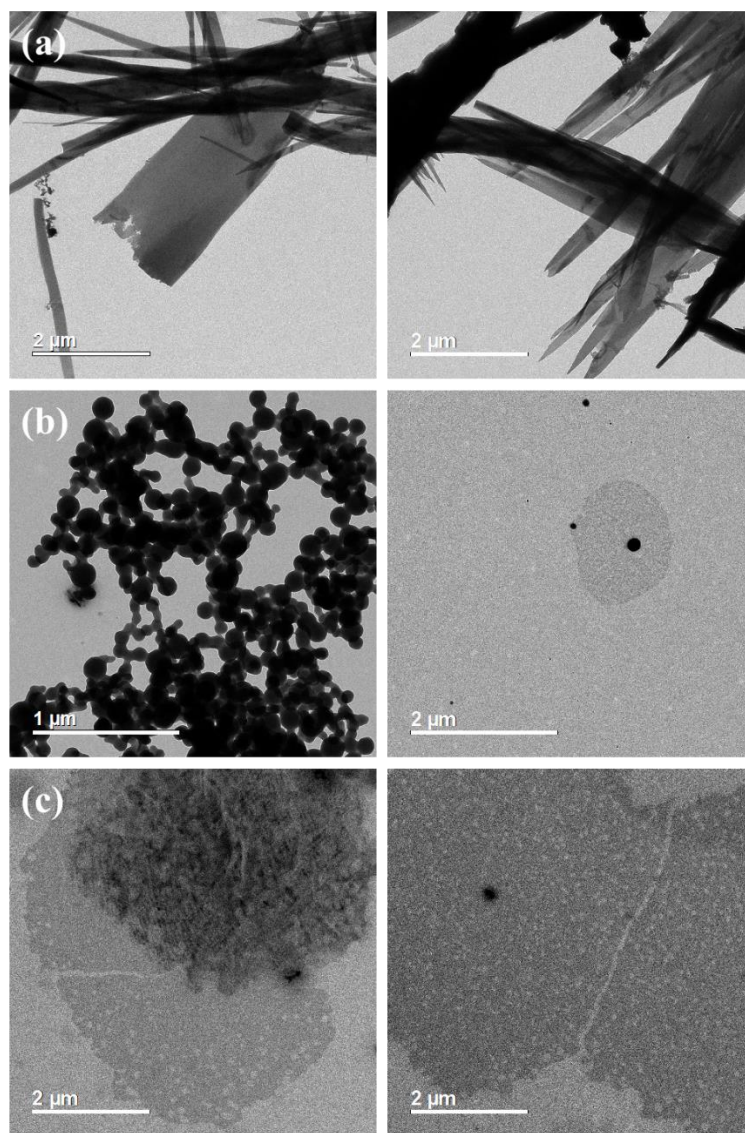


Figure 6.7. TEM images of coumarin containing 2D perovskite nanoplatelets using coumarin containing A cations with (a) ethyl (b) propyl and (c) butyl groups as spacers.

6.4. Conclusion

In this chapter, coumarin containing molecules were attempted, for the first time, as A cations for the synthesis of 2D perovskite nanoplatelets. Due to the limited solubility of coumarin groups in non-polar solvent, molecular modification was conducted to vary the length of spacers from 0 carbon, 2 carbons, 3 carbons, to 4 carbons. The synthesis became non-reproducible when

no spacer is present. A trend in the enhancement of solubility could be found when larger spacers are used. XRD confirmed the appearance of a group of periodic peaks, indicating the formation of 2D structures. TEM also reveals that 2D morphology are formed, despite the lack of uniformity, which is highly likely due to the solubility issue of the spacers. Overall, this project proves the potential in coumarin to be used as A cations to form functional and photo responsive 2D perovskite nanomaterials and will be continued in my post-doctoral study in Professor Lin's group.

Chapter 7. General Conclusions and Broader Impacts

7.1. General Conclusions

On the basis of the results and discussion in Chapter 3-6, we explored the synthesis of organic-inorganic hybrid nanocrystals in 0D, 1D, and 2D and studied practical applications of a unique ternary nanocomposite system. Nanoparticles were first synthesized via conventional colloidal method to form multi-functional nanocomposite with significantly improved antibacterial properties under ambient environment and showed great potential as antibacterial food packaging materials when mixed with cellulose nanofibrils. In addition, precise synthesis of 0D nanoparticles and 1D nanorods were enabled via a unique yet universal and robust nonlinear block copolymer nanoreactor strategy developed in our group. The dimensions of nanocrystals could be easily tuned via controlling the polymerization of block copolymers while the surface chemistry could be changed by growing outer block polymers with targeted functionality such as responsibility towards environment stimuli and semiconducting properties. Moreover, inspired by a previous work in the group where photo responsive polymer with coumarin group in the repeating units in the outer polymer block, we investigate the potential of using coumarin containing molecules as A cations to synthesize light responsive and reversible crosslinkable 2D perovskite nanoplatelets.

First of all, water dispersible antibacterial Ag NPs, semiconducting TiO₂ NPs, and upconverting NaYF₄@Yb:Tm NPs were synthesized via conventional colloidal synthetic methods. Ligand exchange treatment was applied when needed. It was found that the combination of Ag and TiO₂ NPs could remarkably improve their photocatalytic and antibacterial activity through a synergistic effect which reduce the bandgap of TiO₂ due to the electron transfer from Ag to TiO₂

under visible light and the higher ratio of Ti (III) oxide on the surface of TiO₂ due to its interaction with Ag. With the introduction of UCNPs, the NIR irradiation is be converted blue and UV lights which could be absorbed by Ag and TiO₂ NPs, respectively, and boost their activity. As a result, more ROS were generated (predominantly ·OH) even under ambient light environment. This ternary nanocomposite showed great potential to be used in food packaging industry as they can be easily mixed with cellulose and other hydrophilic polymers while still maintain the outstanding antibacterial performance.

Second, we utilized a set of star-like PAA-b-PS block copolymers as nanoreactors for the synthesis of a library of 0D plain nanoparticles. The size of the nanocrystals is controlled by the space taken by the inner PAA block, which can be precisely tuned the polymerization time due to the living characteristic of ATRP. The permanently and intimate tethering of the outer block PS overs supreme stability of the nanocrystals grown inside the nanoreactors. A series of nanoparticles were successfully prepared, including spinel metal oxide such as CoFe₂O₄, NiFe₂O₄, Fe₃O₄, perovskite oxide such as BaTiO₃, metal halide perovskite such as CsPbBr₃, and metallic nanoparticles such as Au. We then systematically studied the magnetic field enhancement of the OER activity in CFO NPs by crafting CFO/CoFe₂O_xH_y core/shell structure via surface reconstruction of PS ligated CFO NPs. Preliminary results confirmed the enhancement of OER activity in the nanoparticles after magnetization owing to the spin-pinning effect, which is the first time that spin-pinning effect is utilized to improve electrocatalytic activity at nanoscale.

Third, we investigate the synthesis of high-quality bottlebrush block copolymers via graft from method using brominated cellulose as backbone polymer. Multiple reaction parameters were systematically adjusted to unveil their effects on the polymerization of first block PtBA. It was found that freshness of Cu(I)Br catalyst and the degree of deoxygenation is of vital importance for

the synthesis of bottlebrush PtBA without tailing in GPC. So far, low and mediate length PtBA (<10 times of the molecular weight of Cellulose backbones) could be successfully produced. When uniform growth of side chain polymer could be realized, 1D morphology could be observed under AFM. As high grafting density and uniform polymerization of each block are prerequisites for the successful synthesis of 1D nanocrystals, it is necessary to continue fine tune reaction parameters and improve the quality of cellulose-Br initiators in the future.

Lastly, photo responsive reversible crosslinkable coumarin containing molecules were synthesized and used as A cations for the synthesis of 2D perovskite nanoplatelets. The reproducibility of 2D perovskite using coumarin ammonium halide without spacers is extremely low due to the poor solubility of coumarin in non-polar solvents such as toluene. When alkyl groups were anchored between coumarin group and ammonium ends, a gradual improvement in the solubility could be observed. TEM and XRD confirmed the formation of 2D structures. However, more systematic study is still in need to allow the control in morphology and in-depth understanding the growth mechanism of coumarin containing 2D perovskite nanoplates. Furthermore, exploration of their photo responsibility and resulted photo tunable properties will be conducted.

7.2. Broader Impacts

In this dissertation, we systematically explored the synthesis of nanocrystals with different morphologies ranging from 0D to 2D via different synthetic methods. 0D and 1D nanocrystals of different size and dimensions could be readily synthesized by capitalization on judiciously designed nonlinear block copolymers, i.e. nanoreactors. In addition, nanocrystals synthesized via nanoreactor strategy is advantageous over conventionally prepared nanocrystals in that nanoreactor strategy provides permanent capping of functional polymers which provide superior

colloidal stabilities, while conventionally synthesized nanocrystals are dynamically covered with small organic ligands which results in poor long-term stability. The highly stable nanocrystals and the tunable functionality determined by the properties of outer block polymers manifest their great potential in the energy related applications including light emitting diode, sensing, electrocatalysis, photocatalysis, etc. Moreover, we not only focused on nanoreactor strategy to craft high quality nanocrystal, but also research on exploring new materials for practical applications.

First, in Chapter 3, we developed an innovative ternary nanocomposite for enhanced antibacterial performance by capitalizing on the synergistic effect of Ag/TiO₂ NP mixture and the utilization of NIR irradiation by the UCNPs. The fast development in food industry needs highly efficient and safe material solutions to ensure the safety of food. Ag and TiO₂ have been studied as potential candidate as antibacterial active component in the food packaging. However, the concerns of toxicity of Ag and the requirement of UV by TiO₂ to kill bacteria greatly limited their usage. We creatively introduce a upconverting NPs which can convert NIR irradiation into blue and UV lights into the Ag/TiO₂ nanocomposite to reduce the usage of Ag and eliminate the need of UV simultaneously while keeping an outstanding antibacterial performance under ambient environment. Due to the water dispersibility of the nanocomposite, it can be easily mixed with many hydrophilic polymers including cellulose nanofibrils to form antibacterial films. This work provides a possible solution for food packaging industry to produce high efficiency and safe antibacterial packaging materials that work under ambient environment.

Moreover, in Chapter 4, we synthesized a set of monodispersed 0D nanoparticles by capitalizing on a unique, robust, and universal star-like nonlinear block copolymer nanoreactor strategy. The permanent and intimate attachment of outer block polymers protect the surface atoms from dissociation into environment or unwanted reactions under external stimuli such as heat,

moisture, O₂, etc. rendering outstanding colloidal stability and composition stability to the nanoparticles. Therefore, this strategy has great potential for preparing highly uniform 0D nanocrystals and is a perfect tool for the study of structure-property relationship in nanomaterials. In this work, we scrutinized the OER enhancement of CoFe₂O₄ nanoparticles synthesized via star-like PAA-*b*-PS nanoreactor. Owing to the stability and uniformity, we were able to adjust the degree of surface reconstruction on the CFO NPs to form CFO/CoFe₂O_xH_y core/shell nanostructures with varied core/shell ratio. We found out the spin pinning effect induced magnetic field enhancement in the OER activity of these ferromagnetic/paramagnetic core/shell nanoparticles, which has never been reported before. Therefore, this work has the potential to be extended to other electrocatalytic nanomaterials to further improve their activity.

Additionally, in Chapter 5, we systematically studied the reaction parameters for the synthesis of high-quality bottlebrush-like block copolymer via grafting from approach. Due to the nature of bottlebrush polymer and grafting from strategy, i.e., extremely high grafting density and large number of active sites during the polymerization, it has remained a big challenging to prepare bottlebrush polymers with uniformly grown side chains. In this work, we examined almost all the key parameters on their effect on the polymerization. We also utilized different dioxygen method and proved that freeze-pump-thaw method is more reliable to lead to repeatable reaction kinetics. The experience gained in this chapter will be helpful and useful for polymer chemists who need to synthesize high-quality bottlebrush polymers. Bottlebrush-like block copolymers, like star-like, can also be used for synthesis of 1D nanocrystals. The diameter and length of the nanocrystals could be precisely and easily controlled by the length of polymer backbone and the side chains. The ability to orthogonally tune dimensions of 1D nanocrystals could not be realized by other conventional methods, providing a great opportunity to investigate their structure-property

relationship in more depth and details that no other methods could afford. This strategy will also be important for the preparation of 1D nanocrystals that are not thermodynamically stable in anisotropic shape and hence impossible to be synthesized by conventional colloidal methods.

Finally, in Chapter 5, we attempted to broaden the current research in 2D perovskite nanocrystals by introducing controlled and reversible functionality to this intriguing class of materials. The solubility issue of photo responsive coumarin molecule is a barrier towards the realization of this exciting idea. Fortunately, molecular modification shows the potential to solve the solubility problem. This work may bring to the field of 2D perovskite more diversified research topics such as controlled assembly/disassembly and the resulting change in their physical properties. Inspired by using light to reversibly couple and decouple nanoplatelets, other dynamic interactions, such as hydrogen bonding, could also be inspected and utilized to achieve the similar controlled reversible assembly of nanoplatelets. This idea could also be useful for the assembly or hybridization of different nanocrystals to form heterojunctions.

In general, multiple strategies were employed in this work for the craft of functional nanomaterials. We provided new practical solutions to the industry, demonstrated unique synthetic approaches for prepared monodispersed nanomaterials and in depth and systematic research on their structure-property relationships and applications in energy applications, and explored the new research directions in controlled reversible assembly/disassembly of 2D perovskite nanomaterials.

Dissemination of Work

The work presented in this dissertation has been conveyed to the scientific community by the following publications and presentations.

Publications

1. **M. Zhang**, G. M. Biesold, W. Choi, J. Yu, M. Shofner, Y. Deng, C. Silvestre, Z. Lin, “Recent Advances in Polymers and Polymer Composites for Food Packaging”, *Materials Today*, **53**, 134 (2022).
2. **M. Zhang**, W. Chen, W. Choi, J. Yu, Y. Deng, X. Xie, Z. Lin, “Ternary Biocidal-Photocatalytic-Upconverting Nanocomposites for Enhanced Antibacterial Activity”, *ACS Sustainable Chemical and engineering*, **10**, 4741 (2022).
3. S. Liang*, **M. Zhang***, G. M. Biesold*, Y. He, Z. Li, D. Shen, Z. Lin, "Recent Advances in Synthesis, Properties, and Applications of Metal Halide Perovskite Nanocrystals/Polymer Nanocomposites", *Advanced Materials*, **33**, 2005888 (2021).
4. S. Liang, **M. Zhang**, S. He, M. Tian, W. Choi, T. Lian, Z. Lin, “A Library of Metal Halide Perovskite Nanorods with Designer Dimensions, Compositions, and Stabilities”, *Nature Synthesis*, (under review).
5. S. Liang, S. He, **M. Zhang**, Y. Yan, T. Jin, T. Lian, Z. Lin, “Tailoring Charge Separation at Meticulously Engineered Conjugated Polymer/Perovskite Quantum Dot Interface for Photocatalyzing Atom Transfer Radical Polymerization”, *Journal of the American Chemical Society*, **144**, 12901 (2022)
6. J. Wang, **M. Zhang**, Y. Liu, Y. Zhang, J. Jiang, H. Li, J. Chen, Z. Lin, “Ultrastable Highly-Emissive Amphiphilic Perovskite Nanocrystal Composites via the Synergy of Polymer-Grafted

Silica Nanoreactor and Surface Ligand Engineering for White Light-Emitting Diode” *Nano Energy*, **98**, 107321 (2022).

7. Y. Yan, S. Liang, X. Wang, **M. Zhang**, S. Hao, X. Cui, Z. Li, Z. Lin, "Robust wrinkled MoS₂/N-C bifunctional electrocatalysts interfaced with single Fe atoms for wearable zinc-air batteries”, *Proceedings of the National Academy of Sciences of the United State of America*, **118**, e2110036118 (2021).

8. L. Gao, X. Cui, Z. Wang, C. D. Sewell, Z. Li, S. Liang, **M. Zhang**, J. Li, Y. Hu, Z. Lin, "Operando Unraveling Photothermal-Promoted Dynamic Active Sites Generation in NiFe₂O₄ for Markedly Enhanced Oxygen Evolution”, *Proceedings of the National Academy of Sciences of the United State of America*, **118**, e2023421118 (2021).

9. J. Yu, A. C. Wang, **M. Zhang**, Z. Lin, "Water Treatment via Non-membrane Inorganic Nanoparticles/Cellulose Composites”, *Materials Today*, **50**, 329 (2021).

10. Z. Li, M. Tang, S. Liang, **M. Zhang**, G. Biesold-McGee, Y. He, S. Hao, W. Choi, Y. Liu, J. Peng, Z. Lin, "Bottlebrush polymers: From controlled synthesis, self-assembly, properties to applications”, *Progress in Polymer Science*, **116**, 101387 (2021).

11. Y. He, Y. Liang, S. Liang, Y.-W. Harn, **M. Zhang**, D. Shen, Z. Li, Y. Yan, X. Pang, Z. Lin, "Dual-Protected Metal Halide Perovskite Nanosheets with an Enhanced Set of Stabilities”, *Angewandte Chemie International Edition*, **60**, 7259 (2021).

12. S. Liang, **M. Zhang**, Y. He, Z. Kang, M. Tian, M. Zhang, H. Miao, Z. Lin "Polymer-ligated uniform lead chalcogenide nanoparticles with tunable size and robust stability enabled by judiciously designed surface chemistry”, *Chemistry of Materials*, **33**, 6701 (2021).

13. Y. Liu, J. Wang, **M. Zhang**, H. Li, and Z. Lin, "Polymer-Ligated Nanocrystals Enabled by Non-Linear Block Copolymer Nanoreactors: Synthesis, Properties and Applications", *ACS Nano*. **14**, 12491 (2020).
14. Y. Liu, Z. Wang, S. Liang, Z. Li, **M. Zhang**, H. Li, and Z. Lin, "Stable Perovskite Nanocrystals Permanently Ligated with Polymer Hairs via Star-like Molecular Bottlebrush Trilobe Nanoreactors", *Nano Letters* **19**, 9019 (2019).

Presentation

1. **M. Zhang**, Z. Lin, "Synthesis of Amphiphilic Bottlebrush-Like Block Copolymers and Their Utility as Nanoreactors for Metal Oxide Nanorods with Tunable Dimensions", American Chemical Society Spring National Meeting, San Diego, March 2022.

References

1. Baig, N.; Kammakakam, I.; Falath, W., Nanomaterials: a review of synthesis methods, properties, recent progress, and challenges. *Materials Advances* **2021**, 2 (6), 1821-1871.
2. Walter, P.; Welcomme, E.; Hallégot, P.; Zaluzec, N. J.; Deeb, C.; Castaing, J.; Veyssi re, P.; Br niaux, R.; L v  que, J.-L.; Tsoucaris, G., Early Use of PbS Nanotechnology for an Ancient Hair Dyeing Formula. *Nano Letters* **2006**, 6 (10), 2215-2219.
3. Freestone, I.; Meeks, N.; Sax, M.; Higgitt, C., The Lycurgus Cup — A Roman nanotechnology. *Gold Bulletin* **2007**, 40 (4), 270-277.
4. 'Plenty of room' revisited. *Nature Nanotechnology* **2009**, 4 (12), 781-781.
5. Kagan, C. R., Flexible colloidal nanocrystal electronics. *Chemical Society Reviews* **2019**, 48 (6), 1626-1641.
6. Yin, Y.; Alivisatos, A. P., Colloidal nanocrystal synthesis and the organic–inorganic interface. *Nature* **2005**, 437 (7059), 664-670.
7. Talapin, D. V.; Lee, J.-S.; Kovalenko, M. V.; Shevchenko, E. V., Prospects of Colloidal Nanocrystals for Electronic and Optoelectronic Applications. *Chemical Reviews* **2010**, 110 (1), 389-458.
8. Kovalenko, M. V.; Manna, L.; Cabot, A.; Hens, Z.; Talapin, D. V.; Kagan, C. R.; Klimov, V. I.; Rogach, A. L.; Reiss, P.; Milliron, D. J.; Guyot-Sionnest, P.; Konstantatos, G.; Parak, W. J.; Hyeon, T.; Korgel, B. A.; Murray, C. B.; Heiss, W., Prospects of Nanoscience with Nanocrystals. *ACS Nano* **2015**, 9 (2), 1012-1057.
9. Link, S.; El-Sayed, M. A., Spectral properties and relaxation dynamics of surface plasmon electronic oscillations in gold and silver nanodots and nanorods. *The Journal of Physical Chemistry B* **1999**, 103 (40), 8410-8426.

10. Bawendi, M. G.; Steigerwald, M. L.; Brus, L. E., The Quantum Mechanics of Larger Semiconductor Clusters ("Quantum Dots"). *Annual Review of Physical Chemistry* **1990**, *41* (1), 477-496.
11. El-Sayed, M. A., Small Is Different: Shape-, Size-, and Composition-Dependent Properties of Some Colloidal Semiconductor Nanocrystals. *Accounts of Chemical Research* **2004**, *37* (5), 326-333.
12. Algar, W. R.; Susumu, K.; Delehanty, J. B.; Medintz, I. L., Semiconductor Quantum Dots in Bioanalysis: Crossing the Valley of Death. *Analytical Chemistry* **2011**, *83* (23), 8826-8837.
13. Zhang, S.-Y.; Regulacio, M. D.; Han, M.-Y., Self-assembly of colloidal one-dimensional nanocrystals. *Chemical Society Reviews* **2014**, *43* (7), 2301-2323.
14. Fafarman, A. T.; Koh, W.-k.; Diroll, B. T.; Kim, D. K.; Ko, D.-K.; Oh, S. J.; Ye, X.; Doan-Nguyen, V.; Crump, M. R.; Reifsnnyder, D. C.; Murray, C. B.; Kagan, C. R., Thiocyanate-Capped Nanocrystal Colloids: Vibrational Reporter of Surface Chemistry and Solution-Based Route to Enhanced Coupling in Nanocrystal Solids. *Journal of the American Chemical Society* **2011**, *133* (39), 15753-15761.
15. Murray, C. B.; Kagan, C. R.; Bawendi, M. G., Self-Organization of CdSe Nanocrystallites into Three-Dimensional Quantum Dot Superlattices. *Science* **1995**, *270* (5240), 1335-1338.
16. Yang, J.; Choi, M. K.; Kim, D.-H.; Hyeon, T., Designed Assembly and Integration of Colloidal Nanocrystals for Device Applications. *Advanced Materials* **2016**, *28* (6), 1176-1207.
17. Gao, J.; Bender, C. M.; Murphy, C. J., Dependence of the Gold Nanorod Aspect Ratio on the Nature of the Directing Surfactant in Aqueous Solution. *Langmuir* **2003**, *19* (21), 9065-9070.

18. Liu, Y.; Gibbs, M.; Puthussery, J.; Gaik, S.; Ihly, R.; Hillhouse, H. W.; Law, M., Dependence of Carrier Mobility on Nanocrystal Size and Ligand Length in PbSe Nanocrystal Solids. *Nano Letters* **2010**, *10* (5), 1960-1969.
19. Elbert Katherine, C.; Zygmunt, W.; Vo, T.; Vara Corbin, M.; Rosen Daniel, J.; Krook Nadia, M.; Glotzer Sharon, C.; Murray Christopher, B., Anisotropic nanocrystal shape and ligand design for co-assembly. *Science Advances* *7* (23), eabf9402.
20. Elbert, K. C.; Vo, T.; Krook, N. M.; Zygmunt, W.; Park, J.; Yager, K. G.; Composto, R. J.; Glotzer, S. C.; Murray, C. B., Dendrimer Ligand Directed Nanoplate Assembly. *ACS Nano* **2019**, *13* (12), 14241-14251.
21. Zito, J.; Infante, I., The Future of Ligand Engineering in Colloidal Semiconductor Nanocrystals. *Accounts of Chemical Research* **2021**, *54* (7), 1555-1564.
22. De Roo, J.; Ibáñez, M.; Geiregat, P.; Nedelcu, G.; Walravens, W.; Maes, J.; Martins, J. C.; Van Driessche, I.; Kovalenko, M. V.; Hens, Z., Highly Dynamic Ligand Binding and Light Absorption Coefficient of Cesium Lead Bromide Perovskite Nanocrystals. *ACS Nano* **2016**, *10* (2), 2071-2081.
23. Fetters, L. J.; Kiss, A. D.; Pearson, D. S.; Quack, G. F.; Vitus, F. J., Rheological behavior of star-shaped polymers. *Macromolecules* **1993**, *26* (4), 647-654.
24. Li, X.; Iocozzia, J.; Chen, Y.; Zhao, S.; Cui, X.; Wang, W.; Yu, H.; Lin, S.; Lin, Z., From Precision Synthesis of Block Copolymers to Properties and Applications of Nanoparticles. *Angewandte Chemie International Edition* **2018**, *57* (8), 2046-2070.
25. Liu, Y.; Wang, J.; Zhang, M.; Li, H.; Lin, Z., Polymer-Ligated Nanocrystals Enabled by Nonlinear Block Copolymer Nanoreactors: Synthesis, Properties, and Applications. *ACS Nano* **2020**, *14* (10), 12491-12521.

26. Wang, J.-S.; Matyjaszewski, K., Controlled/"living" radical polymerization. atom transfer radical polymerization in the presence of transition-metal complexes. *Journal of the American Chemical Society* **1995**, *117* (20), 5614-5615.
27. Pyun, J.; Kowalewski, T.; Matyjaszewski, K., Synthesis of Polymer Brushes Using Atom Transfer Radical Polymerization. *Macromolecular Rapid Communications* **2003**, *24* (18), 1043-1059.
28. Chiefari, J.; Chong, Y.; Ercole, F.; Krstina, J.; Jeffery, J.; Le, T. P.; Mayadunne, R. T.; Meijs, G. F.; Moad, C. L.; Moad, G., Living free-radical polymerization by reversible addition–fragmentation chain transfer: the RAFT process. *Macromolecules* **1998**, *31* (16), 5559-5562.
29. Perrier, S., 50th Anniversary Perspective: RAFT Polymerization—A User Guide. *Macromolecules* **2017**, *50* (19), 7433-7447.
30. Cheng, C.; Qi, K.; Khoshdel, E.; Wooley, K. L., Tandem Synthesis of Core–Shell Brush Copolymers and Their Transformation to Peripherally Cross-Linked and Hollowed Nanostructures. *Journal of the American Chemical Society* **2006**, *128* (21), 6808-6809.
31. Oliveira, A. S. R.; Mendonça, P. V.; Simões, S.; Serra, A. C.; Coelho, J. F. J., Amphiphilic well-defined degradable star block copolymers by combination of ring-opening polymerization and atom transfer radical polymerization: Synthesis and application as drug delivery carriers. *Journal of Polymer Science* **2021**, *59* (3), 211-229.
32. Gao, H.; Matyjaszewski, K., Synthesis of functional polymers with controlled architecture by CRP of monomers in the presence of cross-linkers: From stars to gels. *Progress in Polymer Science* **2009**, *34* (4), 317-350.
33. Jin, X.; Sun, P.; Tong, G.; Zhu, X., Star polymer-based unimolecular micelles and their application in bio-imaging and diagnosis. *Biomaterials* **2018**, *178*, 738-750.

34. Seidi, F.; Shamsabadi, A. A.; Amini, M.; Shabanian, M.; Crespy, D., Functional materials generated by allying cyclodextrin-based supramolecular chemistry with living polymerization. *Polymer Chemistry* **2019**, *10* (27), 3674-3711.
35. Yao, X.; Huang, P.; Nie, Z., Cyclodextrin-based polymer materials: From controlled synthesis to applications. *Progress in Polymer Science* **2019**, *93*, 1-35.
36. Przybyla, M. A.; Yilmaz, G.; Becer, C. R., Natural cyclodextrins and their derivatives for polymer synthesis. *Polymer Chemistry* **2020**, *11* (48), 7582-7602.
37. Wang, F.; Lu, X.; He, C., Some recent developments of polyhedral oligomeric silsesquioxane (POSS)-based polymeric materials. *Journal of Materials Chemistry* **2011**, *21* (9), 2775-2782.
38. Zou, H.; Li, Q.-W.; Wu, Q.-L.; Liang, W.-Q.; Hou, X.-H.; Zhou, L.; Liu, N.; Wu, Z.-Q., POSS-based starlike hybrid helical poly(phenyl isocyanide)s: their synthesis, self-assembly, and enantioselective crystallization ability. *Polymer Chemistry* **2021**, *12* (27), 3917-3924.
39. Zadmard, R.; Hokmabadi, F.; Jalali, M. R.; Akbarzadeh, A., Recent progress to construct calixarene-based polymers using covalent bonds: synthesis and applications. *RSC Advances* **2020**, *10* (54), 32690-32722.
40. Simonova, M. A.; Tarasova, E. V.; Dudkina, M. M.; Tenkovtsev, A. V.; Filippov, A. P., Synthesis and hydrodynamic and conformation properties of star-shaped polystyrene with calix[8]arene core. *International Journal of Polymer Analysis and Characterization* **2019**, *24* (1), 87-95.
41. Iocozzia, J.; Lin, Z., A clean and simple route to soft, biocompatible nanocapsules via UV-cross-linkable azido-hyperbranched polyglycerol. *Macromolecules* **2017**, *50* (13), 4906-4912.

42. Totani, M.; Liu, L.; Matsuno, H.; Tanaka, K., Design of a star-like hyperbranched polymer having hydrophilic arms for anti-biofouling coating. *Journal of Materials Chemistry B* **2019**, 7 (7), 1045-1049.
43. Heise, A.; Diamanti, S.; Hedrick, J. L.; Frank, C. W.; Miller, R. D., Investigation of the Initiation Behavior of a Dendritic 12-Arm Initiator in Atom Transfer Radical Polymerization. *Macromolecules* **2001**, 34 (11), 3798-3801.
44. Pang, X.; Zhao, L.; Akinc, M.; Kim, J. K.; Lin, Z., Novel Amphiphilic Multi-Arm, Star-Like Block Copolymers as Unimolecular Micelles. *Macromolecules* **2011**, 44 (10), 3746-3752.
45. Chen, Y.; Wang, Z.; Harn, Y. W.; Pan, S.; Li, Z.; Lin, S.; Peng, J.; Zhang, G.; Lin, Z., Resolving optical and catalytic activities in thermoresponsive nanoparticles by permanent ligation with temperature-sensitive polymers. *Angewandte Chemie International Edition* **2019**, 58 (34), 11910-11917.
46. Chen, Y.; Wang, Z.; He, Y.; Yoon, Y. J.; Jung, J.; Zhang, G.; Lin, Z., Light-enabled reversible self-assembly and tunable optical properties of stable hairy nanoparticles. *Proceedings of the National Academy of Sciences* **2018**, 115 (7), E1391-E1400.
47. Chen, Y.; Yang, D.; Yoon, Y. J.; Pang, X.; Wang, Z.; Jung, J.; He, Y.; Harn, Y. W.; He, M.; Zhang, S.; Zhang, G.; Lin, Z., Hairy Uniform Permanently Ligated Hollow Nanoparticles with Precise Dimension Control and Tunable Optical Properties. *Journal of the American Chemical Society* **2017**, 139 (37), 12956-12967.
48. Zheng, D.; Pang, X.; Wang, M.; He, Y.; Lin, C.; Lin, Z., Unconventional Route to Hairy Plasmonic/Semiconductor Core/Shell Nanoparticles with Precisely Controlled Dimensions and Their Use in Solar Energy Conversion. *Chemistry of Materials* **2015**, 27 (15), 5271-5278.

49. He, M.; Pang, X.; Liu, X.; Jiang, B.; He, Y.; Snaith, H.; Lin, Z., Inside Back Cover: Monodisperse Dual-Functional Upconversion Nanoparticles Enabled Near-Infrared Organolead Halide Perovskite Solar Cells (Angew. Chem. Int. Ed. 13/2016). *Angewandte Chemie International Edition* **2016**, 55 (13), 4367-4367.
50. Pang, X.; Zhao, L.; Feng, C.; Lin, Z., Novel amphiphilic multiarm, starlike coil-Rod diblock copolymers via a combination of click chemistry with living polymerization. *Macromolecules* **2011**, 44 (18), 7176-7183.
51. Jiang, B.; Pang, X.; Li, B.; Lin, Z., Organic-Inorganic Nanocomposites via Placing Monodisperse Ferroelectric Nanocrystals in Direct and Permanent Contact with Ferroelectric Polymers. *Journal of the American Chemical Society* **2015**, 137 (36), 11760-11767.
52. Xu, H.; Pang, X.; He, Y.; He, M.; Jung, J.; Xia, H.; Lin, Z., Inside Back Cover: An Unconventional Route to Monodisperse and Intimately Contacted Semiconducting Organic-Inorganic Nanocomposites (Angew. Chem. Int. Ed. 15/2015). *Angewandte Chemie International Edition* **2015**, 54 (15), 4679-4679.
53. Li, Z.; Tang, M.; Liang, S.; Zhang, M.; Biesold, G. M.; He, Y.; Hao, S.-M.; Choi, W.; Liu, Y.; Peng, J.; Lin, Z., Bottlebrush polymers: From controlled synthesis, self-assembly, properties to applications. *Progress in Polymer Science* **2021**, 116, 101387.
54. Liang, H.; Cao, Z.; Wang, Z.; Sheiko, S. S.; Dobrynin, A. V., Combs and Bottlebrushes in a Melt. *Macromolecules* **2017**, 50 (8), 3430-3437 % @ 0024-9297.
55. Matyjaszewski, K.; Xia, J., Atom transfer radical polymerization. *Chemical reviews* **2001**, 101 (9), 2921-2990.
56. Yagci, Y.; Tasdelen, M. A., Mechanistic transformations involving living and controlled/living polymerization methods. *Progress in Polymer Science* **2006**, 31 (12), 1133-1170.

57. Verduzco, R.; Li, X.; Pesek, S. L.; Stein, G. E., Structure, function, self-assembly, and applications of bottlebrush copolymers. *Chemical Society Reviews* **2015**, *44* (8), 2405-2420.
58. Chen, K.; Hu, X.; Zhu, N.; Guo, K., Design, Synthesis, and Self-Assembly of Janus Bottlebrush Polymers. *Macromolecular Rapid Communications* **2020**, *41* (20), 2000357.
59. Sheiko, S. S.; Sumerlin, B. S.; Matyjaszewski, K., Cylindrical molecular brushes: Synthesis, characterization, and properties. *Progress in Polymer Science* **2008**, *33* (7), 759-785.
60. Matyjaszewski, K., Advanced materials by atom transfer radical polymerization. *Advanced Materials* **2018**, *30* (23), 1706441.
61. Pang, X.; He, Y.; Jung, J.; Lin, Z., 1D nanocrystals with precisely controlled dimensions, compositions, and architectures. *Science* **2016**, *353* (6305), 1268-1272.
62. Zhang, H.; Wu, J.; Zhang, J.; He, J., 1-Allyl-3-methylimidazolium chloride room temperature ionic liquid: a new and powerful nonderivatizing solvent for cellulose. *Macromolecules* **2005**, *38* (20), 8272-8277.
63. Zhang, J.; Wang, Z.; Wang, X.; Wang, Z., The synthesis of bottlebrush cellulose-graft-diblock copolymer elastomers via atom transfer radical polymerization utilizing a halide exchange technique. *Chemical Communications* **2019**, *55* (92), 13904-13907.
64. Choinopoulos, I., Grubbs' and Schrock's catalysts, ring opening metathesis polymerization and molecular brushes—synthesis, characterization, properties and applications. *Polymers* **2019**, *11* (2), 298.
65. Radzinski, S. C.; Foster, J. C.; Chapleski Jr, R. C.; Troya, D.; Matson, J. B., Bottlebrush polymer synthesis by ring-opening metathesis polymerization: the significance of the anchor group. *Journal of the American Chemical Society* **2016**, *138* (22), 6998-7004.

66. Yuan, J.; Müller, A.; Matyjaszewski, K.; Sheiko, S., Molecular brushes. In *Polymer Science: A Comprehensive Reference, 10 Volume Set*, 2012; pp 199-264.
67. Heo, K.; Kim, Y. Y.; Kitazawa, Y.; Kim, M.; Jin, K. S.; Yamamoto, T.; Ree, M., Structural Characteristics of Amphiphilic Cyclic and Linear Block Copolymer Micelles in Aqueous Solutions. *ACS Macro Letters* **2014**, *3* (3), 233-239.
68. Kästle, G.; Boyen, H. G.; Weigl, F.; Lengl, G.; Herzog, T.; Ziemann, P.; Riethmüller, S.; Mayer, O.; Hartmann, C.; Spatz, J. P., Micellar nanoreactors—Preparation and characterization of hexagonally ordered arrays of metallic nanodots. *Advanced Functional Materials* **2003**, *13* (11), 853-861.
69. Förster, S.; Antonietti, M., Amphiphilic block copolymers in structure - controlled nanomaterial hybrids. *Advanced Materials* **1998**, *10* (3), 195-217.
70. Antonietti, M.; Wenz, E.; Bronstein, L.; Seregina, M., Synthesis and characterization of noble metal colloids in block copolymer micelles. *Advanced Materials* **1995**, *7* (12), 1000-1005.
71. Liu, S.; Weaver, J. V.; Save, M.; Armes, S. P., Synthesis of pH-responsive shell cross-linked micelles and their use as nanoreactors for the preparation of gold nanoparticles. *Langmuir* **2002**, *18* (22), 8350-8357.
72. Bosman, A. W.; Janssen, H. M.; Meijer, E. W., About Dendrimers: Structure, Physical Properties, and Applications. *Chemical Reviews* **1999**, *99* (7), 1665-1688.
73. Bronstein, L. M.; Shifrina, Z. B., Dendrimers as encapsulating, stabilizing, or directing agents for inorganic nanoparticles. *Chemical reviews* **2011**, *111* (9), 5301-5344.
74. Higuchi, M.; Yamamoto, K., Novel π -conjugated nano-supramolecules having fine-controlled metal-assembling functions. *Bulletin of the Chemical Society of Japan* **2004**, *77* (5), 853-874.

75. Vögtle, F.; Gestermann, S.; Kauffmann, C.; Ceroni, P.; Vicinelli, V.; Balzani, V., Coordination of Co^{2+} ions in the interior of poly (propylene amine) dendrimers containing fluorescent dansyl units in the periphery. *Journal of the American Chemical Society* **2000**, *122* (42), 10398-10404.
76. Ottaviani, M. F.; Bossmann, S.; Turro, N. J.; Tomalia, D. A., Characterization of starburst dendrimers by the EPR technique. 1. Copper complexes in water solution. *Journal of the American Chemical Society* **1994**, *116* (2), 661-671.
77. Bakshi, M. S., Colloidal micelles of block copolymers as nanoreactors, templates for gold nanoparticles, and vehicles for biomedical applications. *Advances in colloid and interface science* **2014**, *213*, 1-20.
78. Hou, S.; Guo, Y.; Tang, Y.; Quan, Q., Synthesis and Stabilization of Colloidal Perovskite Nanocrystals by Multidentate Polymer Micelles. *ACS Applied Materials & Interfaces* **2017**, *9* (22), 18417-18422.
79. Tsukamoto, T.; Kuzume, A.; Nagasaka, M.; Kambe, T.; Yamamoto, K., Quantum Materials Exploration by Sequential Screening Technique of Heteroatomicity. *Journal of the American Chemical Society* **2020**, *142* (45), 19078-19084.
80. Pang, X.; Zhao, L.; Han, W.; Xin, X.; Lin, Z., A general and robust strategy for the synthesis of nearly monodisperse colloidal nanocrystals. *Nature Nanotechnology* **2013**, *8* (6), 426-431.
81. Awad, M. A.; Alkhulaifi, M. M.; Aldosari, N. S.; Alzahly, S.; Aldalbahi, A., Novel Eco-Synthesis of PD Silver Nanoparticles: Characterization, Assessment of Its Antimicrobial and Cytotoxicity Properties. *Materials* **2019**, *12* (23).

82. Rai, M.; Yadav, A.; Gade, A., Silver nanoparticles as a new generation of antimicrobials. *Biotechnology Advances* **2009**, *27* (1), 76-83.
83. Taglietti, A.; Arciola, C. R.; D'Agostino, A.; Dacarro, G.; Montanaro, L.; Campoccia, D.; Cucca, L.; Vercellino, M.; Poggi, A.; Pallavicini, P.; Visai, L., Antibiofilm activity of a monolayer of silver nanoparticles anchored to an amino-silanized glass surface. *Biomaterials* **2014**, *35* (6), 1779-1788.
84. Fahmy, H. M.; Salah Eldin, R. E.; Abu Serea, E. S.; Gomaa, N. M.; AboElmagd, G. M.; Salem, S. A.; Elsayed, Z. A.; Edrees, A.; Shams-Eldin, E.; Shalan, A. E., Advances in nanotechnology and antibacterial properties of biodegradable food packaging materials. *RSC Advances* **2020**, *10* (35), 20467-20484.
85. Morones, J. R.; Elechiguerra, J. L.; Camacho, A.; Holt, K.; Kouri, J. B.; Ramírez, J. T.; Yacaman, M. J., The bactericidal effect of silver nanoparticles. *Nanotechnology* **2005**, *16* (10), 2346.
86. Sondi, I.; Salopek-Sondi, B., Silver nanoparticles as antimicrobial agent: a case study on *E. coli* as a model for Gram-negative bacteria. *Journal of colloid and interface science* **2004**, *275* (1), 177-182.
87. Kim, J. S.; Kuk, E.; Yu, K. N.; Kim, J. H.; Park, S. J.; Lee, H. J.; Kim, S. H.; Park, Y. K.; Park, Y. H.; Hwang, C. Y.; Kim, Y. K.; Lee, Y. S.; Jeong, D. H.; Cho, M. H., Antimicrobial effects of silver nanoparticles. *Nanomedicine-Nanotechnology Biology and Medicine* **2007**, *3* (1), 95-101.
88. Danilczuk, M.; Lund, A.; Sadlo, J.; Yamada, H.; Michalik, J., Conduction electron spin resonance of small silver particles. *Spectrochimica Acta Part a-Molecular and Biomolecular Spectroscopy* **2006**, *63* (1), 189-191.

89. Gupta, A.; Maynes, M.; Silver, S., Effects of halides on plasmid-mediated silver resistance in *Escherichia coli*. *Applied and environmental microbiology* **1998**, *64* (12), 5042-5045.
90. Matsumura, Y.; Yoshikata, K.; Kunisaki, S.; Tsuchido, T., Mode of bactericidal action of silver zeolite and its comparison with that of silver nitrate. *Applied and Environmental Microbiology* **2003**, *69* (7), 4278-4281.
91. Morones, J. R.; Elechiguerra, J. L.; Camacho, A.; Holt, K.; Kouri, J. B.; Ramirez, J. T.; Yacaman, M. J., The bactericidal effect of silver nanoparticles. *Nanotechnology* **2005**, *16* (10), 2346-2353.
92. Hatchett, D. W.; White, H. S., Electrochemistry of sulfur adlayers on the low-index faces of silver. *Journal of Physical Chemistry* **1996**, *100* (23), 9854-9859.
93. Shrivastava, S.; Bera, T.; Roy, A.; Singh, G.; Ramachandrarao, P.; Dash, D., Characterization of enhanced antibacterial effects of novel silver nanoparticles. *Nanotechnology* **2007**, *18* (22).
94. Lee, S. Y.; Kim, H. J.; Patel, R.; Im, S. J.; Kim, J. H.; Min, B. R., Silver nanoparticles immobilized on thin film composite polyamide membrane: characterization, nanofiltration, antifouling properties. *Polymers for Advanced Technologies* **2007**, *18* (7), 562-568.
95. Eleftheriadou, M.; Pyrgiotakis, G.; Demokritou, P., Nanotechnology to the rescue: using nano-enabled approaches in microbiological food safety and quality. *Current Opinion in Biotechnology* **2017**, *44*, 87-93.
96. Echegoyen, Y.; Nerín, C., Nanoparticle release from nano-silver antimicrobial food containers. *Food and Chemical Toxicology* **2013**, *62*, 16-22.

97. Møller, J. K.; Bertelsen, G.; Skibsted, L. H., Photooxidation of nitrosylmyoglobin at low oxygen pressure. Quantum yields and reaction stoichiometries. *Meat science* **2002**, 60 (4), 421-425.
98. Minelli, G.; Lo Fiego, D. P.; Macchioni, P.; Fava, P., EFFECT OF DIFFERENT ILLUMINATION SOURCES ON COLOUR AND OXIDATIVE STABILITY OF SEASONED COPPA DI PARMA PGI. *Italian Journal of Food Science* **2020**, 32 (1), 181-194.
99. Liu, C.; Geng, L.; Yu, Y.; Zhang, Y.; Zhao, B.; Zhao, Q., Mechanisms of the enhanced antibacterial effect of Ag-TiO₂ coatings. *Biofouling* **2018**, 34 (2), 190-199.
100. Li, M.; Noriega-Trevino, M. E.; Nino-Martinez, N.; Marambio-Jones, C.; Wang, J.; Damoiseaux, R.; Ruiz, F.; Hoek, E. M. V., Synergistic Bactericidal Activity of Ag-TiO₂ Nanoparticles in Both Light and Dark Conditions. *Environmental Science & Technology* **2011**, 45 (20), 8989-8995.
101. Liang, L.; Meng, Y.; Shi, L.; Ma, J.; Sun, J., Enhanced photocatalytic performance of novel visible light-driven Ag-TiO₂/SBA-15 photocatalyst. *Superlattices and Microstructures* **2014**, 73, 60-70.
102. Mihaly Cozmuta, A.; Peter, A.; Mihaly Cozmuta, L.; Nicula, C.; Crisan, L.; Baia, L.; Turila, A., Active Packaging System Based on Ag/TiO₂ Nanocomposite Used for Extending the Shelf Life of Bread. Chemical and Microbiological Investigations. *Packaging Technology and Science* **2015**, 28 (4), 271-284.
103. Abutalib, M. M.; Rajeh, A., Enhanced structural, electrical, mechanical properties and antibacterial activity of Cs/PEO doped mixed nanoparticles (Ag/TiO₂) for food packaging applications. *Polymer Testing* **2021**, 93, 107013.

104. Prabhu, S.; Poullose, E. K., Silver nanoparticles: mechanism of antimicrobial action, synthesis, medical applications, and toxicity effects. *International Nano Letters* **2012**, 2 (1).
105. Zhou, Z.; Li, B.; Liu, X.; Li, Z.; Zhu, S.; Liang, Y.; Cui, Z.; Wu, S., Recent Progress in Photocatalytic Antibacterial. *ACS Applied Bio Materials* **2021**, 4 (5), 3909-3936.
106. Omerović, N.; Djislov, M.; Živojević, K.; Mladenović, M.; Vunduk, J.; Milenković, I.; Knežević, N. Ž.; Gadžanski, I.; Vidić, J., Antimicrobial nanoparticles and biodegradable polymer composites for active food packaging applications. *Comprehensive Reviews in Food Science and Food Safety* **2021**, 20 (3), 2428-2454.
107. Ebrahimi, Y.; Peighambaroust, S. J.; Peighambaroust, S. H.; Karkaj, S. Z., Development of Antibacterial Carboxymethyl Cellulose-Based Nanobiocomposite Films Containing Various Metallic Nanoparticles for Food Packaging Applications. *Journal of Food Science* **2019**, 84 (9), 2537-2548.
108. Sobhan, A.; Muthukumarappan, K.; Wei, L.; Van Den Top, T.; Zhou, R., Development of an activated carbon-based nanocomposite film with antibacterial property for smart food packaging. *Materials Today Communications* **2020**, 23, 101124.
109. Zhang, R.; Cheng, M.; Wang, X.; Wang, J., Bioactive mesoporous nano-silica/potato starch films against molds commonly found in post-harvest white mushrooms. *Food Hydrocolloids* **2019**, 95, 517-525.
110. Minelli, G.; Lo Fiego, D. P.; Macchioni, P.; Fava, P., Effect of Different Illumination Sources on Color and Oxidative Stability of Seasoned Coppa di Parma PGI. *Italian Journal of Food Science* **2020**, 32 (1), 181-194.
111. Kanmani, P.; Rhim, J.-W., Physicochemical properties of gelatin/silver nanoparticle antimicrobial composite films. *Food Chemistry* **2014**, 148, 162-169.

112. Ma, Y.; Li, J.; Si, Y.; Huang, K.; Nitin, N.; Sun, G., Rechargeable Antibacterial N-Halamine Films with Antifouling Function for Food Packaging Applications. *ACS Applied Materials & Interfaces* **2019**, *11* (19), 17814-17822.
113. Noimark, S.; Allan, E.; Parkin, I. P., Light-activated antimicrobial surfaces with enhanced efficacy induced by a dark-activated mechanism. *Chemical Science* **2014**, *5* (6), 2216-2223.
114. Otoni, C. G.; Moura, M. R. d.; Aouada, F. A.; Camilloto, G. P.; Cruz, R. S.; Lorevice, M. V.; Soares, N. d. F. F.; Mattoso, L. H. C., Antimicrobial and physical-mechanical properties of pectin/papaya puree/cinnamaldehyde nanoemulsion edible composite films. *Food Hydrocolloids* **2014**, *41*, 188-194.
115. Ye, X.; Collins, J. E.; Kang, Y.; Chen, J.; Chen, D. T. N.; Yodh, A. G.; Murray, C. B., Morphologically controlled synthesis of colloidal upconversion nanophosphors and their shape-directed self-assembly. *Proceedings of the National Academy of Sciences* **2010**, *107* (52), 22430.
116. Najmr, S.; Lu, T.; Keller, A. W.; Zhang, M.; Lee, J. D.; Makvandi, M.; Pryma, D. A.; Kagan, C. R.; Murray, C. B., Preparation of silica coated and ⁹⁰Y-radiolabeled β -NaYF₄ upconverting nanophosphors for multimodal tracing. *Nano Futures* **2018**, *2* (2), 025002.
117. Liu, J.; Bu, W.; Pan, L.; Shi, J., NIR-Triggered Anticancer Drug Delivery by Upconverting Nanoparticles with Integrated Azobenzene-Modified Mesoporous Silica. *Angewandte Chemie International Edition* **2013**, *52* (16), 4375-4379.
118. Park, Y. I.; Lee, K. T.; Suh, Y. D.; Hyeon, T., Upconverting nanoparticles: a versatile platform for wide-field two-photon microscopy and multi-modal in vivo imaging. *Chemical Society Reviews* **2015**, *44* (6), 1302-1317.
119. Liu, Y.; Teitelboim, A.; Fernandez-Bravo, A.; Yao, K.; Altoe, M. V. P.; Aloni, S.; Zhang, C.; Cohen, B. E.; Schuck, P. J.; Chan, E. M., Controlled Assembly of Upconverting

Nanoparticles for Low-Threshold Microlasers and Their Imaging in Scattering Media. *ACS Nano* **2020**, *14* (2), 1508-1519.

120. Fernandez-Bravo, A.; Wang, D.; Barnard, E. S.; Teitelboim, A.; Tajon, C.; Guan, J.; Schatz, G. C.; Cohen, B. E.; Chan, E. M.; Schuck, P. J.; Odom, T. W., Ultralow-threshold, continuous-wave upconverting lasing from subwavelength plasmons. *Nature Materials* **2019**, *18* (11), 1172-1176.

121. Kim, W. J.; Nyk, M.; Prasad, P. N., Color-coded multilayer photopatterned microstructures using lanthanide (III) ion co-doped NaYF₄ nanoparticles with upconversion luminescence for possible applications in security. *Nanotechnology* **2009**, *20* (18), 185301.

122. He, M.; Pang, X.; Liu, X.; Jiang, B.; He, Y.; Snaith, H.; Lin, Z., Monodisperse Dual-Functional Upconversion Nanoparticles Enabled Near-Infrared Organolead Halide Perovskite Solar Cells. *Angewandte Chemie International Edition* **2016**, *55* (13), 4280-4284.

123. Liao, W.; Zheng, D.; Tian, J.; Lin, Z., Dual-functional semiconductor-decorated upconversion hollow spheres for high efficiency dye-sensitized solar cells. *Journal of Materials Chemistry A* **2015**, *3* (46), 23360-23367.

124. Zhou, J.; Liu, Z.; Li, F., Upconversion nanophosphors for small-animal imaging. *Chemical Society Reviews* **2012**, *41* (3), 1323-1349.

125. Li, Z. Q.; Zhang, Y.; Jiang, S., Multicolor Core/Shell-Structured Upconversion Fluorescent Nanoparticles. *Advanced Materials* **2009**, *21* (47).

126. Tang, Y.; Di, W.; Zhai, X.; Yang, R.; Qin, W., NIR-Responsive Photocatalytic Activity and Mechanism of NaYF₄:Yb,Tm@TiO₂ Core-Shell Nanoparticles. *ACS Catalysis* **2013**, *3* (3), 405-412.

127. Qiu, Z.; Shu, J.; Tang, D., Near-Infrared-to-Ultraviolet Light-Mediated Photoelectrochemical Aptasensing Platform for Cancer Biomarker Based on Core–Shell NaYF₄:Yb,Tm@TiO₂ Upconversion Microrods. *Analytical Chemistry* **2018**, *90* (1), 1021-1028.
128. Lv, S.; Zhang, K.; Zhu, L.; Tang, D., ZIF-8-Assisted NaYF₄:Yb,Tm@ZnO Converter with Exonuclease III-Powered DNA Walker for Near-Infrared Light Responsive Biosensor. *Analytical Chemistry* **2020**, *92* (1), 1470-1476.
129. Tan, L.; Li, D.; Zhang, L.; Xu, L.; Zhao, Y.; Zhu, L.; Qiao, R., Preparation of Multishell-Structured NaYF₄:Yb,Tm,Nd@NaYF₄:Yb,Nd@SiO₂@ZnO Nanospheres with Effective NIR-Induced Photocatalytic Activity. *The Journal of Physical Chemistry C* **2020**, *124* (33), 18081-18090.
130. Tou, M.; Luo, Z.; Bai, S.; Liu, F.; Chai, Q.; Li, S.; Li, Z., Sequential coating upconversion NaYF₄:Yb,Tm nanocrystals with SiO₂ and ZnO layers for NIR-driven photocatalytic and antibacterial applications. *Materials Science and Engineering: C* **2017**, *70*, 1141-1148.
131. Li, H.; Xia, H.; Wang, D.; Tao, X., Simple synthesis of monodisperse, quasi-spherical, citrate-stabilized silver nanocrystals in water. *Langmuir* **2013**, *29* (16), 5074-5079.
132. Li, X.-L.; Peng, Q.; Yi, J.-X.; Wang, X.; Li, Y., Near Monodisperse TiO₂ Nanoparticles and Nanorods. *Chemistry – A European Journal* **2006**, *12* (8), 2383-2391.
133. Dong, A.; Ye, X.; Chen, J.; Kang, Y.; Gordon, T.; Kikkawa, J. M.; Murray, C. B., A Generalized Ligand-Exchange Strategy Enabling Sequential Surface Functionalization of Colloidal Nanocrystals. *Journal of the American Chemical Society* **2011**, *133* (4), 998-1006.
134. Haase, M.; Schäfer, H., Upconverting nanoparticles. *Angewandte Chemie International Edition* **2011**, *50* (26), 5808-5829.

135. Ye, X.; Collins, J. E.; Kang, Y.; Chen, J.; Chen, D. T.; Yodh, A. G.; Murray, C. B., Morphologically controlled synthesis of colloidal upconversion nanophosphors and their shape-directed self-assembly. *Proceedings of the National Academy of Sciences* **2010**, *107* (52), 22430-22435.
136. Jin, L. M.; Chen, X.; Siu, C. K.; Wang, F.; Yu, S. F., Enhancing Multiphoton Upconversion from NaYF₄:Yb/Tm@NaYF₄ Core–Shell Nanoparticles via the Use of Laser Cavity. *ACS Nano* **2017**, *11* (1), 843-849.
137. Li, C.; Quan, Z.; Yang, J.; Yang, P.; Lin, J., Highly Uniform and Monodisperse β -NaYF₄:Ln³⁺ (Ln = Eu, Tb, Yb/Er, and Yb/Tm) Hexagonal Microprism Crystals: Hydrothermal Synthesis and Luminescent Properties. *Inorganic Chemistry* **2007**, *46* (16), 6329-6337.
138. Tan, M. C.; Al-Baroudi, L.; Riman, R. E., Surfactant Effects on Efficiency Enhancement of Infrared-to-Visible Upconversion Emissions of NaYF₄:Yb-Er. *ACS Applied Materials & Interfaces* **2011**, *3* (10), 3910-3915.
139. Li, Z.; Zhang, Y., Monodisperse Silica-Coated Polyvinylpyrrolidone/NaYF₄ Nanocrystals with Multicolor Upconversion Fluorescence Emission. *Angewandte Chemie International Edition* **2006**, *45* (46), 7732-7735.
140. Hoffmann, M. R.; Martin, S. T.; Choi, W.; Bahnemann, D. W., Environmental Applications of Semiconductor Photocatalysis. *Chemical Reviews* **1995**, *95* (1), 69-96.
141. Wang, S.; Qian, H.; Hu, Y.; Dai, W.; Zhong, Y.; Chen, J.; Hu, X., Facile one-pot synthesis of uniform TiO₂–Ag hybrid hollow spheres with enhanced photocatalytic activity. *Dalton Transactions* **2013**, *42* (4), 1122-1128.

142. Li, X. Z.; Li, F. B., Study of Au/Au³⁺-TiO₂ Photocatalysts toward Visible Photooxidation for Water and Wastewater Treatment. *Environmental Science & Technology* **2001**, 35 (11), 2381-2387.
143. Wang, M.; Pang, X.; Zheng, D.; He, Y.; Sun, L.; Lin, C.; Lin, Z., Nonepitaxial growth of uniform and precisely size-tunable core/shell nanoparticles and their enhanced plasmon-driven photocatalysis. *Journal of Materials Chemistry A* **2016**, 4 (19), 7190-7199.
144. Hutchison, M. L.; Thomas, D. J. I.; Avery, S. M., Thermal death of Escherichia coli O157:H7 in cattle feeds. *Letters in Applied Microbiology* **2007**, 44 (4), 357-363.
145. Ali, T.; Ahmed, A.; Alam, U.; Uddin, I.; Tripathi, P.; Muneer, M., Enhanced photocatalytic and antibacterial activities of Ag-doped TiO₂ nanoparticles under visible light. *Materials Chemistry and Physics* **2018**, 212, 325-335.
146. Yu, Z.; Zhao, Y.; Gao, B.; Liu, X.; Jia, L.; Zhao, F.; Ma, J., Performance of novel a Ag-n-TiO₂/PVC reinforced hollow fiber membrane applied in water purification: in situ antibacterial properties and resistance to biofouling. *RSC Advances* **2015**, 5 (118), 97320-97329.
147. Xu, S.; Xu, W.; Wang, Y.; Zhang, S.; Zhu, Y.; Tao, L.; Xia, L.; Zhou, P.; Song, H., NaYF₄:Yb,Tm nanocrystals and TiO₂ inverse opal composite films: a novel device for upconversion enhancement and solid-based sensing of avidin. *Nanoscale* **2014**, 6 (11), 5859-5870.
148. Liao, J.; Yang, Z.; Wu, H.; Yan, D.; Qiu, J.; Song, Z.; Yang, Y.; Zhou, D.; Yin, Z., Enhancement of the up-conversion luminescence of Yb³⁺/Er³⁺ or Yb³⁺/Tm³⁺ co-doped NaYF₄ nanoparticles by photonic crystals. *Journal of Materials Chemistry C* **2013**, 1 (40), 6541-6546.
149. Alonso-Cristobal, P.; Oton-Fernandez, O.; Mendez-Gonzalez, D.; Díaz, J. F.; Lopez-Cabarcos, E.; Barasoain, I.; Rubio-Retama, J., Synthesis, Characterization, and Application in HeLa Cells of an NIR Light Responsive Doxorubicin Delivery System Based on

NaYF₄:Yb,Tm@SiO₂-PEG Nanoparticles. *ACS Applied Materials & Interfaces* **2015**, 7 (27), 14992-14999.

150. Mirmohseni, A.; Rastgar, M.; Olad, A., Preparation of PANI-CuZnO ternary nanocomposite and investigation of its effects on polyurethane coatings antibacterial, antistatic, and mechanical properties. *Journal of Nanostructure in Chemistry* **2018**, 8 (4), 473-481.

151. Lops, C.; Ancona, A.; Di Cesare, K.; Dumontel, B.; Garino, N.; Canavese, G.; Hernández, S.; Cauda, V., Sonophotocatalytic degradation mechanisms of Rhodamine B dye via radicals generation by micro- and nano-particles of ZnO. *Applied Catalysis B: Environmental* **2019**, 243, 629-640.

152. Park, C. B.; Lee, S. H.; Subramanian, E.; Kale, B. B.; Lee, S. M.; Baeg, J.-O., Solar energy in production of l-glutamate through visible light active photocatalyst—redox enzyme coupled bioreactor. *Chemical Communications* **2008**, (42), 5423-5425.

153. Zhou, X.; Lan, J.; Liu, G.; Deng, K.; Yang, Y.; Nie, G.; Yu, J.; Zhi, L., Facet-Mediated Photodegradation of Organic Dye over Hematite Architectures by Visible Light. *Angewandte Chemie International Edition* **2012**, 51 (1), 178-182.

154. Torun, E.; Fang, C. M.; de Wijs, G. A.; de Groot, R. A., Role of Magnetism in Catalysis: RuO₂ (110) Surface. *The Journal of Physical Chemistry C* **2013**, 117 (12), 6353-6357.

155. Garcés-Pineda, F. A.; Blasco-Ahicart, M.; Nieto-Castro, D.; López, N.; Galán-Mascarós, J. R., Direct magnetic enhancement of electrocatalytic water oxidation in alkaline media. *Nature Energy* **2019**, 4 (6), 519-525.

156. Ren, X.; Wu, T.; Sun, Y.; Li, Y.; Xian, G.; Liu, X.; Shen, C.; Gracia, J.; Gao, H.-J.; Yang, H.; Xu, Z. J., Spin-polarized oxygen evolution reaction under magnetic field. *Nature Communications* **2021**, 12 (1), 2608.

157. Khassin, A. A.; Anufrienko, V. F.; Ikorskii, V. N.; Plyasova, L. M.; Kustova, G. N.; Larina, T. V.; Molina, I. Y.; Parmon, V. N., Physico-chemical study on the state of cobalt in a precipitated cobalt-aluminum oxide system. *Physical Chemistry Chemical Physics* **2002**, *4* (17), 4236-4243.
158. Kudielka, A.; Bette, S.; Dinnebier, R.; Abeykoon, M.; Pietzonka, C.; Harbrecht, B., Variability of composition and structural disorder of nanocrystalline CoOOH materials. *Journal of Materials Chemistry C* **2017**, *5* (11), 2899-2909.
159. Wu, T.; Ren, X.; Sun, Y.; Sun, S.; Xian, G.; Scherer, G. G.; Fisher, A. C.; Mandler, D.; Ager, J. W.; Grimaud, A.; Wang, J.; Shen, C.; Yang, H.; Gracia, J.; Gao, H.-J.; Xu, Z. J., Spin pinning effect to reconstructed oxyhydroxide layer on ferromagnetic oxides for enhanced water oxidation. *Nature Communications* **2021**, *12* (1), 3634.
160. Gaborieau, M.; Castignolles, P., Size-exclusion chromatography (SEC) of branched polymers and polysaccharides. *Analytical and Bioanalytical Chemistry* **2011**, *399* (4), 1413-1423.
161. Grcev, S.; Schoenmakers, P.; Iedema, P., Determination of molecular weight and size distribution and branching characteristics of PVAc by means of size exclusion chromatography/multi-angle laser light scattering (SEC/MALLS). *Polymer* **2004**, *45* (1), 39-48.
162. Sun, G.; Cho, S.; Clark, C.; Verkhoturov, S. V.; Eller, M. J.; Li, A.; Pavía-Jiménez, A.; Schweikert, E. A.; Thackeray, J. W.; Trefonas, P.; Wooley, K. L., Nanoscopic Cylindrical Dual Concentric and Lengthwise Block Brush Terpolymers as Covalent Preassembled High-Resolution and High-Sensitivity Negative-Tone Photoresist Materials. *Journal of the American Chemical Society* **2013**, *135* (11), 4203-4206.

163. Miyake, G. M.; Piunova, V. A.; Weitekamp, R. A.; Grubbs, R. H., Precisely Tunable Photonic Crystals From Rapidly Self-Assembling Brush Block Copolymer Blends. *Angewandte Chemie International Edition* **2012**, *51* (45), 11246-11248.
164. Sowers, M. A.; McCombs, J. R.; Wang, Y.; Paletta, J. T.; Morton, S. W.; Dreaden, E. C.; Boska, M. D.; Ottaviani, M. F.; Hammond, P. T.; Rajca, A.; Johnson, J. A., Redox-responsive branched-bottlebrush polymers for in vivo MRI and fluorescence imaging. *Nature Communications* **2014**, *5* (1), 5460.
165. Zhang, T.; Wang, Y.; Ma, X.; Hou, C.; Lv, S.; Jia, D.; Lu, Y.; Xue, P.; Kang, Y.; Xu, Z., A bottlebrush-architected dextran polyprodrug as an acidity-responsive vector for enhanced chemotherapy efficiency. *Biomaterials Science* **2020**, *8* (1), 473-484.
166. Runge, M. B.; Bowden, N. B., Synthesis of High Molecular Weight Comb Block Copolymers and Their Assembly into Ordered Morphologies in the Solid State. *Journal of the American Chemical Society* **2007**, *129* (34), 10551-10560.
167. Qi, H.; Liu, X.; Henn, D. M.; Mei, S.; Staub, M. C.; Zhao, B.; Li, C. Y., Breaking translational symmetry via polymer chain overcrowding in molecular bottlebrush crystallization. *Nature Communications* **2020**, *11* (1), 2152.
168. Li, S.; Jiang, K.; Wang, J.; Zuo, C.; Jo, Y. H.; He, D.; Xie, X.; Xue, Z., Molecular Brush with Dense PEG Side Chains: Design of a Well-Defined Polymer Electrolyte for Lithium-Ion Batteries. *Macromolecules* **2019**, *52* (19), 7234-7243.
169. Ji, X.; Cao, M.; Fu, X.; Liang, R.; Le, A. N.; Zhang, Q.; Zhong, M., Efficient room-temperature solid-state lithium ion conductors enabled by mixed-graft block copolymer architectures. *Giant* **2020**, *3*, 100027.

170. Reynolds, V. G.; Mukherjee, S.; Xie, R.; Levi, A. E.; Atassi, A.; Uchiyama, T.; Wang, H.; Chabynyc, M. L.; Bates, C. M., Super-soft solvent-free bottlebrush elastomers for touch sensing. *Materials Horizons* **2020**, 7 (1), 181-187.
171. Xie, R.; Mukherjee, S.; Levi, A. E.; Reynolds, V. G.; Wang, H.; Chabynyc, M. L.; Bates, C. M., Room temperature 3D printing of super-soft and solvent-free elastomers. *Science Advances* **2020**, 6 (46), eabc6900.
172. Gregory, A.; Stenzel, M. H., Complex polymer architectures via RAFT polymerization: From fundamental process to extending the scope using click chemistry and nature's building blocks. *Progress in Polymer Science* **2012**, 37 (1), 38-105.
173. Liang, S.; Zhang, M.; Biesold, G. M.; Choi, W.; He, Y.; Li, Z.; Shen, D.; Lin, Z., Recent Advances in Synthesis, Properties, and Applications of Metal Halide Perovskite Nanocrystals/Polymer Nanocomposites. *Advanced Materials* **2021**, 33 (50), 2005888.
174. Gao, Y.; Wei, Z.; Hsu, S.-N.; Boudouris, B. W.; Dou, L., Two-dimensional halide perovskites featuring semiconducting organic building blocks. *Materials Chemistry Frontiers* **2020**, 4 (12), 3400-3418.
175. Shi, E.; Gao, Y.; Finkenauer, B. P.; Akriti; Coffey, A. H.; Dou, L., Two-dimensional halide perovskite nanomaterials and heterostructures. *Chemical Society Reviews* **2018**, 47 (16), 6046-6072.
176. Zhang, F.; Lu, H.; Tong, J.; Berry, J. J.; Beard, M. C.; Zhu, K., Advances in two-dimensional organic–inorganic hybrid perovskites. *Energy & Environmental Science* **2020**, 13 (4), 1154-1186.

177. Mao, L.; Stoumpos, C. C.; Kanatzidis, M. G., Two-Dimensional Hybrid Halide Perovskites: Principles and Promises. *Journal of the American Chemical Society* **2019**, *141* (3), 1171-1190.
178. Smith, I. C.; Hoke, E. T.; Solis-Ibarra, D.; McGehee, M. D.; Karunadasa, H. I., A Layered Hybrid Perovskite Solar-Cell Absorber with Enhanced Moisture Stability. *Angewandte Chemie International Edition* **2014**, *53* (42), 11232-11235.
179. Mitzi, D. B., Templating and structural engineering in organic–inorganic perovskites. *Journal of the Chemical Society, Dalton Transactions* **2001**, (1), 1-12.
180. Quan, L. N.; Yuan, M.; Comin, R.; Voznyy, O.; Beauregard, E. M.; Hoogland, S.; Buin, A.; Kirmani, A. R.; Zhao, K.; Amassian, A.; Kim, D. H.; Sargent, E. H., Ligand-Stabilized Reduced-Dimensionality Perovskites. *Journal of the American Chemical Society* **2016**, *138* (8), 2649-2655.
181. Park, I.-H.; Chu, L.; Leng, K.; Choy, Y. F.; Liu, W.; Abdelwahab, I.; Zhu, Z.; Ma, Z.; Chen, W.; Xu, Q.-H.; Eda, G.; Loh, K. P., Highly Stable Two-Dimensional Tin(II) Iodide Hybrid Organic–Inorganic Perovskite Based on Stilbene Derivative. *Advanced Functional Materials* **2019**, *29* (39), 1904810.
182. Gao, Y.; Shi, E.; Deng, S.; Shiring, S. B.; Snaider, J. M.; Liang, C.; Yuan, B.; Song, R.; Janke, S. M.; Liebman-Peláez, A.; Yoo, P.; Zeller, M.; Boudouris, B. W.; Liao, P.; Zhu, C.; Blum, V.; Yu, Y.; Savoie, B. M.; Huang, L.; Dou, L., Molecular engineering of organic–inorganic hybrid perovskites quantum wells. *Nature Chemistry* **2019**, *11* (12), 1151-1157.
183. Ortiz-Cervantes, C.; Román-Román, P. I.; Vazquez-Chavez, J.; Hernández-Rodríguez, M.; Solis-Ibarra, D., Thousand-fold Conductivity Increase in 2D Perovskites by Polydiacetylene Incorporation and Doping. *Angewandte Chemie International Edition* **2018**, *57* (42), 13882-13886.

184. Trenor, S. R.; Shultz, A. R.; Love, B. J.; Long, T. E., Coumarins in Polymers: From Light Harvesting to Photo-Cross-Linkable Tissue Scaffolds. *Chemical Reviews* **2004**, *104* (6), 3059-3078.
185. Schadt, M.; Schmitt, K.; Kozinkov, V.; Chigrinov, V., Surface-Induced Parallel Alignment of Liquid Crystals by Linearly Polymerized Photopolymers. *Japanese Journal of Applied Physics* **1992**, *31* (Part 1, No. 7), 2155-2164.
186. Tian, Y.; Akiyama, E.; Nagase, Y., Liquid crystalline cyclic tetramethyltetrasiloxanes containing coumarin moieties. *Journal of Materials Chemistry* **2003**, *13* (6), 1253-1258.
187. Serin, J.; Schultze, X.; Adronov, A.; Fréchet, J. M. J., Synthesis and Study of the Absorption and Luminescence Properties of Polymers Containing Ru(BpyMe₂)₃²⁺ Chromophores and Coumarin Laser Dyes. *Macromolecules* **2002**, *35* (14), 5396-5404.
188. Weidman, M. C.; Seitz, M.; Stranks, S. D.; Tisdale, W. A., Highly Tunable Colloidal Perovskite Nanoplatelets through Variable Cation, Metal, and Halide Composition. *ACS Nano* **2016**, *10* (8), 7830-7839.
189. Biesold, G. M.; Liang, S.; Wagner, B. K.; Kang, Z.; Lin, Z., Continuous production of ultrathin organic–inorganic Ruddlesden–Popper perovskite nanoplatelets via a flow reactor. *Nanoscale* **2021**, *13* (30), 13108-13115.
190. Passarelli, J. V.; Fairfield, D. J.; Sather, N. A.; Hendricks, M. P.; Sai, H.; Stern, C. L.; Stupp, S. I., Enhanced Out-of-Plane Conductivity and Photovoltaic Performance in n = 1 Layered Perovskites through Organic Cation Design. *Journal of the American Chemical Society* **2018**, *140* (23), 7313-7323.

191. Sheikh, T.; Nag, A., Mn Doping in Centimeter-Sized Layered 2D Butylammonium Lead Bromide (BA₂PbBr₄) Single Crystals and Their Optical Properties. *The Journal of Physical Chemistry C* **2019**, *123* (14), 9420-9427.